Waseda University Doctoral Dissertation

Research on Digital Control for DC/DC Switching Converters

Xutao LI

Graduate School of Information, Production and Systems

Waseda University

May 2016

Abstract

Nowadays, the switching mode power supplier (SMPS) is taking a higher and higher ratio of the power suppliers, because it has a well-known higher power conversion efficiency which is helpful for easing the energy crisis. The DC/DC switching converter is a very important kind of SMPS. A controller is always required for a converter, since it is nearly always desired to produce a well-regulated output voltage in the presence of variations in the input voltage and load current. The controller should first guarantee that the power conversion is stable under all operating conditions, and next, the desired dynamic performance is maintained when a disturbance occurs in the input voltage or the load. The dynamic performance of a switching converter, whether it has single- or multi-loop control, is determined by its closed-loop characteristics including the audio susceptibility and output impedance. For a boost, buck-boost and fly-back converter in continuous conduction mode (CCM), there is a right-half-plane-zero (RHPZ) in the transfer function from the duty ratio to the output voltage. This RHPZ severely restricts the crossover frequency of the open-loop gain, hence results in poor dynamic performance if single-loop voltage control is adopted. Multi-loop control is widely adopted to improve the dynamic performance. However, a current sampling circuit such as a shunt resistor with an amplifier, a transformer or an active filter, is required to detect the inductor or switch current, which causes an increase of the size, cost, and weight of the circuit. Sensorless multi-loop control solves this problem by an inductor current estimator instead of the inductor current sampling network.

In the past, the controller of a converter is always implemented by a circuit. In recent years, the digital control, which means the control part is implemented on a digital signal processor such as MCU, DSP and FPGA, begins to be adopted and attracts many researchers' interests, because the digital SMPS has many advantages. Firstly, it is easy to develop and modify the control part, which means the time-to-market can be shortened a lot. Secondly, it is very easy to implement a sophisticated algorithm to improve the dynamic performance. Thirdly, it is easy to add some functions such as communication to the system, while it is very difficult for the analog control. Fourthly, a digital controller will not vary along with the environment, so that high stability and noise immunity can be maintained. For these reasons, the digital switching converter will be more and more in future.

Therefore, this research focuses on the design of the sensorless control for DC/DC switching converters. Several design approaches to the sensorless control of boost converters are proposed. The deduced controllers are implemented on a digital signal processor NJU20010 produced by New Japan Radio Corporation.

Chapter 1 begins with the research background. A brief development history of DC/DC switching mode converters is firstly presented. After some research topics and technologies are introduced, this chapter ends with this research's purpose.

Chapter 2 is the preliminaries of the control of boost converters. After the principle of small signal average value model of SMPS is firstly introduced, the small signal average value model of a boost converter is deduced. Based on the small signal model, the closed-loop characteristics of single-loop and multi-loop control of boost converters are presented. Lastly, the principles of modern robust control including robust H∞ control and sliding mode control are introduced.

Chapter 3 is the proposed design method of the Luenberger observer (LO) based sensorless multi-loop control for boost converters. Current sensorless control of a switching converter contributes to reduce the size, weight, and cost of the converter. An LO is effective in estimating the inductor current for the current sensorless control. A closed-loop characteristics evaluation method is proposed to design an LO-based sensorless multi-loop control for boost converters. The closed-loop stability evaluation and the closed-loop characteristics evaluations of output voltage, inductor as well as the estimated inductor current are provided. Simulations show the design procedure of the controller and the observer. Practical experiments on a digital signal processor give the practical dynamic responses.

Chapter 4 is the proposal of robust H∞ synthesis approaches for the inductor current sensorless control of boost converters. The LO-based sensorless multi-loop control needs a trial-and-error design procedure, because there are too many parameters to be determined, and the closed-loop characteristics are not directly related with the loop gains for the multi-loop control. As a modern control, robust H∞ control adopts a compact sensorless controller and directly takes the disturbance attenuation as the target. In this chapter, a novel H∞ synthesis approach is firstly proposed to design a full-order sensorless controller for boost converters, which need not solve any algebraic Riccati equation (ARE) or linear matrix inequality (LMI), and most importantly, parameterizes the controller by an adjustable parameter behaving like a 'knob' on the dynamic performance. Simulations show the straightforward closed-loop characteristics evaluation and the closed-loop dynamic performance by the proposed H∞ approach. Practical experiments on a digital signal processor show the practical dynamic responses.

Usually, the order of the sensorless controller is the same to the state space equation of the power stage. However, the order of the controller can be reduced if a certain condition is satisfied. A low order controller has the merit of less computation volume or simpler circuit. In previous researches, ARE and LMI based $H\infty$ approaches have been introduced to design a low order controller, however, a quite complicated and exhaustive procedure is needed. Therefore, in this chapter, a robust $H\infty$ synthesis approach is also proposed to design a low order sensorless controller for boost converters, which need not solve any ARE or LMI, and parameterizes the controller by an adjustable parameter behaving like a 'knob' on the closed-loop characteristics. Simulations show the straightforward closed-loop characteristics evaluation and the closed-loop dynamic performance. Practical experiments on a digital signal processor give the practical dynamic responses.

Chapter 5 is the proposed sliding mode observer (SMO) for the sensorless control of boost converters. For the SMO, a nonlinear output estimation error is fed back to it. Provided a bound on the magnitude of the disturbances is known, the SMO can force the estimation error to converge to zero in a finite time, which means the observer states can converge asymptotically to the actual system states. In this chapter, an improved discrete SMO is proposed for the sensorless control of boost converters to improve the dynamic performance. Simulations by Simulink and practical experiments on a digital signal processor are performed. It is shown that the dynamic performance of the boost converter is greatly improved by the proposed SMO-based sensorless control, compared with the LO-based sensorless control.

Chapter 6 concludes the thesis and gives the topics studied in future.

To my beloved wife and my lovely son

Acknowledgements

I wish to express the most sincere gratitude to Professor Tsutomu Yoshihara, my supervisor, for providing me with a lot of advices and guidance, and tremendous resources throughout the entire duration of my doctoral course.

I would also like to express my appreciation to Professor Toshihiko Yoshimasu and Professor Takahiro Watanabe for their guidance to my research.

I sincerely thank Section Chief Mr. Matsuda and KDC Chief Mr. Fujiwara in New Japan Radio Corporation for offering me the internship chance and apart-time job, and allowing me to use their development tool for free of charge until now.

I am also very grateful to Professor Abe in Kyushu Institute of Technology and Senior Researcher Tsukuda in International Centre for the Study of East Asian Development (ICSEAD) for helping me to study power electronics and write my papers.

I sincerely thank my wife Yingzhuo Liu, for making delicious meals every day and working hard to support my family.

A special thanks goes to my son “Tora Kun”. I could not persist in the doctoral course till now without his lovely smile.

My parents support me very much throughout my life and I thank them forever.

I also thank to other students in the laboratory. I sincerely thank some persons whose words inspired me very much.

Xutao LI
May, 2016

Contents

List of Figures

List of Tables

Glossary

I	Unit matrix
A^{-1}	Inverse of matrix A
A^T	Transpose of matrix A
$\mathrm{Im}(A)$	Range space of matrix A
$Ker(A)$	Kernel space of matrix A
$V^-(\Sigma)$	Weakly unobservable subspace of system Σ
$S^-(\Sigma)$	Strongly controllable subspace of system Σ

1

Introduction

1.1 Energy and Power Conversion

With the extensive use of electrical and electronical equipment, the power demand is rapidly increasing. Besides the development of new energy sources such as solar and wind power generation, effective power use is an important measure of easing the energy crisis. Before 1970s, the linear power regulator [1] achieving the voltage modulation by the voltage drop on a semiconductor device dominated the power supply, with a very low power conversion efficiency (40% ~ 50%). The switching mode power supplier (SMPS) [2] has a well-known higher power conversion efficiency (80% ~ 99%), which transmits power pulse by pulse through controlling the switch's ON and OFF. From 1970s, the SMPS began to replace the linear power supplier. During the 1980s, the power supply for computers was almost all updated to SMPS. From 1990s, the SMPS began to be widely applied to the electronic and electrical equipment, communication equipment, PBX and so on. From 2000s, the SMPS began to be used in a wider area such as digital TV, high speed locomotive, LED, ICT, solar and wind power generation, and it is taking a higher and higher ratio of the power suppliers.

The SMPS belongs to the power electronics field, which is concerned with the processing of electrical power using electronic devices. As illustrated in Fig. 1.1, in general, a switching converter contains power input and control input ports, and a power output port. The raw input power is processed as specified by the control input, yielding the conditioned output power. The SMPS are divided into four categories [2]:

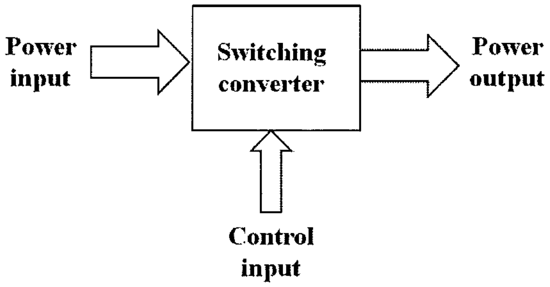

Fig. 1.1 A basic power processing block of a switching converter.

(1) DC/DC converter

In a DC/DC converter, the DC input voltage is converted to a DC output voltage having a larger or smaller magnitude, possibly with opposite polarity or with isolation of the input and output ground references.

(2) AC/DC converter

In an AC/DC converter, which is also called AC/DC rectifier, an AC input voltage is rectified, producing a DC output voltage. The DC output voltage and/or AC input current waveform may be controlled.

(3) DC/AC inverter

The inverse process, DC–AC inversion, involves transforming a DC input voltage into an AC output voltage of controllable magnitude and frequency.

(4) AC/AC converter

AC–AC conversion involves converting an AC input voltage to a given AC output voltage of controllable magnitude and frequency.

The DC/DC converter is an important power supplier, and it is the basis of researching other switching mode power suppliers.

1.2 Overview of DC/DC Switching Converters

According to the conversion ratio between input voltage and output voltage, the DC/DC switching converters are divided into three categories: buck, boost, and buck-boost converter. A buck converter converts an input high DC voltage to an output low DC voltage; a boost converter converts an input low DC voltage to an output high DC voltage; a buck-boost converter can convert an input voltage to an output voltage which is higher or lower than the input voltage. Taking a basic boost converter as an instance, it is shown in Fig. 1.2. The power stag is shown in Fig. 1.2 (a). When the switch S is ON, the inductor current will be charged by the input voltage v_g and the load R is charged by the capacitor C as shown in Fig. 1.2 (b). When the switch S is OFF, the input voltage will charge the capacitor C and the load

R as shown in Fig. 1.2 (c). When the circuit becomes steady, it can be deduced that the output voltage v_o is higher than the input voltage v_g through the volt-sec law of inductor L.

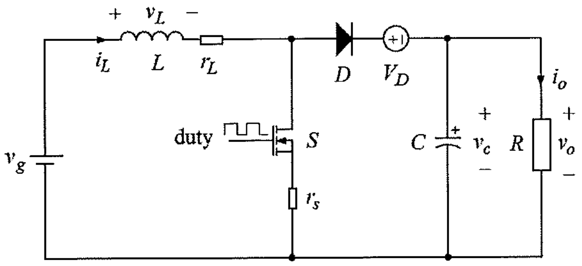

(a) Power stage of a boost converter

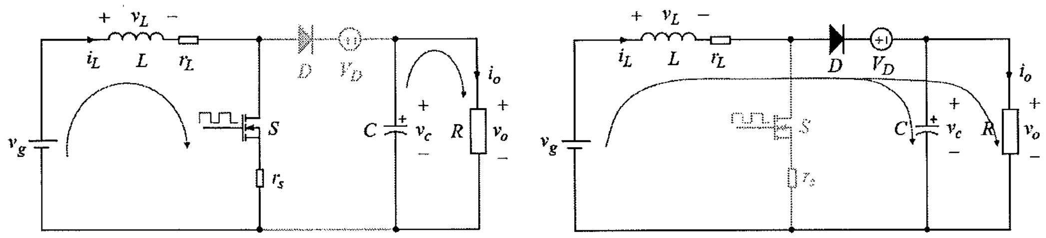

(b) Switch S is ON (b) Switch S is OFF

Fig. 1.2 A basic DC/DC boost switching converter.

1.2.1 Development history of DC/DC switching converters

Before the 1960s, the vacuum and semiconductor devices were placed between the input voltage and output voltage to achieve DC regulation. The vacuum and semiconductors behaves like variable resistors and therefore the power conversion efficiency was very low and large heat sink was necessary to exhaust the heat. As a result, the size and weight had been a big problem. From 1960s, along with the promotion of the project Apollo Moon Landing, small size and light weight began to be researched. In 1966, a paper “Basic Considerations for DC to DC Conversion Networks” written by Dr. E.T. Moore in America Duck university was published, and DC/DC converter began to be known. In 1968, a paper “Comparative Analysis of Chopper Voltage Regulators with LCV Filter” written by Soviets Dr. O.A. Kossov was published. This paper introduced three basic DC/DC converters called by step-down, step-up, and step-down-up converter, with their principles and steady state characteristics explained. Since then, the DC/DC converter research era really started.

Switching power suppliers belongs to power electronics. In 1973, the power electronics pioneer Dr. William E. Newell published a paper “Power Electronics-Emerging from Limbo” at the IEEE 73th Power Electronics Specialists Conference, and pointed out that power electronics is the constitute of electrical, electronic and control. In 1981, Dr. R.D. Middle Brook in America California University of Technology published a paper “Power

Electronics: An Emerging Discipline", and the voltage, current and frequency conversion was further explained.

From 1970s, the SMPS operating with a switching frequency over 20 kHz, which is much smaller size, lighter weight and higher efficiency than the conventional linear regulators, began to be widely applied to the advance field such as space development. Therefore, this period is also called the 20 kHz revolution era. After that, closely related to the information society taking shape under the support of integrated circuit technology and IT technology, and mainly for the power supplier of ICT (information, communication technology), the SMPS began to be more widely applied. From 2000s, the smart grid and green ICT began to be promoted. As its foundation, the research of renewable energy such as solar power generation and wind power generation become hot topic. For this reason, the SMPS becomes more necessary and exists almost everywhere.

1.2.2 Research topics of DC/DC switching converters

Nowadays, the DC/DC switching converters are developed towards the following trends [3] [4] [5]: small size, light weight, high power density, and low cost; high efficiency and high performance; low noise, low EMI; high reliability. To achieve these goals, some attractive technologies are as follows: high switching frequency, digital control, current sensorless control, soft-switching, integrated circuit technology, advance semiconductor materials, intelligent power module, etc.

(1) Small size, light weight, high power density, and low cost

Small size, light weight and low cost are demanded for many applications, such as LED driver, digital TV power supplier, portable equipment. The power density can also be improved if the size is reduced. Some technologies to achieve this goal are as follows:

- **High switching frequency**

The sizes of inductor and capacitor can be reduced through improving the switching frequency of a SMPS [6] [7]. Especially, the switching frequency can be very high with the performance of switch devices such as MOSFET, IGBT and IGCT improved fabricated by the advanced semiconductor materials [8]. However, EMI is the problem to be solved.

- **Integrated circuit technology**

For the low power converter, through integrating all the components of a switching converter into one chip [9], the size of the converter can be very small and the weight can be very light. Meanwhile, the wires connecting the components are shortened for an integrated converter, which means the parasitic parameters are reduced, so that the reliability can be improved.

- **Digital control**

In the past, the control part of a DC/DC switching converter is mainly implemented by a circuit. In recent years, the control part begins to be digitally implemented with the price decline in the digital signal processors including MCU, DSP and FPGA. The digital SMPS [10] [11] has many advantages. Firstly, it is easy to develop and modify the control part, so that the time-to-market can be shortened a lot. Secondly, it is very easy to implement a sophisticated algorithm to improve the performance. Thirdly, it is easy to add some functions such as communication to the system, while it is very difficult for the analog control. Lastly, a digital controller will not vary along with the environment, so that high stability and noise immunity can be maintained. It is also reported that a digital SMPS can reduce the PCB size of the converter [12] [13]. For these reasons, the digital control attracts more and more attentions, and more and more digital SMPS will be developed in future.

- **Sensorless current control**

For a boost, buck-boost, and fly-back switching converter, the current control is needed to improve the dynamic performance. However, it needs a current sensing circuit to detect the inductor current or capacitor current of the converter [14] [15]. A current sensing circuit has some drawbacks. Firstly, a current sensing circuit has many devices and occupies some PCB area. Secondly, the sensing result is affected by the switching noise. Thirdly, it is difficult to detect the current if the load changes in a large range. In contrast, current sensorless control of a switching converter has a contribution to the size, cost, and weight reduction [16] [17] [18], and the performance of a converter can also be improved because of the increased design freedom.

(2) High efficiency and high performance

Many applications, such as solar power generation and electric vehicles, have created an increased demand for high power densities and high efficiency in power converters. The power conversion efficiency improvement is focused on the following technologies:

- **Soft-switching technology**

During a switch changes from ON state to OFF state, or from OFF state to ON state, the overlap of the voltage and current of the switch causes a switching loss for the converter. To reduce the switching power loss, the soft-switching technology is widely used for the large power converters, including ZVS (zero voltage switching) and ZCS (zero current switching) technologies [19].

- **Advanced semiconductor materials**

The silicon carbide (SiC) [20] and gallium nitride (GaN) [21] are the candidates of greatly improving the efficiency in future, which have been the object of a growing interest over the past decade.

- **Advanced control algorithms**

The dynamic performance of a switching converter can be improved through adopting advanced control algorithms such as auto-tuning controller [22], sliding mode control [23], fuzzy controller [24], large signal nonlinear controller [25], and so on.

(3) Low noise, low EMI

One drawback of SMPS is the noise in the output voltage or output current. A random modulation method is proved to be effective in reducing the switching noise [26].

Electromagnetic emissions from power electronics has already become a very important issue, with the fact that the total power being processed by the converters is increasing rapidly. Standards and recommendations have come into effect internationally. The solution to this problem is critically dependent on the application, and presents enormous challenges and opportunities closely related to components, packaging, manufacturing, and cooling. Many researches proposed effective EMI reduction technologies such as soft-switching [27] and PCB layout [28].

(4) High reliability

Reliability is also an important index of a SMPS, which is related with the power supply risk and life span. Many researchers have given the reliability analysis of a switching converter [29], and some design considerations have also been provided [30]. Recently, intelligent power module [31] attracts many interests. For some applications, such as battery charge, pulse arc welding power supply, the power supplier must be program-like controlled in accordance with the work procedure. It means that the output of the power supplier may be changed among the several states: constant current/limited voltage, constant voltage/limited current, and constant current/constant voltage. An intelligent overheating protection and overvoltage protection is required to protect the power supplier itself.

1.3 Research purpose

For a boost, buck-boost and fly-back converter in continuous conduction mode, there is a right-half-plane-zero (RHPZ) in the transfer function from the duty ratio to the output voltage. This RHPZ severely restricts the crossover frequency of the open-loop gain, hence results in poor dynamic performance if single-loop voltage control is adopted. Multi-loop control is widely adopted to improve the dynamic performance. However, a current sensing circuit is required to detect the inductor current, which causes an increase of the cost, size and weight of the circuit. Current sensorless multi-loop control solves this problem by estimating the inductor current instead of the inductor current sensing circuit.

In the past, the controller of a converter is always implemented by a circuit. In recent years, the digital control, which means the control part is implemented on a digital signal processor such as MCU, DSP and FPGA, attracts many researchers' interests, because the digital SMPS has many advantages: a digital controller is easy to be modified, so that the time-to-market can be shortened a lot; it is very easy to implement a sophisticated control algorithm to improve the dynamic performance; it is easy to add some functions such as communication to the system, while it is very difficult for the analog control; a digital controller will not vary along with the environment, so that high stability and noise immunity can be maintained.

However, according to the authors' investigation, the design of current sensorless control for a boost, buck-boost or fly-back converter has not been well studied, although there are some contributions to the sensorless control of SMPS. Therefore, in this research, the topic focuses on the current sensorless digital control of DC/DC boost switching converters, with the purpose of contributing to small size, low cost, and light weight for switching converters. The controllers are implemented on a digital signal processor NJU20010.

2

Preliminaries to DC/DC Boost Switching Converters

The mathematical models of a switching converter can be firstly divided into two categories: peak value model [32] and average value model [33]. The average value model is very widely used to design a controller for a switching converter, and it can be divided into dc large signal average value model [25] and ac small signal average value model [33]. This research is based on the small signal average value model.

2.1 Principle of Small Signal Average Value Model of DC/DC Switching Converters

The behavior of a DC/DC switching converter is nonlinear, and its operation analysis is complex because of the periodic ON/OFF operation on the switches. In 1976, as the general analysis method, Dr. R.D. Middle Brook and CuK in America California University of Technology proposed the state space average value method for switching converters [33].

As a prerequisite of the state space average value model, it requires that the switching frequency f_s should be very higher than the resonant frequency f_r of the LC filter as follows:

$$f_s >> f_r \tag{2.1}$$

If the prerequisite in Eq. (2.1) is satisfied, the change of the inductor current and capacitor voltage in one switching period can be approximated as polygonal lines. Then, taking the average values of inductor current and capacitor voltage in one switching period as variables, the nonlinear operation of as DC/DC converter can be linearized.

As shown in Fig. 2.1, for a converter operating in inductor current continuous conduction mode (CCM), the circuit states can be divided into two working states: ON state and OFF state. Each state is linear and the state equations can be written in Eqs. (2.2) and (2.3).

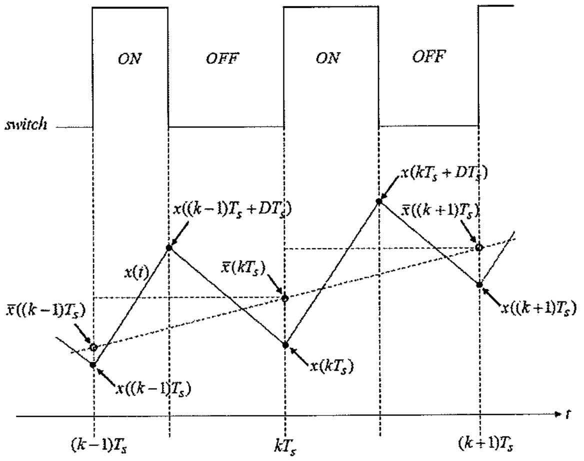

Fig. 2.1 State change in one period and its average value.

State 1: switch is ON

$$\begin{aligned} &\frac{dx(t)}{dt} = A_1x(t) + b_1V_g \qquad (kT_s \le t \le kT_s + DTs) \\ &y(t) = c_1x(t) \end{aligned} \tag{2.2}$$

State 2: switch is OFF

$$\begin{aligned} &\frac{dx(t)}{dt} = A_2x(t) + b_2V_g \qquad (kT_s + DTs \le t \le (k+1)T_s) \\ &y(t) = c_2x(t) \end{aligned} \tag{2.3}$$

where $x(t)$ is the system state incorporating some elements such as inductor current and capacitor voltage, and $y(t)$ is the output of the converter. The matrices A_1, b_1, c_1, A_2, b_2 and c_2 are determined by the converter parameters, and V_g is the input voltage. As shown in Fig. 2.1, if the switching frequency f_s is far larger than the natural resonant frequency f_r of the converter, the ON and OFF states are very short so that the state change in the two periods can be approximated as linear, and the final values at the end of each state are:

$$x(kT_s + DT_s) = x(kT_s) + \frac{dx(t)}{dt}\Big|_{t=kT_s} T_{ON} \tag{2.4}$$

$$x(k+1)T_s) = x(kT_s + DT_s) + \frac{dx(t)}{dt}\Big|_{t=kT_s+T_{ON}} T_{OFF} \tag{2.5}$$

where $D = T_{ON}/T_s$, $D' = T_{OFF}/T_s$. Denote I as a unit matrix. Substituting Eqs. (2.2) and (2.3) into Eqs. (2.4) and (5.5), the following equations can be obtained:

$$x(kT_s + DT_s) = [I + DT_s A_1]x(kT_s) + DT_s b_1 V_g \tag{2.6}$$

$$x((k+1)T_s) = [I + D'T_s A_2]x(kT_s + DT_s) + D'T_s b_2 V_g \tag{2.7}$$

Replacing k+1 by k in Eq. (2.7), an expression of $x(kT_s)$ can be obtained. Substituting this $x(kT_s)$ into Eq. (2.6) and ignoring the 2-order terms, the Eq. (2.8) is obtained. Similarly, substituting Eq. (2.6) into Eq. (2.7) and ignoring the 2-order terms, the Eq. (2.9) is obtained.

$$x(kT_s + DT_s) = (I + DT_s A_1 + D'T_s A_2)x((k-1)T_s + DT_s) + (DT_s b_1 + D'T_s b_2)V_g \tag{2.8}$$

$$x((k+1)T_s) = (I + DT_s A_1 + D'T_s A_2)x(kT_s) + (DT_s b_1 + D'T_s b_2)V_g \tag{2.9}$$

Replacing k+1 by k in Eq. (2.9), the following equation can be obtained:

$$x(kT_s) = (I + DT_s A_1 + D'T_s A_2)x((k-1)T_s) + (DT_s b_1 + D'T_s b_2)V_g \tag{2.10}$$

Then, adding Eqs. (2.8) and (2.10) and dividing by $D/2$, adding Eqs. (2.8) and (2.9) and dividing by $D'/2$, and adding the obtained two equations, an equation can be obtained as:

$$\begin{aligned}\frac{D[x(kT_s) + x(kT_s + DT_s)] + D'[x(kT_s + DT_s) + x((k+1)T_s]}{2} &= (I + DT_s A_1 + D'T_s A_2) \\ &\quad \frac{D[x((k-1)T_s) + x((k-1)T_s + DT_s)] + D'[x((k-1)T_s + DT_s) + x(kT_s]}{2} \\ &\quad + (DT_s b_1 + D'T_s b_2)V_g\end{aligned} \tag{2.11}$$

The average state values in one switching period T_s shown in Fig. 2.1 are written as:

$$\begin{aligned}\bar{x}(kT_s) &= \frac{1}{T_s}\int_{(k-1)T_s}^{kT_s} x(t)dt \\ &= \frac{D[x((k-1)T_s)+x((k-1)T_s+DT_s)]+D'[x((k-1)T_s+DT_s)+x(kT_s]}{2}\end{aligned} \tag{2.12}$$

$$\begin{aligned}\bar{x}((k+1)T_s) &= \frac{1}{T_s}\int_{T_s}^{(k+1)T_s} x(t)dt \\ &= \frac{D[x(kT_s)+x(kT_s+DT_s)]+D'[x(kT_s+DT_s)+x((k+1)T_s]}{2}\end{aligned} \tag{2.13}$$

From Eqs. (2.11), (2.12) and (2.13), the state average value equation is obtained as:

$$\frac{x((k+1)T_s)-x(kT_s)}{T_s} = (DA_1 + D'A_2)\bar{x}(kT_s) + (Db_1 + D'b_2)V_g \tag{2.14}$$

As shown in Fig. 2.1, replacing the discrete time kT_s by continuous time t in Eq. (2.14), the state average value equation of a DC/DC converter is obtained in Eq. (2.15). Similarly, the output average value equation is obtained in Eq. (2.16).

$$\frac{d\bar{x}(t)}{dt} = A\bar{x}(t) + bV_g \tag{2.15}$$

$$\bar{y} = c\bar{x}(t) \tag{2.16}$$

where

$$A = DA_1 + D'A_2,\quad b = Db_1 + D'b_2,\quad c = Dc_1 + D'c_2$$

(1) Steady state characteristics

From Eqs. (2.15) and (2.16), the steady state characteristics of a converter are as follows:

$$\begin{aligned} X &= -A^{-1}bV_g \\ Y &= -cA^{-1}bV_g \end{aligned} \tag{2.17}$$

(2) Small signal average value characteristics

Giving a small fluctuation on the input voltage *Vg*, duty ratio *D* and load *R*, small fluctuations on the state and output will also appear. This is written as follows:

$$\begin{cases} \bar{x}(t) = X + \Delta X(t) \\ \bar{y}(t) = Y + \Delta Y(t) \end{cases} \tag{2.18}$$

$$\begin{cases} v_g = V_g + \Delta V_g \\ \Re = R + \Delta R \\ d = D + \Delta D \end{cases} \tag{2.19}$$

Rewriting Eqs. (2.15) and (2.16) by Eqs. (2.18) and (2.19), and using the Eq. (2.20), the Eqs. (2.21) and (2.22) can be obtained.

$$\frac{\partial A}{\partial D} = A_1 - A_2,\ \frac{\partial b}{\partial D} = b_1 - b_2,\ \frac{\partial c}{\partial D} = c_1 - c_2 \tag{2.20}$$

$$\frac{d(X+\Delta X)}{dt} = (A + (A_1 - A_2)\Delta D + \frac{\partial A}{\partial R}\Delta R)(X + \Delta X) + (b + (b_1 - b_2)\Delta D)(V_g + \Delta V_g) \tag{2.21}$$

$$Y + \Delta Y = (c + (c_1 - c_2)\Delta D + \frac{\partial c}{\partial R}\Delta R)(X + \Delta X) \tag{2.22}$$

Ignoring the 2-order terms, Eqs. (2.21) and (2.22) are rewritten as follows:

$$\frac{d\Delta X}{dt} = A\Delta X + [(A_1 - A_2)X + (b_1 - b_2)V_g]\Delta D + b\Delta V_g + \frac{\partial A}{\partial R}X\Delta R \tag{2.23}$$

$$\Delta Y = c\Delta X + (c_1 - c_2)X\Delta D + \frac{\partial c}{\partial R}X\Delta R \tag{2.24}$$

Equations (2.23) and (2.24) are the small signal average value model of a switching converter. Through Laplace transformation of Eqs. (2.23) and (2.24), the following equations are obtained:

$$\Delta X(s) = (sI - A)^{-1}\{b\Delta V_g(s) + [(A_1 - A_2)X + (b_1 - b_2)V_g]\Delta D(s) + \frac{\partial A}{\partial R}X\Delta R(s)\} \tag{2.25}$$

$$\Delta Y(s) = c\Delta X(s) + (c_1 - c_2)X\Delta D(s) + \frac{\partial c}{\partial R}X\Delta R(s) \tag{2.26}$$

The Eqs. (2.25) and (2.26) are used to analyze the dynamic characteristics of the power conversion stage, and to design the controller for the power conversion.

2.2 Small Signal Average Value Model of Boost Converters

The power stage of a basic boost converter is shown in Fig. 2.2, with several parasitic parameters considered. The equivalent circuits when the switch S is ON/OFF are shown in Fig. 2.3. The waveforms when the boost converter operates in CCM are shown in Fig. 2.4.

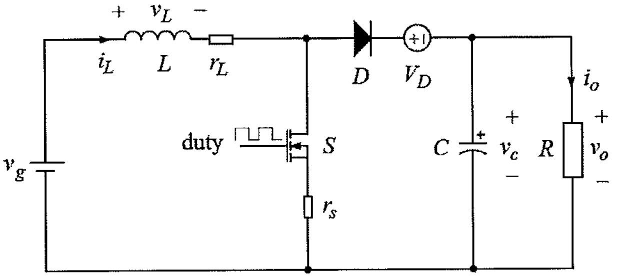

Fig. 2.2 The power stage of a basic boost converter.

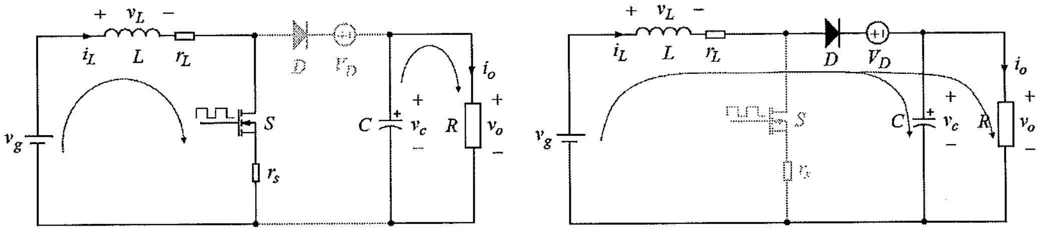

(a) circuit state when S is ON (b) circuit state when S is OFF

Fig. 2.3 Circuit states when S is ON/OFF.

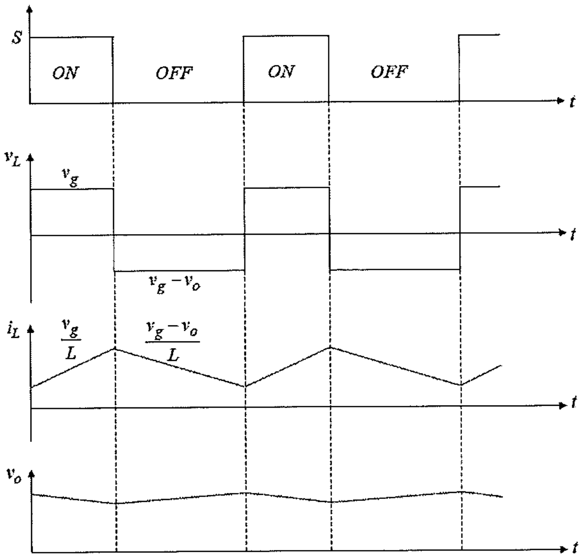

Fig. 2.4 Current and voltage waveforms of a boost converter in CCM.

For the boost converter in Fig. 2.2, the equivalent series resistor of the output capacitor is ignored, so the capacitor voltage v_c is the same to the output voltage v_o. The state space equations when S is ON and OFF are given in Eqs. (2.27) and (2.28), respectively.

State I: S is ON

$$\begin{bmatrix} \dot{i}_L \\ \dot{v}_o \end{bmatrix} = A_1 \begin{bmatrix} i_L \\ v_o \end{bmatrix} + B_1 \begin{bmatrix} v_g \\ v_D \end{bmatrix} = \begin{bmatrix} -\dfrac{r_L + r_s}{L} & 0 \\ 0 & -\dfrac{1}{RC} \end{bmatrix} \begin{bmatrix} i_L \\ v_o \end{bmatrix} + \begin{bmatrix} \dfrac{1}{L} & 0 \\ 0 & 0 \end{bmatrix} \begin{bmatrix} v_g \\ v_D \end{bmatrix} \tag{2.27}$$

State II: S is OFF

$$\begin{bmatrix} \dot{i}_L \\ \dot{v}_o \end{bmatrix} = A_2 \begin{bmatrix} i_L \\ v_o \end{bmatrix} + B_2 \begin{bmatrix} v_g \\ v_D \end{bmatrix} = \begin{bmatrix} -\dfrac{r_L}{L} & -\dfrac{1}{L} \\ \dfrac{1}{C} & -\dfrac{1}{RC} \end{bmatrix} \begin{bmatrix} i_L \\ v_o \end{bmatrix} + \begin{bmatrix} \dfrac{1}{L} & -\dfrac{1}{L} \\ 0 & 0 \end{bmatrix} \begin{bmatrix} v_g \\ v_D \end{bmatrix} \tag{2.28}$$

Substituting Eqs. (2.27) and (2.28) into Eq. (2.15), the corresponding state space average value model of the boost converter in Fig. 2.2 is written as follows:

$$\begin{bmatrix} \dot{i}_L \\ \dot{v}_o \end{bmatrix} = A \begin{bmatrix} i_L \\ v_o \end{bmatrix} + B \begin{bmatrix} v_g \\ v_D \end{bmatrix} = \begin{bmatrix} -\dfrac{r_L + Dr_s}{L} & -\dfrac{D'}{L} \\ \dfrac{D'}{C} & -\dfrac{1}{RC} \end{bmatrix} \begin{bmatrix} i_L \\ v_o \end{bmatrix} + \begin{bmatrix} \dfrac{1}{L} & -\dfrac{D'}{L} \\ 0 & 0 \end{bmatrix} \begin{bmatrix} v_g \\ v_D \end{bmatrix} \tag{2.29}$$

2.2.1 Steady state characteristics

From Eqs. (2.17) and (2.29), the steady state characteristics are obtained as follows:

$$I_L = \frac{V_g - D'V_D}{r_L + Dr_s + D'^2 R} \tag{2.30}$$

$$V_o = \frac{D'R(V_g - D'V_D)}{r_L + Dr_s + D'^2 R} \tag{2.31}$$

Denote the reference output voltage as V_{ref}. From Eq. (2.31), the duty ratio at the steady state is given as follows:

$$D' = \frac{r_s V_{ref} + RV_g}{2R(V_{ref} + V_D)}(1 + \sqrt{1 - \frac{4R(r_L + r_s)(V_{ref} + V_D)V_{ref}}{(r_s V_{ref} + RV_g)^2}}) \tag{2.32}$$

2.2.2 Small signal dynamic characteristics

Substituting Eq. (2.29) into Eqs. (2.23) and (2.24), the small signal average value model of the boost converter in Fig. 2.2 is given as follows:

$$\begin{aligned} \dot{x} &= Ax + B\hat{d} + Ew \\ y &= cx \end{aligned} \tag{2.33}$$

where $x = [\hat{\imath}_L \quad \hat{v}_o]$ and $w = [\hat{v}_g \quad \hat{\imath}_o]$ are the small signals, and

$$A = \begin{bmatrix} -\dfrac{r_L + Dr_s}{L} & -\dfrac{D'}{L} \\ \dfrac{D'}{C} & -\dfrac{1}{RC} \end{bmatrix}, \quad B = \begin{bmatrix} \dfrac{(D'R - r_s)V_g + (r_s + r_L)V_D}{L(r_L + Dr_s + D'^2 R)} \\ -\dfrac{V_g - D'V_D}{C(r_L + Dr_s + D'^2 R)} \end{bmatrix}$$

$$E = \begin{bmatrix} \dfrac{1}{L} & 0 \\ 0 & -\dfrac{1}{C} \end{bmatrix}, \quad c = \begin{bmatrix} 0 & 1 \end{bmatrix}$$

For the small signal model given in Eq. (2.33), its equivalent circuit model is written in Fig. 2.5, which gives a clear understanding of the small signal relations.

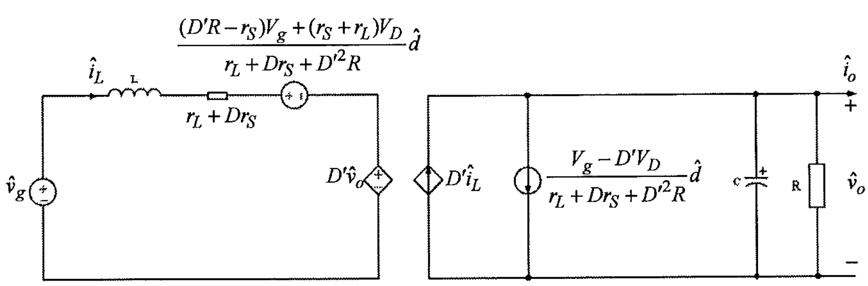

Fig. 2.5 Equivalent small signal model of the boost converter in CCM.

For expression convenience, denote the matrices A, B and E in Eq. (2.33) as follows:

$$A=\begin{bmatrix} a_{11} & a_{12} \\ a_{21} & a_{22} \end{bmatrix},\ B=\begin{bmatrix} b_1 \\ b_2 \end{bmatrix},\ E=\begin{bmatrix} e_1 & 0 \\ 0 & e_2 \end{bmatrix}$$

From Eqs. (2.25) and (2.33), the small signal transfer functions of the boost power conversion stage are as follows:

$$F_1=\frac{\hat{v}_o(s)}{\hat{v}_g(s)}=\frac{a_{21}e_1}{s^2-(a_{11}+a_{22})s+a_{11}a_{22}-a_{12}a_{21}} \tag{2.34}$$

$$F_2=\frac{\hat{v}_o(s)}{\hat{d}(s)}=\frac{b_2s+a_{21}b_1-a_{11}b_2}{s^2-(a_{11}+a_{22})s+a_{11}a_{22}-a_{12}a_{21}} \tag{2.35}$$

$$F_3=\frac{\hat{i}_L(s)}{\hat{v}_g(s)}=\frac{e_1s-e_1a_{22}}{s^2-(a_{11}+a_{22})s+a_{11}a_{22}-a_{12}a_{21}} \tag{2.36}$$

$$F_4=\frac{\hat{i}_L(s)}{\hat{d}(s)}=\frac{b_1s+a_{12}b_2-a_{22}b_1}{s^2-(a_{11}+a_{22})s+a_{11}a_{22}-a_{12}a_{21}} \tag{2.37}$$

$$F_5=\frac{\hat{i}_L(s)}{\hat{i}_o(s)}=\frac{a_{12}e_2}{s^2-(a_{11}+a_{22})s+a_{11}a_{22}-a_{12}a_{21}} \tag{2.38}$$

$$Z_p=\frac{\hat{v}_o(s)}{\hat{i}_o(s)}=\frac{e_2s-a_{11}e_2}{s^2-(a_{11}+a_{22})s+a_{11}a_{22}-a_{12}a_{21}} \tag{2.39}$$

From the characteristic equation $\Delta = s^2 - (a_{11} + a_{22})s + a_{11}a_{22} - a_{12}a_{21}$ of the above transfer functions, the natural resonant frequency and damp ratio of the boost converter in Fig. 2.2 are given in Eq. (2.40) and (2.41), respectively.

$$\omega_r=\sqrt{\frac{r_L+Dr_s+D'^2R}{RLC}} \tag{2.40}$$

$$\xi=\frac{RC(r_L+Dr_s)+L}{2\sqrt{RLC(r_L+Dr_s+D'^2R)}} \tag{2.41}$$

The above small signal transfer functions are used to analyze the characteristics of the power stage, and to design a controller as well as control loop characteristics analysis.

2.3 Analysis of DC/DC Boost Power Conversion System

The controller of a converter should first guarantee that the power conversion is stable under all operating conditions, and secondly that the desired dynamic performance is maintained when a disturbance occurs in the circuit. The closed-loop stability can be evaluated through examining its open-loop characteristics, and the closed-loop dynamic performance can be evaluated through examining the closed-loop dynamic characteristics [34] [35].

2.3.1 Single-loop control

The single-loop output voltage control of a boost converter is shown in Fig. 2.6, and its small signal block diagram is shown in Fig. 2.7. The symbols F_1, F_2, F_3, F_4, F_5, and Z_p are the transfer functions given in subsection 2.3, and F_c is the transfer function of a controller.

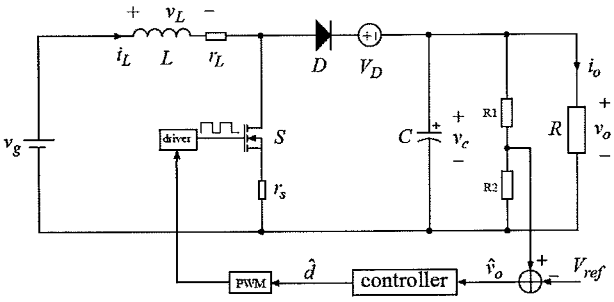

Fig. 2.6 Single-loop control of a boost converter.

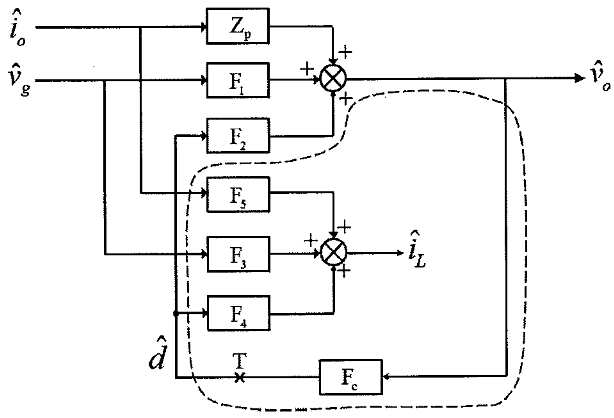

Fig. 2.7 Block diagram of single-loop control.

Breaking the loop at the point T, the open-loop transfer function is written as follows:

$$G_{op}(s) = F_2 F_c \tag{2.42}$$

The closed-loop stability can be evaluated through examining the characteristics of $G_{op}(s)$, for example through drawing its Bode plot, Nyquist plot, or root locus. From Fig. 2.7, the closed-loop characteristics including audio-susceptibility and output impedance are given in Eqs. (2.43) and (2.44), respectively.

$$\left.\frac{\hat{v}_o(s)}{\hat{v}_g(s)}\right|_{cl} = \frac{F_1}{1 - G_{op}(s)} = \frac{F_1}{1 - F_2 F_c} \tag{2.43}$$

$$\left.\frac{\hat{v}_o(s)}{\hat{i}_o(s)}\right|_{cl} = \frac{Z_p}{1 - G_{op}(s)} = \frac{Z_p}{1 - F_2 F_c} \tag{2.44}$$

The closed-loop characteristics of the inductor current are given in Eqs. (2.45) and (2.46).

$$\left.\frac{\hat{i}_L(s)}{\hat{v}_g(s)}\right|_{cl} = \frac{F_3 + F_c(F_1 F_4 - F_2 F_3)}{1 - G_{op}(s)} = \frac{F_3 + F_c(F_1 F_4 - F_2 F_3)}{1 - F_2 F_c} \tag{2.45}$$

$$\left.\frac{\hat{i}_L(s)}{\hat{i}_o(s)}\right|_{cl} = \frac{F_5 + F_c(Z_p F_4 - F_2 F_5)}{1 - G_{op}(s)} = \frac{F_5 + F_c(Z_p F_4 - F_2 F_5)}{1 - F_2 F_c} \tag{2.46}$$

From the above Eqs. (2.43), (2.44), (2.45), and (2.46), it can be seen that the closed-loop dynamic characteristics are directly related with the gain of the controller F_c, so that the controller design is a simple work for the single-loop control.

The proportional-integral-derivative (PID) controllers [22] are most widely adopted in the switching mode power suppliers, because it is easy understanding, simple to use, and capable of providing a high cost/benefit ratio. The most widely used PID controller is written in Eq. (2.47).

$$d(t) = K_p e + K_I \int e + K_D \dot{e} \tag{2.47}$$

where $e = V_{ref} - v_o$, and V_{ref} is the reference output voltage.

The boost converter with parameters listed in Table 2.1 is used in this research. From Eq. (2.40), the natural resonant frequency of this boost converter is $f_r = 2.1631$ kHz. The transfer function of Eq. (2.47) can be written as $f_c = K_D(s+z_1)(s+z_2)/s$, where z_1 and z_2 are the zeros. Setting $z_1 = 0.7\times2\pi\times f_r$ and $z_2 = 2\pi\times f_r$, and tuning the open-loop gain given in Eq. (2.42), a PID controller is obtained in Eq. (2.48).

Table 2.1 Parameters of a boost converter.

Input voltage	$v_g = 10$ V
Output voltage	$v_o = 20$ V
Output capacitor	$C = 1000$ μF
Inductor	$L = 47$ μH, $r_L = 24$ mΩ
Load	$R = 25$ Ω
Switch	$r_S = 36$ mΩ
Diode	$V_D = 1.25$ V
Switching frequency	$f_s = 150$ kHz

$$F_c = 0.5516 + 491.2952\frac{1}{s} + 0.0001s \tag{2.48}$$

The bode plot of the open-loop transfer function $G_{op}(s)$ is shown in Fig. 2.8. The open loop has a crossover frequency $f_c = 5.2$ kHz which is 1/28.8 of f_s and 1/3.8 of $f_z = 19.4$ kHz, where f_z is the frequency of the zero in Eq. (2.35), and a phase margin of 70.3^0.

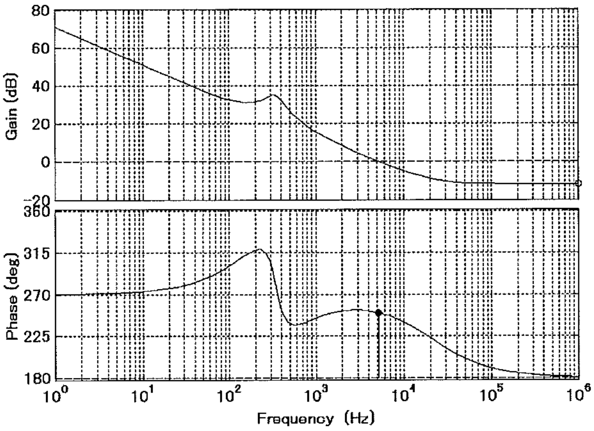

Fig. 2.8 Bode plot of open-loop $G_{op}(s)$.

The closed-loop characteristics of output voltage written in Eqs. (2.43) and (2.44) are shown in Figs. 2.9 (a) and (b), respectively, and the step responses of output voltage to a step change in the input voltage and the load current are shown in Figs. 2.10 (a) and (b), respectively. The closed-loop characteristics of inductor current given in Eqs. (2.45) and

(2.46) are shown in Figs. 2.11 (a) and (b), respectively, and the step responses of inductor current to a step change in the input voltage and the load current are shown in Figs. 2.12 (a) and (b), respectively.

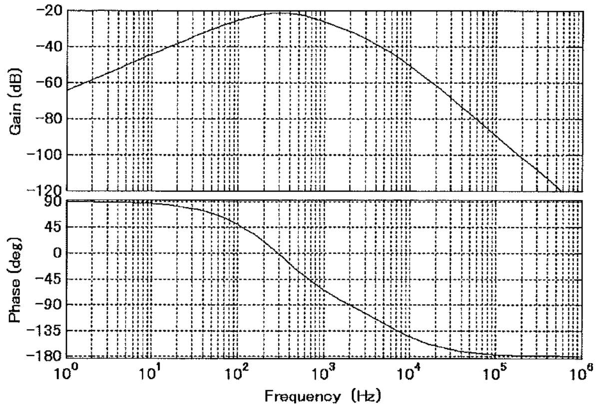

(a) Closed-loop audio-susceptibility ($\hat{v}_o/\hat{v}_g$)

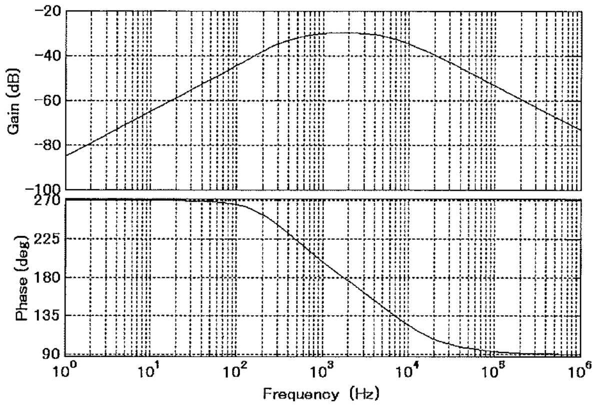

(b) Closed-loop output impedance ($\hat{v}_o/\hat{i}_o$)

Fig. 2.9 Bode plots of closed-loop dynamic characteristics (output voltage).

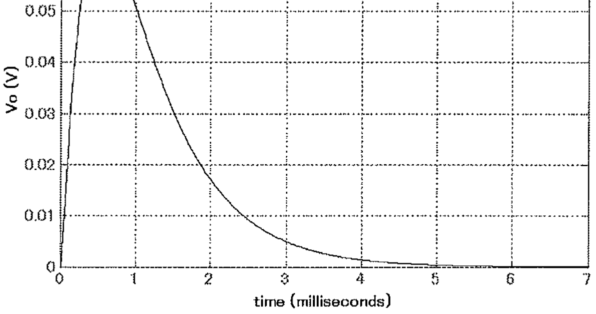

(a) Step response of $\hat{v}_o$ to a step change in $\hat{v}_g$

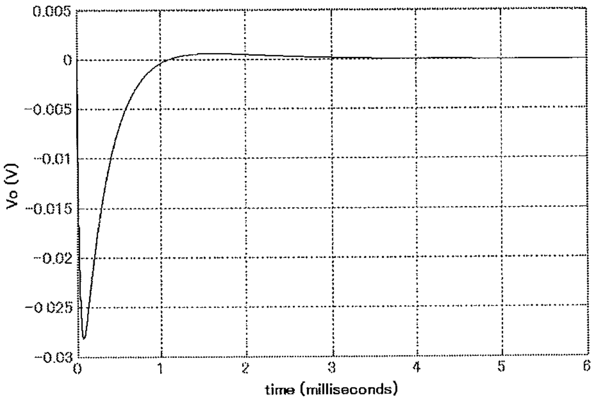

(b) Step response of $\hat{v}_o$ to a step change in $\hat{i}_o$

Fig. 2.10 Step responses of $\hat{v}_o$ to step changes in $\hat{v}_g$ and $\hat{i}_o$.

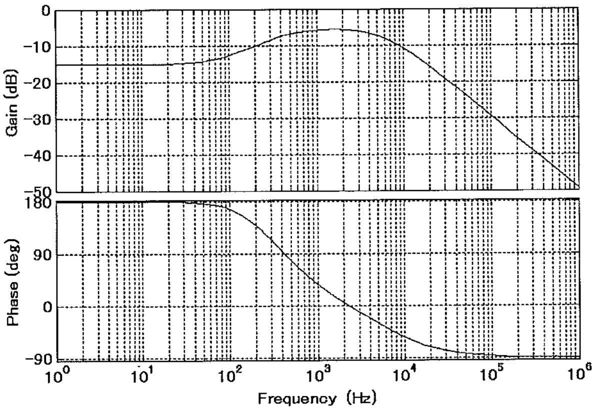

(a) Closed-loop audio-susceptibility ($\hat{i}_L/\hat{v}_g$).

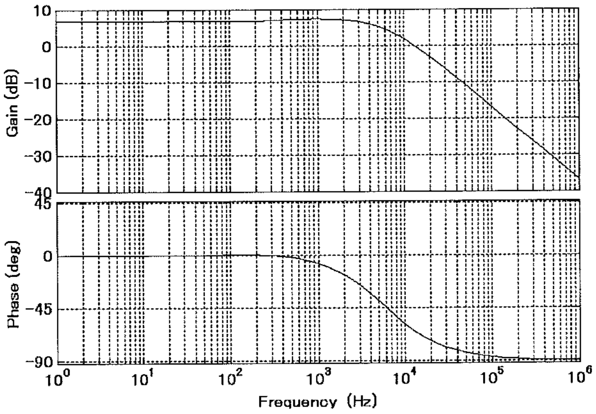

(b) Closed-loop output impedance ($\hat{i}_L/\hat{i}_o$).

Fig. 2.11 Bode plots of closed-loop dynamic characteristics (inductor current).

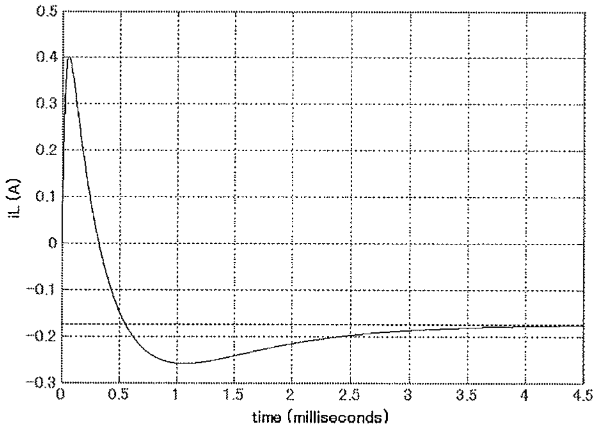

(a) Step response of $\hat{i}_L$ to a step change in $\hat{v}_g$

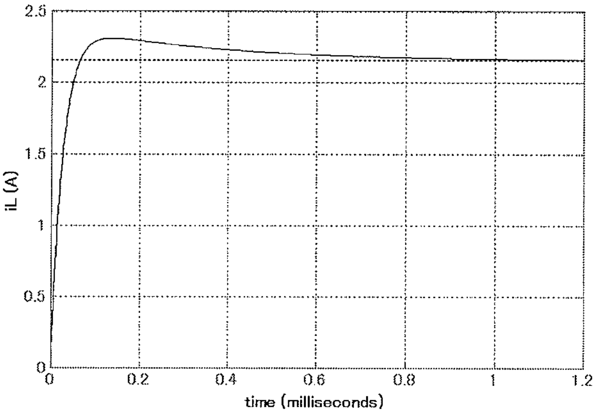

(b) Step response of $\hat{i}_L$ to a step change in $\hat{i}_o$.

Fig. 2.12 Step responses of $\hat{i}_L$ to step changes in $\hat{v}_g$ and $\hat{i}_o$.

2.3.2 Multi-loop control

The multi-loop control of a boost converter is shown in Fig. 2.13, which consists of an outer voltage control loop and an inner current control loop. The outer loop provides a reference inductor current for the inner loop.

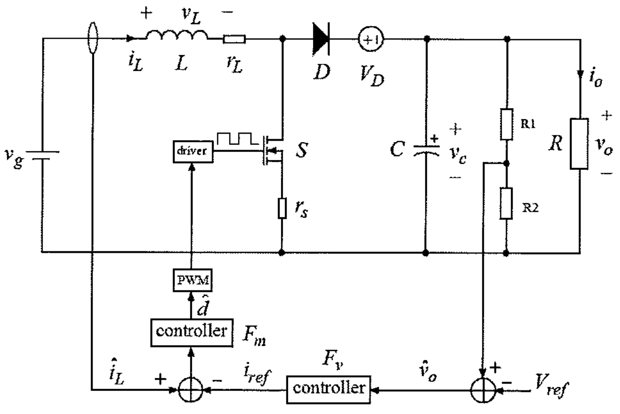

Fig. 2.13 Multi-loop control of a boost converter.

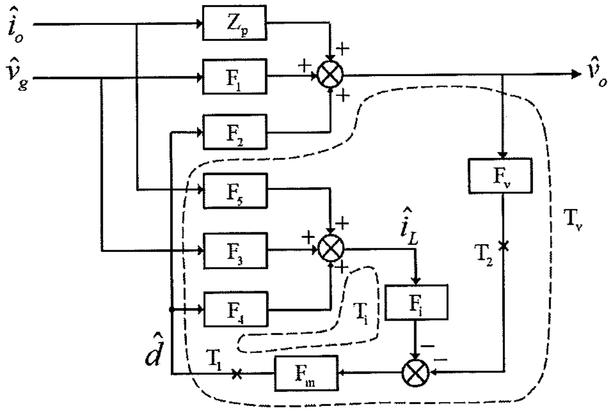

Fig. 2.14 Block diagram of multi-loop control.

The small signal block diagram of Fig. 2.13 is shown in Fig. 2.14. The symbols F_1, F_2, F_3, F_4, F_5, and Z_p are the transfer functions given in subsection 2.2, F_i is the transfer function of the inductor current sampling network, and F_m and F_v are the inner loop and outer loop compensators, respectively.

Denote the output voltage feedback path as $T_v = F_mF_vF_2$, and the inner current feedback path as $T_i = F_mF_iF_4$. Breaking the loop at the points T_1 and T_2, respectively, two open-loop transfer functions are given as follows:

$$T_1 = T_v + T_i \tag{2.49}$$

$$T_2 = \frac{T_v}{1+T_i} \tag{2.50}$$

here, the loop gain T_1 is called as the overall loop gain since it is measured inside both the current and voltage feedback loops, and the loop gain T_2 is called as the outer loop gain since it is measured outside of the current loop. The closed-loop stability can be evaluated through examining the characteristics of T_1 and T_2. From Fig. 2.14, the closed-loop characteristics including audio-susceptibility and output impedance are given in Eqs. (2.51) and (2.52), respectively.

$$\left.\frac{\hat{v}_o(s)}{\hat{v}_g(s)}\right|_{cl} = \frac{F_1 + T_i\left(F_1 - \frac{F_2F_3}{F_4}\right)}{1+T_i+T_v} \tag{2.51}$$

$$\left.\frac{\hat{v}_o(s)}{\hat{i}_o(s)}\right|_{cl} = \frac{Z_p + T_i(Z_p - \frac{F_2F_5}{F_4})}{1 + T_i + T_v} \tag{2.52}$$

The closed-loop characteristics of the inductor current are given in Eqs. (2.53) and (2.54).

$$\left.\frac{\hat{i}_L(s)}{\hat{v}_g(s)}\right|_{cl} = \frac{F_3 + T_v(F_3 - \frac{F_1F_4}{F_2})}{1 + T_i + T_v} \tag{2.53}$$

$$\left.\frac{\hat{i}_L(s)}{\hat{i}_o(s)}\right|_{cl} = \frac{F_5 + T_v(F_5 - \frac{F_4Z_p}{F_2})}{1 + T_i + T_v} \tag{2.54}$$

From the above Eqs. (2.49) and (2.50), it is known that the crossover frequency of the current loop gain T_i should be made high so that it dominates the overall loop gain T_1 at the crossover frequency, and gives it a 90^0 phase boost. This phase increase is critical to stabilize the boost, buck-boost, and fly-back converters which have additional phase delay of the voltage loop gain T_v due to the power stage right-half-plane-zero. From Eqs. (2.51), (2.52), (2.53) and (2.54), it can be seen that the closed-loop dynamic characteristics are not directly related with the loop gain T_i and T_v. Both T_i and T_v affect the closed-loop characteristics. This is very different from the single-loop control. Usually, the crossover frequency of the current loop should be larger than that of the voltage loop to obtain the full benefits of multi-loop control, and the gain of the current loop should be fairly low and the voltage loop gain should be much larger.

For the compensators F_m and F_v in Fig. 2.14, the proportional-integral (PI) controllers are adopted for the boost converter with parameters listed in Table 2.1. It is found that the following PI compensators guarantee the closed-loop stability and maintain good dynamic response of output voltage.

$$\begin{aligned} F_m &= 1.5 + 30.0/s \\ F_v &= 23.0 + 4.5 \times 10^4/s \end{aligned} \tag{2.55}$$

The Bode plots of loop gain T_1 and T_2 are shown in Fig. 2.15, and their characteristics are given as follows, where f_c is the gain crossover frequency, PM is the phase margin and GM is the gain margin:

$$\begin{aligned} &T_1 : f_c = 24.0kHz, PM = 72.1^o \\ &T_2 : f_c = 5.8kHz, PM = 60.3^o, GM = 10.7dB \end{aligned} \tag{2.56}$$

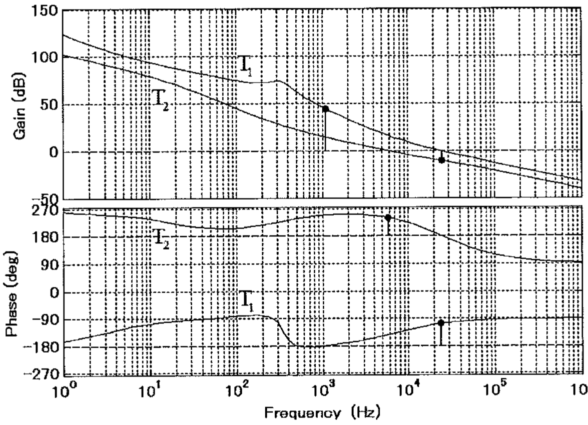

Fig. 2.15 Bode plots of open-loop gains at the points T_1 and T_2.

The closed-loop characteristics are shown in Fig. 2.16, and the step responses of output voltage to step changes in the input voltage and the load current are shown in Fig. 2.17 (a) and (b), respectively. Comparing Figs. 2.9 and 2.10 with Figs. 2.16 and 2.17, it can be seen that the closed-loop dynamic characteristics of the multi-loop are greatly improved and that the dynamic responses of output voltage are greatly improved than the single-loop control.

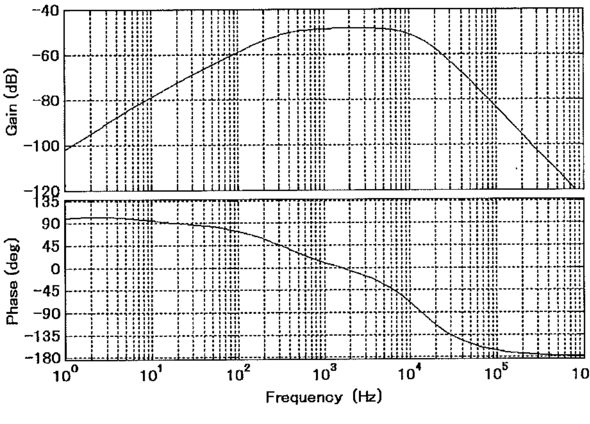

(a) Closed-loop audio susceptibility ($\hat{v}_o/\hat{v}_g$)

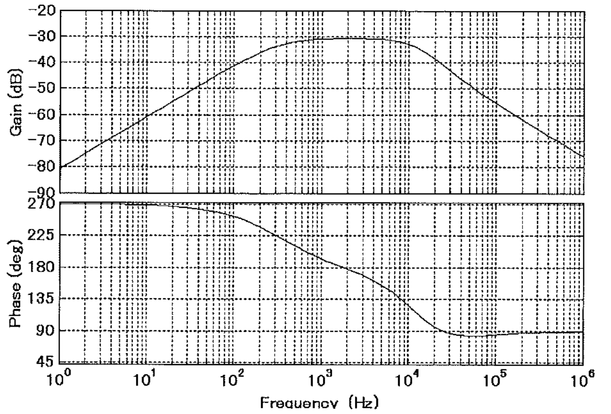

(b) Closed-loop output impedance ($\hat{v}_o/\hat{\imath}_o$)

Fig. 2.16 Bode plots of the closed-loop dynamic characteristics (output voltage).

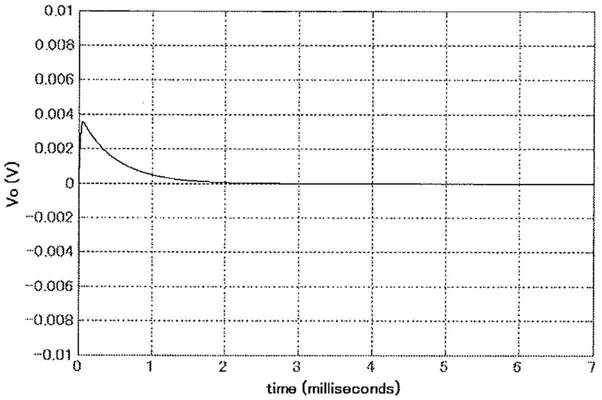

(a) Step response of $\hat{v}_o$ to a step change in $\hat{v}_g$

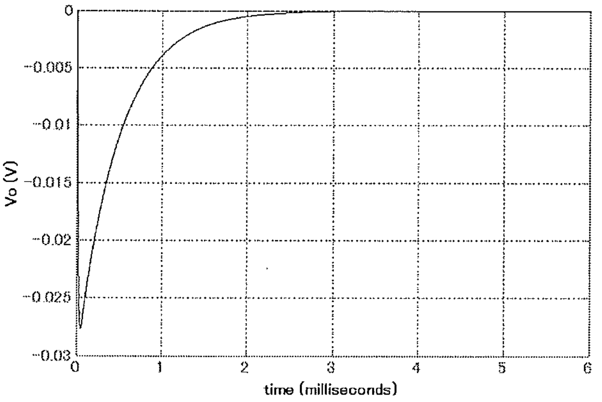

(b) Step response of $\hat{v}_o$ to a step change in $\hat{\imath}_o$.

Fig. 2.17 Step responses of $\hat{v}_o$ to step changes in $\hat{v}_g$ and $\hat{\imath}_o$.

The closed-loop dynamic characteristics of the inductor current are shown in Fig. 2.18, and the step responses of inductor current to step changes in the input voltage and the load current are shown in Fig. 2.19. Compared with Figs. 2.11 and 2.12, it can be seen that the dynamic performance of inductor current is also greatly improved by the multi-loop control. Therefore, the multi-loop control is widely adopted to control a boost converter. The situation is the same to buck-boost and fly-back converters which also have a positive zero in the transfer function from the duty ratio to the output voltage.

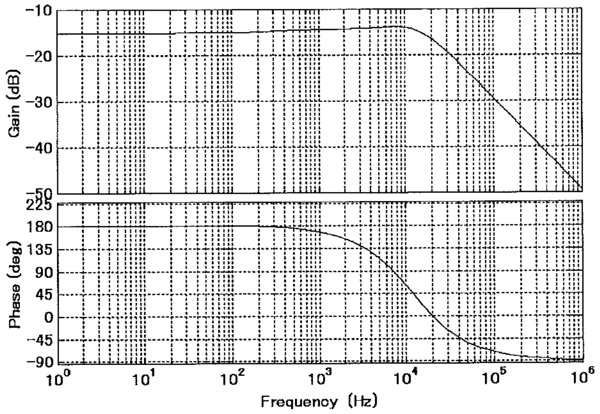

(a) Closed-loop audio susceptibility ($\hat{i}_L/\hat{v}_g$)

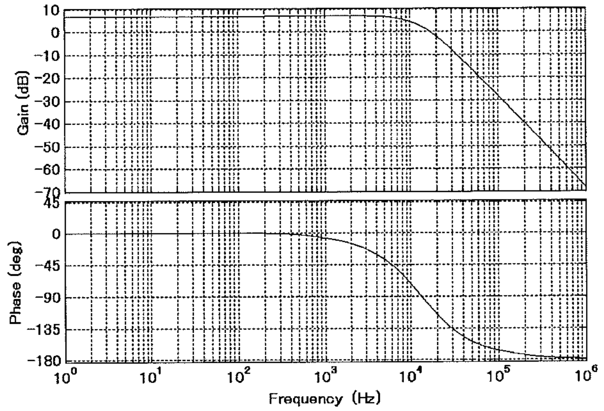

(b) Closed-loop output impedance ($\hat{i}_L/\hat{i}_o$)

Fig. 2.18 Bode plots of the closed-loop dynamic characteristics (inductor current).

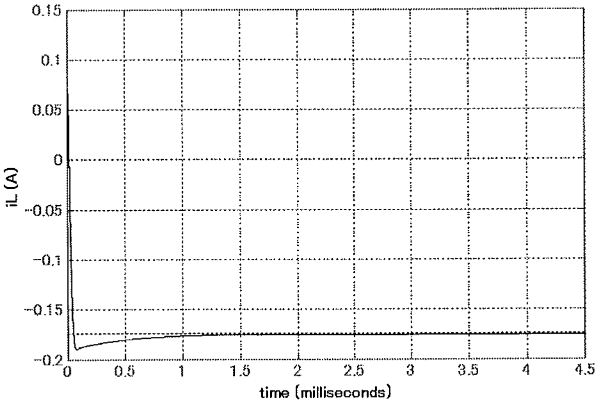

(a) Step response of $\hat{i}_L$ to a step change in $\hat{v}_g$

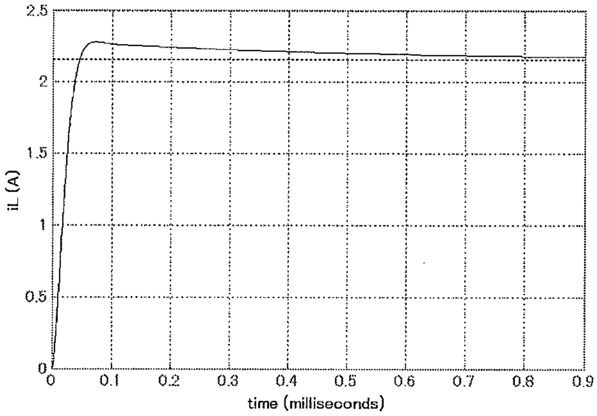

(b) Step response of $\hat{i}_L$ to a step change in $\hat{i}_o$

Fig. 2.19 Step responses of $\hat{i}_L$ to step changes in $\hat{v}_g$ and $\hat{i}_o$.

2.4 Introduction of Modern Robust Control Theory

The afore-described controller design method and the control system analysis are based on the classical control theory, which is very effective in analyzing a linear control system in frequency domain and is mainly finished before 1960s. From 1960s, many modern control theories began to be advocated and were well accomplished at the end of 1980. A brief development history of control theory is given in Fig. 2.20. In many modern control theories, the controller is directly designed based on the system state space equation. When applying the modern control theory to the SMPS, a featured quantity of a storage component is usually selected as a system state, such as the current of an inductor and the voltage of a capacitor. In this subsection, two important robust control theories adopted in this research are briefly introduced.

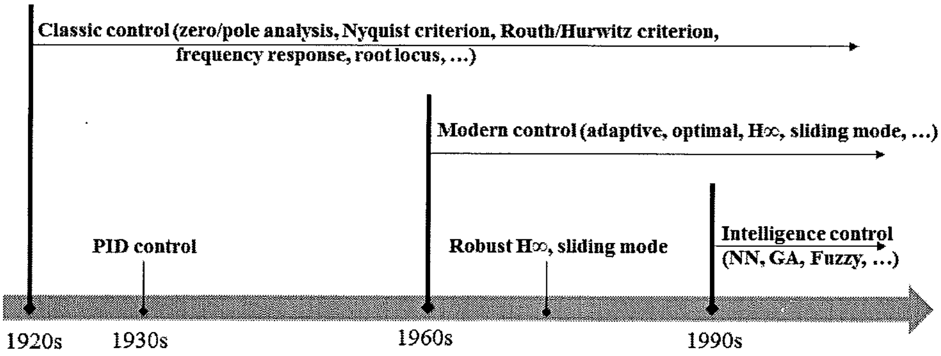

Fig. 2.20 Development history of control theory.

2.4.1 Robust H∞ control

The robust H∞ control was firstly formulated by Dr. G. Zames in 1981, and since then a great deal of work has been done on finding the solution to H∞ control problem. The block diagram of robust control is shown in Fig. 2.21, where *P* represents a linear time-invariant control object such as a boost converter and *C* represents a controller. The symbol *w* represents the disturbance acting on the control object *P*, *z* represents the controlled output which is to be minimized, *y* is the measurable output of *P* as well as the controller input, and *u* represents the controller output. A constraint imposed on *P* is that the mapping from *y* to *u* should be such that the closed-loop system is internally stable.

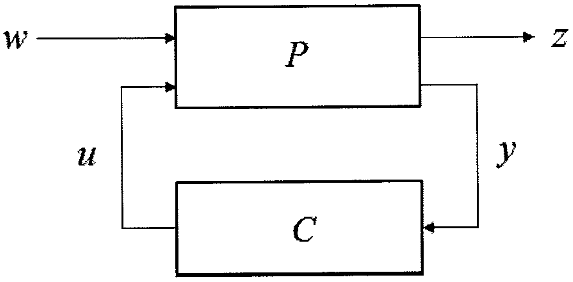

Fig. 2.21 Block diagram of robust H∞ control.

To design the controller *C* using robust H∞ control, a state space equation of the control object *P* should be first constructed which is always written as follows:

$$\begin{cases} \dot{x} = Ax + Bu + Ew \\ y = C_1 x + D_{11} u + D_1 w \\ z = C_2 x + D_2 u + D_{22} w \end{cases} \qquad (2.57)$$

where $x \in R^n$, $u \in R^m$, $w \in R^l$, $y \in R^q$ and $y \in R^q$. The matrices A, B, E, C_1, C_2, D_{11}, D_1, D_2 and D_{22} are of appropriate dimensions, and A, B, and E come from the physical description equation of the control object P, while the matrices C_1, D_1, C_2, D_2, D_{11} and D_{22} are determined by the type of the controller C. The following three controllers can be designed by the robust H∞ control:

$$u = Fx \qquad (2.58)$$

$$u = F_1 x + F_2 w \qquad (2.59)$$

$$\begin{cases} \dot{p} = Kp + Ly \\ u = Mp + Ny \end{cases} \qquad (2.60)$$

The controller in Eq. (2.58) is called as state feedback, which means that all the system states are available while the disturbance is unavailable. The controller in Eq. (2.59) is called as static feedback, which means that not only the system states are available but also the disturbance is available. The controller in Eq. (2.60) is called as output measurement feedback, which means that only some system states are available and some system states will be estimated. For the control in Eq. (2.60), if $D_{11} \neq 0$, it will not be unique for system in Eq. (2.57). The system in Eq. (2.60) is called as a well-posed system if $D_{11} = 0$. For a well-posed system, the closed-loop system of Eqs. (2.57) and (2.60) is written as follows:

$$\Sigma_{cl} : \begin{cases} \dot{x}_e = A_e x_e + E_e w \\ z = C_e x_e + D_e w \end{cases} \tag{2.61}$$

where $x_e = [x \quad p]$, and

$$A_e = \begin{bmatrix} A + BNC_1 & BM \\ LC_1 & K \end{bmatrix}, \quad B_e = \begin{bmatrix} E + BND_1 \\ LD_1 \end{bmatrix}$$

$$C_e = \begin{bmatrix} C_2 + D_2NC_1 & D_2M \end{bmatrix}, \quad D_e = D_2ND_1 + D_{22}$$

It is said the controller in Eq. (2.60) is internally stabilizing when applied to the system in Eq. (2.57) if the matrix A_e is asymptotically stable which means that all the eigenvalues of A_e are negative values. For the closed-loop system in Eq. (2.61), the transfer function from the disturbance w to the controlled output z is written as follows:

$$G_{cl}(s) = C_e(sI - A_e)^{-1} B_e + D_e \tag{2.62}$$

The solution of Eq. (2.60) can be derived through minimizing the H∞ norm of $G_{cl}(s)$. The H∞ norm of $G_{cl}(s)$ is defined as follows:

$$\left\| G_{cl}(s) \right\|_\infty = \sup_{\omega \in [0,\infty]} \sigma_{\max}[G_{cl}(j\omega)] = \sup_{\|w\|_2 = 1} \frac{\|z\|_2}{\|w\|_2} \tag{2.63}$$

where σ means the singular value of $G_{cl}(j\omega)$, sup is supremum, z and w are the output and input of $G_{cl}(s)$, respectively, and $\|z\|_2$ and $\|w\|_2$ are the l_2 norm of the continuous time signal z and w. The physical meaning of H∞ norm is that the effect of w on z after closing the loop is measured in terms of the energy and the worst disturbance w, and this measure is turned out to be equal to the closed-loop H∞ norm $G_{cl}(s)$, which is the supremum over all disturbances unequal to zero of the quotient of the energy flowing out of the system and the energy flowing into the system. The geometric explanation of $\|G_{cl}(s)\|_\infty$ is given in Fig. 2.22. It shows that the H∞ norm is the maximum gain of $\|G_{cl}(s)\|_\infty$ in the Bode plot as shown in Fig. 2. 22 (a), or the longest distance from the origin in the vector diagram as shown in Fig. 2. 22 (b).

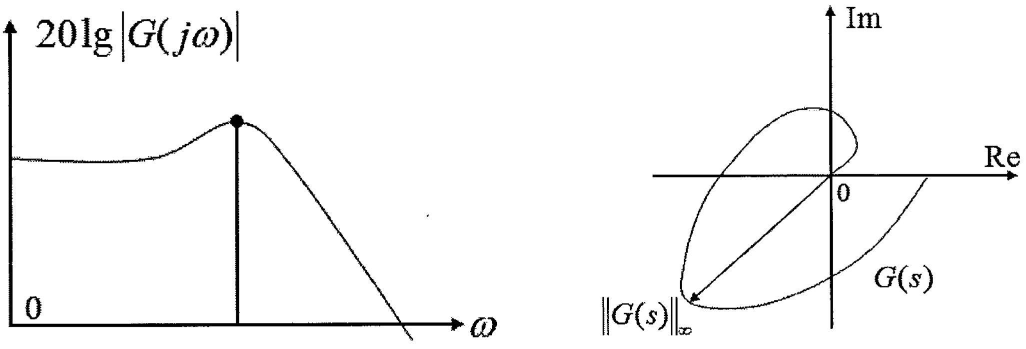

(a) Bode plot (b) Vector diagram

Fig. 2.22 Mathematical explanation of H∞ norm.

Since 1980s, many control theory researchers have contributed to finding a solution to the controller in Eq. (2.60). In the early 1980s, the researches focused on finding the solution in frequency domain, and the main drawback was that it yielded high order controllers. After that, researches began to move on the time-domain approach, the polynomial approach, the J-spectral factorization approach, etc. By far, the time-domain approach is very widely adopted since very elegant solution can be given by this approach. Mainly, there are two approaches to finding a solution to the controller in Eq. (2.60). One approach is based on solving the linear matrix inequalities (LMI), and the second approach is based on solving the algebraic Riccati equations (ARE). The solvability conditions for the system in Eq. (2.57) with the controller in Eq. (2.60) are as follows [36]:

I) (A, B_1) is stabilizable, and (C_1, A) is detectable;

II) (A, B_2) is stabilizable, and (C_2, A) is detectable;

III) $D_2^T[C_2 \quad D_2]=[0 \quad I]$;

IV) $\begin{bmatrix} B \\ D_1 \end{bmatrix} D_1^T = \begin{bmatrix} 0 \\ I \end{bmatrix}$;

V) $D_{11}=0, D_{22}=0$.

If the above conditions are satisfied, the ARE-based approach is as follows: Given a priori bound $\gamma > 0$, if there exists a stable semi-definite matrix P for the ARE in Eq. (2.64) and a stable semi-definite matrix Q for the ARE in Eq. (2.65), and P and Q satisfy the conditions in Eqs. (2.66), (2.67) and (2.68), then a solution to Eq. (2.60) is given in Eq. (2.69).

$$A^T P + PA + \gamma^{-2} PBB^T P - PEE^T P + C_2^T C_2 = 0 \tag{2.64}$$

$$AQ + QA^T + \gamma^{-2} QC_2^T C_2 Q - QC_1^T C_1 Q + BB^T = 0 \tag{2.65}$$

$$A + \gamma^{-2} BB^T P - EE^T P \quad \textit{is stable} \tag{2.66}$$

$$A^T + \gamma^{-2} C_2^T C_2 Q - C_1^T C_1 Q \quad \textit{is stable} \tag{2.67}$$

$$\rho(PQ) < \gamma^2 \tag{2.68}$$

$$\begin{cases} \overset{\bullet}{p} = Kp + Ly \\ u = Mp + Ny \end{cases} \tag{2.69}$$

where

$$K = A + \gamma^{-2} BB^T P - EE^T P - (I - \gamma^{-2} QP)^{-1} QC_1^T C_1$$

$$L = (I - \gamma^{-2} QP)^{-1} QC_1^T$$

$$M = -E^T P$$
$$N = 0$$

A discrete controller can be obtained through discretizing the controller in Eq. (2.69), or be designed using a discrete linear time-invariant system which is the discrete counterpart of Eq. (2.57).

2.4.2 Sliding mode control

Sliding mode control (SMC) is firstly introduced by the Soviet Dr. Utkin in 1977. In general, SMC is a class of nonlinear control and is dedicated to the robust control of variable structure systems [37]. It has a long development history and its potential applications in power converters have attracted much research attentions. The main idea of SMC is to predefine an ideal manifold for the state trajectory to travel along. This manifold is also known as "sliding surface" as shown by the s in Fig. 2.23 (a) which is an exemplary ideal sliding mode control system. Upon the satisfaction of certain criteria, the state trajectory is moved on the sliding surface as shown by the stage 2 in Fig. 2.23 (a) and is forced along it towards the origin, which is the equilibrium point where the control error is zero. Since the movement on the sliding surface is independent of the system disturbances, the control system exhibits constant dynamic behaviors even in the presence of disturbances, which is known as the "invariance property" of SMC. In the control of SMPS, this feather of robustness is reflected by the consistent steady state and transient response performances under all operation conditions.

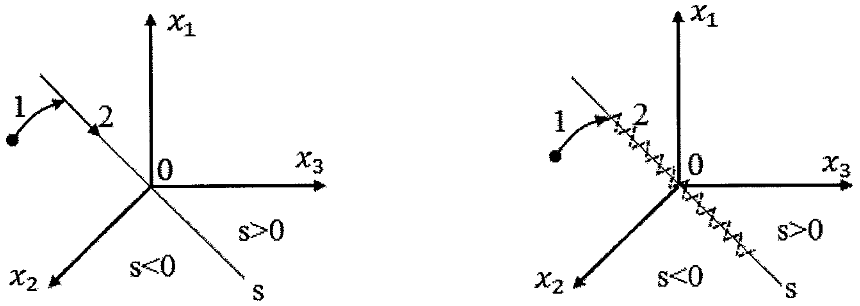

(a) ideal sliding mode trajectory (b) practical sliding mode trajectory

Fig. 2.23 An example of sliding mode control.

The SMC theory provides a solid framework for systematic derivation of robust control rules. The invariance property of SMC allows the application of equivalent control, so that facilitates the controller design. The SMC is hysteresis-like and the switching function cannot be directly applied to the derivation of the PWM control for a SMPS. However, applying the equivalent control in the SMC theory to the average value model based PWM control, a PWM quasi-sliding mode controller can be obtained, which has SMC advantage of high robust performance and yet operates at a fixed switching frequency. The SMC based derivation approach also provides insights into the design and optimization of the controller parameters through the manipulation of the sling surface equation.

Suppose a linear constant system is described by the following equation:

$$\dot{x} = Ax + Bu + g \tag{2.70}$$

where x is the system state, u is the scalar input, A and B are the constant matrices. Define a sliding surface as follows:

$$s = Cx \tag{2.71}$$

where C is a constant matrix. According to the equivalent control principle, there exists an equivalent control u_{eq} so that $ds/dt = 0$ is satisfied when the system states move along the sliding surface s. For the system in Eq. (2.70), the equivalent control u_{eq} is written as follows:

$$u_{eq} = -(CB)^{-1}(CAx + Cg) \tag{2.72}$$

The control strength in Eq. (2.72) guarantees that the system state moves along the sliding surface s towards the origin. However, the start point of the system state trajectory is always not on the sliding surface. So, the system state should be brought onto the sliding surface by an additional control strength u_{sw} as shown by the trajectory 1 in Fig. 2.23 (b). The trajectory in this period is called the reaching stage. Meanwhile, there always are some switch delays for a practical system, so that the system state cannot ideally slide along the sliding surface. The system state should be trapped into a small range of the sliding surface by the control strength u_{sw} as shown by the trajectory 2 in Fig. 2.23 (b), and the trajectory in this period is called sliding stage. The switch control part u_{sw} can use a sign function as follows:

$$u_{sw} = K\,\mathrm{sgn}(s) = \begin{cases} +K & \mathit{if}\ s(x) > 0 \\ -K & \mathit{if}\ s(x) < 0 \end{cases} \tag{2.73}$$

The total control u consists of the sum of u_{eq} and u_{sw} written as follow:

$$u = u_{eq} + u_{sw} \tag{2.74}$$

Define a Lyapunov function as follows:

$$V = \frac{1}{2}s^2 \tag{2.75}$$

According to the Lyapunov stability theorem, the system in Eq. (2.70) with the control in

Eq. (2.74) is asymptotically stable if the condition $dV/dt < 0$ is stratified. From this stability condition, the following global existence and reachable condition for the system in Eq. (2.70) with the control in Eq. (2.74) should be satisfied:

$$\dot{s}s < 0 \tag{2.76}$$

The condition in Eq. (2.76) adds a constraint on the parameters C and K.

The discrete sliding mode control is well presented by Furuta in 1990. Suppose a linear constant system can be described by the following discrete state equation:

$$x(k+1) = Ax(k) + Bu(k) + g \tag{2.77}$$

Define the sliding surface as $s(k) = Cx(k)$. According to the equivalent control $s(k+1) = s(k)$, the equivalent control strength can be obtained as follows:

$$u_{eq} = -(CB)^{-1}C[(A-I)x(k) + g] \tag{2.78}$$

Similar to the continuous SMC, the switching control strength u_{sw} is also needed. An important difference is that the stability condition is changed as follows:

$$\begin{aligned} &(s(k+1) - s(k))\operatorname{sgn} s(k) < 0 \\ &(s(k+1) + s(k))\operatorname{sgn} s(k) > 0 \end{aligned} \tag{2.79}$$

2.5 Conclusion

In this chapter, the small signal average value model of switching mode power suppliers is firstly introduced. Then, the small signal a boost converter is deduced. Based on the small signal model, the characteristics of the boost power stage are provided. The single-loop PID control and multi-loop PI control of the boost converter are compared, and it clearly shows that multi-loop control can improve the closed-loop dynamic performance. At last, the basic principles of modern control including the robust H∞ control and the sliding mode control are introduced.

3

Luenberger Observer Based Sensorless Multi-loop Control of Boost Converters

Sensorless multi-loop control reduces the cost, size and weight of a switching converter. The Luenberger observer (LO) is widely used to estimate the inductor current for the current sensorless control of a converter. In this chapter, a closed-loop characteristics evaluation method is proposed to design a LO-based sensorless multi-loop control for boost converters.

3.1 Introduction

The controller of a switching converter should firstly guarantee that the power conversion is stable under all operating conditions, and secondly that the desired dynamic performance is maintained when a disturbance occurs. The dynamic performance of a switching converter, whether it has single- or multi-loop control, is determined by its closed-loop characteristics including audio susceptibility and output impedance [38]. For a single-loop output voltage controlled buck converter or boost converter in discontinuous conduction mode, since the loop gain and crossover frequency are directly related with the closed-loop characteristics, the stability and dynamic performance can be guaranteed through making the loop gain as large as possible with a high crossover frequency and adequate phase and gain margins. Nevertheless, there is a right-half-plane-zero (RHPZ) in the transfer function from the duty ratio to the output voltage for a boost, buck-boost and fly-back converters in continuous conduction mode (CCM) [39]. This RHPZ severely restricts the crossover frequency of the open-loop gain, hence results in poor dynamic performance if single-loop voltage control is adopted. Multi-loop control is widely adopted to improve the dynamic performance. For the multi-loop control, the relationships between the closed-loop characteristics and the loop gains are generally indirect [34]. Minimizing the closed-loop characteristics involves an iterative process to make a trade-off between the loop gains, regardless of the peak current control [40] or average current control [41].

For the multi-loop control, the inductor or switch current should be sensed by a shunt resistor with an amplifier, a transformer or an active filter [14]. Taking a shunt resistor sensing circuit shown in Fig. 3.1 as an instance, it can be seen that a current sensing circuit will unavoidably increase the cost, size, and weight and cause a slight power loss. This is similar to the control of buck-boost and fly-back converters. Current sensorless multi-loop control solves this problem through a system state observer instead of the current sampling circuit [16] [17] [18].

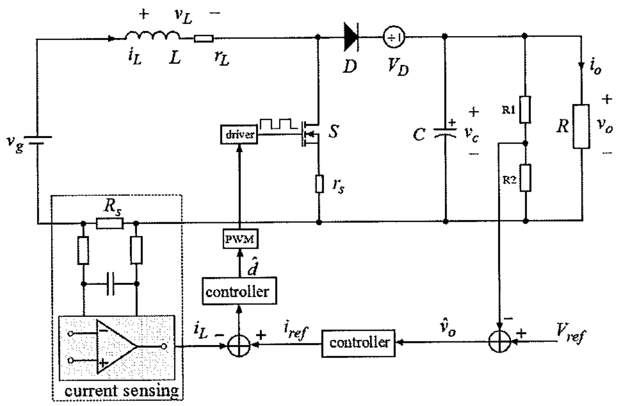

Fig. 3.1 Inductor current sensed multi-loop control of a boost converter.

The Luenberger observer (LO) [42] is very effective in estimating the inductor current for the sensorless control. However, since there are more parameters relating with the closed-loop characteristics for the LO-based sensorless multi-loop control, it is difficult to design an LO-based sensorless multi-loop control for a switching converter. Although the LO-based sensorless control has been introduced in previous papers [17] [43], the design of the LO as well as the controllers has not been well presented. Therefore, in this chapter, a closed-loop characteristics evaluation method is proposed to design the LO-based sensorless multi-loop control for boost converters. Simulations show the closed-loop characteristics evaluations. Practical experiments on a digital processor give the practical dynamic responses.

3.2 Analysis of LO-based Sensorless Multi-loop Control

3.2.1 Block diagram of LO-based sensorless multi-loop control

The sensorless multi-loop control of a boost converter is shown in Fig. 3.2, and its closed-loop block diagram is shown in Fig. 3.3 [44]. The control system consists of an outer loop T_v and an inner loop T_i. The outer loop provides a reference inductor current for the inner current loop. The symbols $\hat{v}_o$, $\hat{v}_g$, $\hat{i}_o$, and $\hat{i}_L$ are the small signals of the converter. F_1, F_2, F_3, F_4, F_5 and Z_p are the transfer functions. F_m and F_v are the inner and outer compensators, respectively. $\hat{i}_{LO}$ is the estimated inductor current obtained by the LO given in Eq. (3.1).

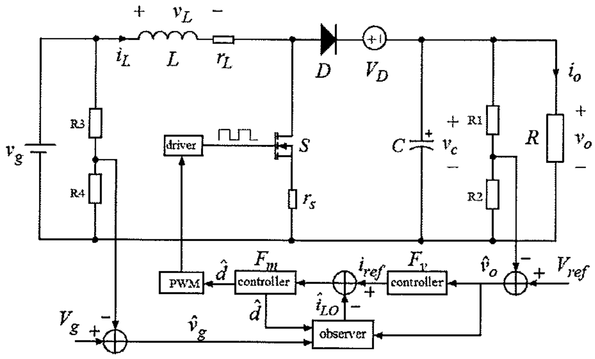

Fig. 3.2 LO-based sensorless multi-loop control for a boost converter.

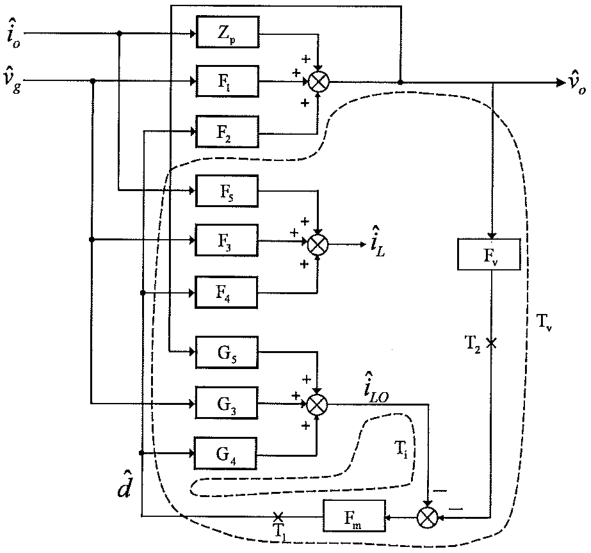

Fig. 3.3 Small signal block diagram of sensorless multi-loop control.

$$\begin{aligned}\dot{\hat{x}} &= A(\hat{x}) + B(\hat{x},u) + L(y-\hat{y}) \\ \hat{y} &= C\hat{x}(t)\end{aligned} \tag{3.1}$$

where $\hat{x} = [\hat{i}_{LO} \quad \hat{v}_{LO}]$ is the estimated system state, $\hat{y}$ is the estimated system output, and $y = \hat{v}_o$ is the measurable output. The matrices A, B and C come from the model of the converter, and L is the parameter of the LO. After Laplace transformation of Eq. (3.1), the transfer functions G_3, G_4, and G_5 can be obtained.

3.2.2 Closed-loop stability evaluation

Denote the current loop gain $T_i = F_m G_4$, and the voltage loop gain $T_v = F_m F_v F_2 + F_m G_5 F_2$. The total gain at the point T_1 and the outer gain at the point T_2 in Fig. 3.3 are written in Eqs. (3.2) and Eq. (3.3), respectively.

$$T_1 = F_m G_4 + F_m F_v F_2 + F_m G_5 F_2 \tag{3.2}$$

$$T_2 = \frac{F_m F_v F_2 + F_m G_5 F_2}{1 + F_m G_4} \tag{3.3}$$

From Eqs. (3.2) and (3.3), the crossover frequency of the current loop T_i should be as high as possible to provide a critical 90^0 phase boost for the outer loop T_v, while its loop gain should be as small as possible at low frequencies. The loop gain T_v should be as large as possible to attenuate the disturbance on the output voltage. The closed-loop stability can be examined through evaluating the loop gains at the points T_1 and T_2.

3.2.3 Closed-loop dynamic characteristics evaluation

The dynamic performance of a switching converter can be evaluated by the closed-loop characteristics including audio susceptibility and output impedance. From Fig. 3.3, the closed-loop audio susceptibility and output impedance of the output voltage are written in Eqs. (3.4) and (3.5), respectively.

$$\frac{\hat{v}_o(s)}{\hat{v}_g(s)} = \frac{F_1 + F_m(F_1 G_4 - F_2 G_3)}{1 + F_m G_4 + F_m F_v F_2 + F_m G_5 F_2} \tag{3.4}$$

$$\frac{\hat{v}_o(s)}{\hat{i}_o(s)} = \frac{Z_p + F_m Z_p G_4}{1 + F_m G_4 + F_m F_v F_2 + F_m G_5 F_2} \tag{3.5}$$

The dynamic performance of the inductor current $\hat{i}_L$ can also be evaluated by the following closed-loop inductor characteristics:

$$\frac{\hat{i}_L(s)}{\hat{v}_g(s)}=\frac{F_3(1+F_mG_4)+F_m(F_2F_3-F_1F_4)(F_v+G_5)-F_mF_4G_3}{1+F_mG_4+F_mF_vF_2+F_mG_5F_2} \tag{3.6}$$

$$\frac{\hat{i}_L(s)}{\hat{i}_o(s)}=\frac{F_5(1+F_mG_4)+F_m(F_2F_5-F_4Z_p)(F_v+G_5)}{1+F_mG_4+F_mF_vF_2+F_mG_5F_2} \tag{3.7}$$

The dynamic performance of the estimated inductor current $\hat{i}_{LO}$ can also be evaluated by the following closed-loop inductor characteristics:

$$\frac{\hat{i}_{LO}(s)}{\hat{v}_g(s)}=\frac{G_3+F_mF_v(F_2G_3-F_1G_4)+F_1G_5}{1+F_mG_4+F_mF_vF_2+F_mG_5F_2} \tag{3.8}$$

$$\frac{\hat{i}_{LO}(s)}{\hat{i}_o(s)}=\frac{-F_mF_vG_4Z_p+Z_pG_5}{1+F_mG_4+F_mF_vF_2+F_mG_5F_2} \tag{3.9}$$

3.3 Design of the LO-Based Sensorless Multi-loop Control for Boost Converters

3.3.1 Construction of the small signal average value model

The boost converter used in this research is shown in Fig. 3.2, in which several parasitic components are considered. Referring to [45], the small signal average value model of the boost converter in CCM is written in Eq. (3.10).

$$\dot{x}=Ax+B\hat{d}+Ew \tag{3.10}$$

where $x=[\hat{i}_L \quad \hat{v}_c]$, $w=[\hat{v}_g \quad \hat{i}_o]$, and

$$A=\begin{bmatrix} -\frac{r_L+Dr_s}{L} & -\frac{D'}{L} \\ \frac{D'}{C} & -\frac{1}{RC} \end{bmatrix},\quad B=\begin{bmatrix} \frac{(D'R-r_s)V_g+(r_s+r_L)V_D}{L(r_L+Dr_s+D'^2R)} \\ -\frac{V_g-D'V_D}{C(r_L+Dr_s+D'^2R)} \end{bmatrix},\quad E=\begin{bmatrix} \frac{1}{L} & 0 \\ 0 & -\frac{1}{C} \end{bmatrix}$$

$$D'=\frac{r_sV_{ref}+RV_g}{2R(V_{ref}+V_D)}\left(1+\sqrt{1-\frac{4R(r_L+r_s)(V_{ref}+V_D)V_{ref}}{(r_sV_{ref}+RV_g)^2}}\right) \tag{3.11}$$

The symbols $\hat{i}_L$, $\hat{v}_c$, $\hat{v}_g$, $\hat{i}_o$, and $\hat{d}$ are the small signals, and $\hat{v}_g$ and $\hat{i}_o$ are the disturbances. The symbol D denotes the duty ratio at a given operating point and $D' = 1 - D$, and $\hat{d}$ is the duty ratio adjustment from the given operation point. Ignoring the equivalent series resistance of the output capacitor, $\hat{v}_c$ is equivalent to $\hat{v}_o$. For convenience, define

$$A = \begin{bmatrix} a_{11} & a_{12} \\ a_{21} & a_{22} \end{bmatrix}, \quad B = \begin{bmatrix} b_1 \\ b_2 \end{bmatrix}, \quad E = \begin{bmatrix} e_1 & 0 \\ 0 & e_2 \end{bmatrix}$$

3.3.2 Derivation of the transfer functions

Through Laplace transformation of Eq. (3.10), the transfer functions shown in Fig. 3.3 are obtained as follows:

$$F_1 = \frac{a_{21}e_1}{\Delta} \tag{3.12}$$

$$F_2 = \frac{b_2 s + a_{21}b_1 - a_{11}b_2}{\Delta} \tag{3.13}$$

$$F_3 = \frac{e_1 s - e_1 a_{22}}{\Delta} \tag{3.14}$$

$$F_4 = \frac{b_1 s + a_{12}b_2 - a_{22}b_1}{\Delta} \tag{3.15}$$

$$F_5 = \frac{a_{12}e_2}{\Delta} \tag{3.16}$$

$$Z_p = \frac{e_2 s - a_{11}e_2}{\Delta} \tag{3.17}$$

where $\Delta = s^2 - (a_{11} + a_{22})s + a_{11}a_{22} - a_{12}a_{21}$. Substituting the matrices A, B, and C in Eq. (3.10) into Eq. (3.1) and performing Laplace transformation, the transfer functions G_3, G_4, and G_5 in Fig. 3.3 are obtained as follows:

$$G_3 = \frac{e_1 s + e_2(a_{12} - l_1) - e_1(a_{22} - l_2)}{\Lambda} \tag{3.18}$$

$$G_4 = \frac{b_1 s + b_2(a_{12} - l_1) - b_1(a_{22} - l_2)}{\Lambda} \tag{3.19}$$

$$G_5 = \frac{l_1 s + l_2 a_{12} - l_1 a_{22}}{\Lambda} \tag{3.20}$$

where $\Lambda = s^2 - (a_{11} + a_{22} - l_2)s + a_{11}a_{22} - a_{12}a_{21} - a_{11}l_2 + a_{21}l_1$, and l_1 and l_2 are the elements of the L. The PI controllers in Eqs. (3.21) and (3.22) are used as the compensators F_m and F_v in Fig. 3.3, respectively:

$$F_m = K_{Pm} + K_{Im}\frac{1}{s} \tag{3.21}$$

$$F_v = K_{Pv} + K_{Iv}\frac{1}{s} \tag{3.22}$$

Let $C = [0 \quad 1]$. The LO in Eq. (3.1) is written in Eq. (3.23).

$$\dot{\hat{x}} = \begin{bmatrix} a_{11} & a_{12} \\ a_{21} & a_{22} \end{bmatrix}\hat{x} + \begin{bmatrix} b_1 & e_1 \\ b_2 & 0 \end{bmatrix}u + \begin{bmatrix} l_1 \\ l_2 \end{bmatrix}(v_o - \hat{v}_o) \tag{3.23}$$

where $\hat{x} = [\hat{\imath}_{LO} \quad \hat{v}_{LO}]$ is the estimated system state, and $u = [\hat{d} \quad \hat{v}_g]$ is the system input. The compensators in Eqs. (3.21) and (3.22) as well as the LO in Eq. (3.23) can be designed by the closed-loop stability evaluations in Eqs. (3.2) and (3.3), and the closed-loop characteristics evaluations in Eqs. (3.4), (3.5), (3.6), (3.7), (3.8) and (3.9).

3.4 Simulations and Experiments

A boost converter with parameters listed in Table 2.1 is used to show the design of LO based sensoreless multi-loop control.

3.4.1 Simulations of the closed-loop stability and characteristics

Substituting the parameters in Table 2.1 into Eq. (3.10), the matrices A, B and E is obtained as follows:

$$A = \begin{bmatrix} -918.8 & -9938.5 \\ 467.1 & -40 \end{bmatrix}, \quad B = \begin{bmatrix} 450820 \\ -1712.7 \end{bmatrix}, \quad E = \begin{bmatrix} 21277 & 0 \\ 0 & -1000 \end{bmatrix}$$

Denote the current loop $T_i = F_mG_4$ and the voltage loop $T_v = F_mF_vF_2 + F_mG_5F_2$ in Fig. 3.3. The overall loop gain at the point T_1 is written as $T_1 = T_i + T_v$, and the outer loop gain at the point T_2 is written as $T_2 = T_v/1+T_i$. From the expressions of T_1 and T_2, the crossover frequency of the current loop T_i should be as high as possible to provide a 90^0 phase boost for the voltage loop T_v, while its gain should be as small as possible at low frequencies; the loop gain T_v should be as large as possible to attenuate the disturbance on the output voltage.

For this boost converter with parameters listed in Table 2.1, the LO in Eq. (3.1) is written as follows:

$$\overset{\bullet}{\hat{x}} = \begin{bmatrix} -918.8 & -9938.5 \\ 467 & -40 \end{bmatrix} \hat{x} + \begin{bmatrix} 450820 & 21277 \\ -1712.7 & 0 \end{bmatrix} u + \begin{bmatrix} l_1 \\ l_2 \end{bmatrix} \Delta\hat{v}_o \tag{3.24}$$

where $\hat{x} = [\hat{i}_{LO} \quad \hat{v}_{LO}]$, $u = [\hat{d} \quad \hat{v}_g]$, and $\Delta\hat{v}_o = \hat{v}_o - \hat{v}_{LO}$. The PI controllers in Eqs. (3.21) and (3.22) are used as the compensators F_m and F_v.

In Eqs. (3.24), (3.21), and (3.22), the parameters to be determined are $L = [l_1 \quad l_2]^T$, K_{P1}, K_{I1}, K_{P2}, and K_{I2}. An iterative try-and-error design process is: assign the eigenvalues of $A-LC$ to determine $L = [l_1 \quad l_2]^T$, here $C = [0 \quad 1]$; tune K_{P1}, K_{I1}, K_{P2}, and K_{I2} through examining the bode plots of the loop gains $T_1 = T_i + T_v$ and $T_2 = T_v/1+T_i$ until a stable control system is maintained; further tune K_{P1}, K_{I1}, K_{P2}, and K_{I2} through examining the closed-loop characteristics in Eqs. (3.2) and (3.3) to obtain a good dynamic performance; repeat the above steps until the desired dynamic performance is obtained. Through the above iterative process, it is found that the eigenvalues $\{-0.0093, -7.5003\}\times10^5$ are the best, and correspondingly $L = [0.01 \quad 0.75]^T\times10^6$. After the LO is determined, the following compensators F_m and F_v are used to show the design of the compensators F_m and F_v:

$$\begin{aligned} &I. \ \ F_m = 0.20 + 250/s, \ F_v = 30.0 + 18000/s \\ &II. \ \ F_m = 0.40 + 500/s, \ F_v = 30.0 + 18000/s \\ &III. \ F_m = 0.20 + 250/s, \ F_v = 45.0 + 25000/s \end{aligned} \tag{3.25}$$

The bode plots of the loop gains T_1 and T_2 are shown in Fig. 3.4, with the stability characteristics given in Eq. (3.26).

$$\begin{aligned} &I. \ \ T_1 : f_c = 12.9kHz, PM = 78.8^o \\ &\quad\ \ T_2 : f_c = 2.26kHz, PM = 73.5^o, GM = 18.8dB \\ &II. \ \ T_1 : f_c = 25.6kHz, PM = 84.3^o \\ &\quad\ \ T_2 : f_c = 2.28kHz, PM = 77.9^o, GM = 18.8dB \\ &III. \ T_1 : f_c = 12.5kHz, PM = 72.0^o \\ &\quad\ \ T_2 : f_c = 3.33kHz, PM = 66.4^o, GM = 15.3dB \end{aligned} \tag{3.26}$$

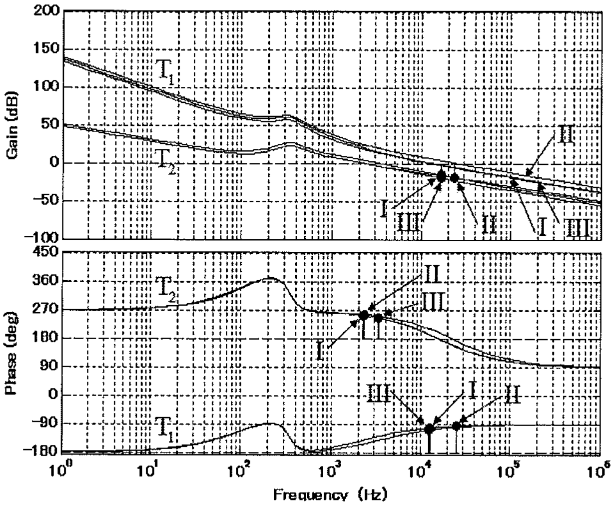

Fig. 3.4 Bode plots of T_1 and T_2.

The closed-loop characteristics of output voltage in Eqs. (3.4) and (3.5) are shown in Fig. 3.5, and the step responses of the output voltage to step changes in the input voltage and the load current are shown in Fig. 3.6. From the curves I and II in Figs. 3.4, 3.5, and 3.6, it can be seen that increasing the gain of inner compensator F_m can increase the gain crossover frequency, and decrease the peak output voltage, however, the recovery time is prolonged; from the curves I and III, it can be seen that increasing the gain of the outer compensator F_v can improve the dynamic performance, however, the phase margins are reduced. The curves I, II, and III demonstrate that I in Eq. (3.25) is the best.

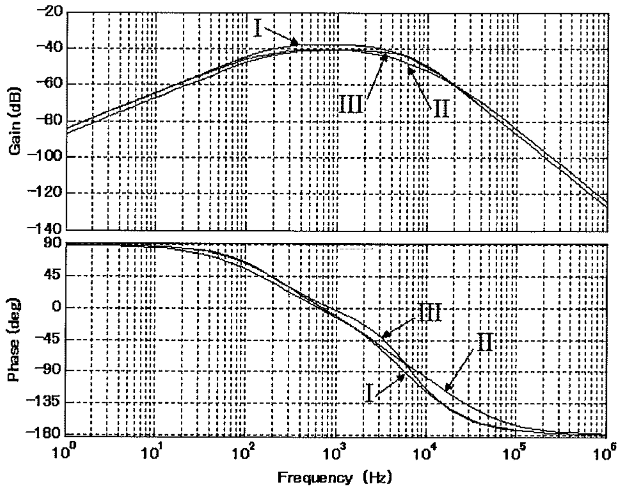

(a) audio susceptibility

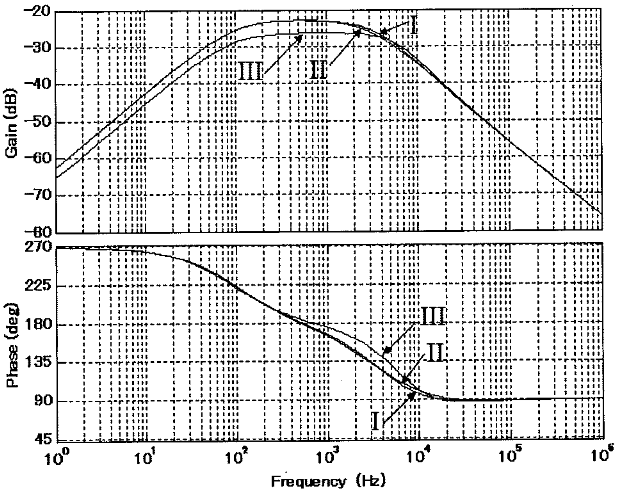

(b) output impedance

Fig. 3.5 Closed-loop dynamic characteristics (output voltage).

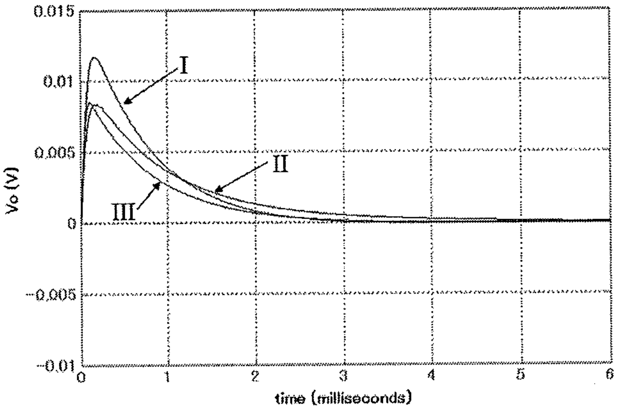

(a) step response of $\hat{v}_o$ to a step change in $\hat{v}_g$

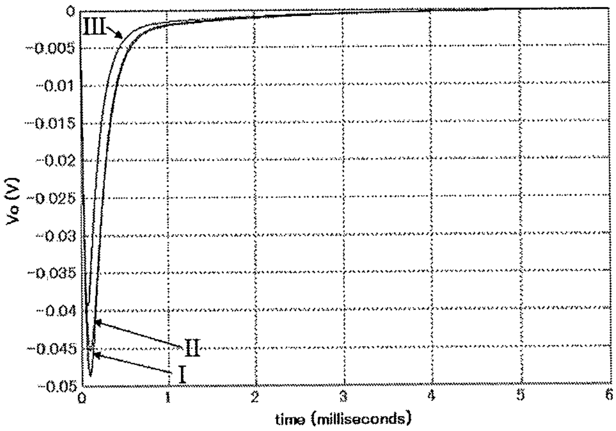

(b) step response of $\hat{v}_o$ to a step change in $\hat{i}_o$

Fig. 3.6 Step responses of $\hat{v}_o$ to step changes in $\hat{v}_g$ and $\hat{i}_o$.

The closed-loop dynamic characteristics of the inductor current $\hat{\imath}_L$ and the estimated inductor current $\hat{\imath}_{LO}$ given in Eqs. (3.6), (3.7), (3.8) and (3.9) are shown in Fig. 3.7 for the compensators I in Eq. (3.25), it can be seen that the curves are almost the same. The step responses of $\hat{\imath}_L$ and $\hat{\imath}_{LO}$ are shown in Fig. 3.8. It can be seen that the estimated inductor current $\hat{\imath}_{LO}$ perfectly estimated the inductor current $\hat{\imath}_L$ when the input voltage is disturbed, while there is a slight error between $\hat{\imath}_L$ and $\hat{\imath}_{LO}$ when the load current is disturbed.

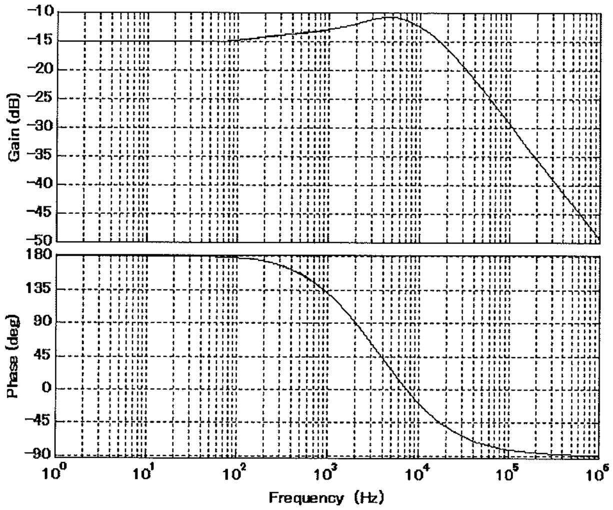

(a) audio susceptibility ($\hat{\imath}_L/\hat{v}_g$ and $\hat{\imath}_{LO}/\hat{v}_g$)

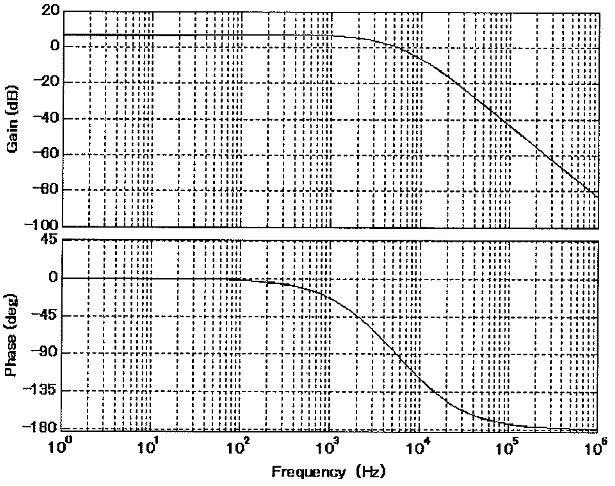

(b) output impedance ($\hat{\imath}_L/\hat{\imath}_o$ and $\hat{\imath}_{LO}/\hat{\imath}_o$)

Fig. 3.7 Closed-loop dynamic characteristics of $\hat{\imath}_L$ and $\hat{\imath}_{LO}$.

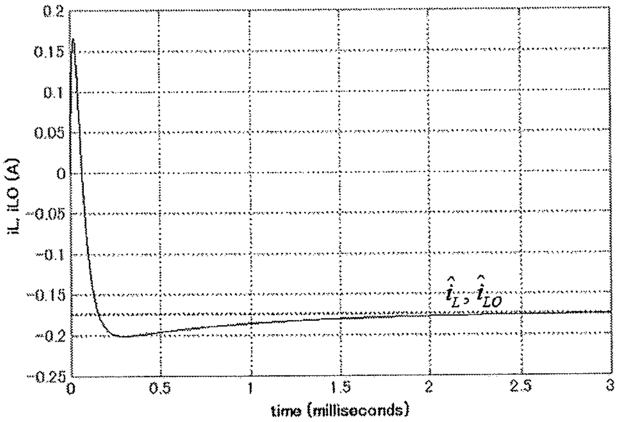

(a) step responses of of $\hat{\imath}_L$ and $\hat{\imath}_{LO}$ to a step change in $\hat{v}_g$

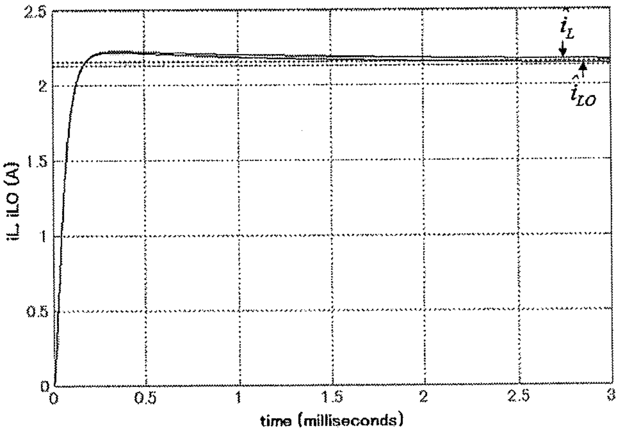

(b) step responses of of $\hat{\imath}_L$ and $\hat{\imath}_{LO}$ to a step change in $\hat{\imath}_o$

Fig. 3.8 Step responses of $\hat{\imath}_L$ and $\hat{\imath}_{LO}$ to step changes in $\hat{v}_g$ and $\hat{\imath}_o$.

3.4.2 Practical experiments

To execute the controller on a digital processor, the above continuous compensators and LO should be discretized. The discrete counterpart of Eq. (3.24) is obtained in Eq. (3.27) by the zero-hold discretization method. The discrete counterparts of Eqs. (3.21) and (3.22) are obtained in Eqs. (3.28) and (3.29) by the backward difference $s = 1\text{-}z^{-1}/T_s$, where T_s is the switching period.

$$\hat{x}(k+1)=\begin{bmatrix}0.9938 & -0.0660\\ 0.0031 & -0.9996\end{bmatrix}\hat{x}(k)+\begin{bmatrix}2.9965 & 0.1414\\ -0.0067 & 0.0002\end{bmatrix}u(k)+\begin{bmatrix}-0.0988\\ 4.9993\end{bmatrix}\Delta\hat{v}_o(k) \quad (3.27)$$

where $\hat{x}(k) = [\hat{\imath}_{LO}(k) \quad \hat{v}_{LO}(k)]$, $u(k) = [\hat{d}(k) \quad \hat{v}_g(k)]$, and $\Delta\hat{v}_o(k) = \hat{v}_o(k) - \hat{v}_{LO}(k)$.

$$F_m = 0.2 + 0.0017(1 - z^{-1}) \tag{3.28}$$

$$F_v = 30 + 0.1200(1 - z^{-1}) \tag{3.29}$$

The practical dynamic responses are shown in Fig. 3.9.

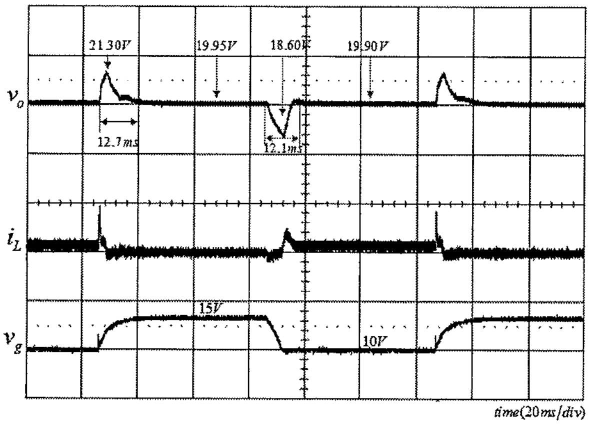

(a) Dynamic response when input voltage is disturbed

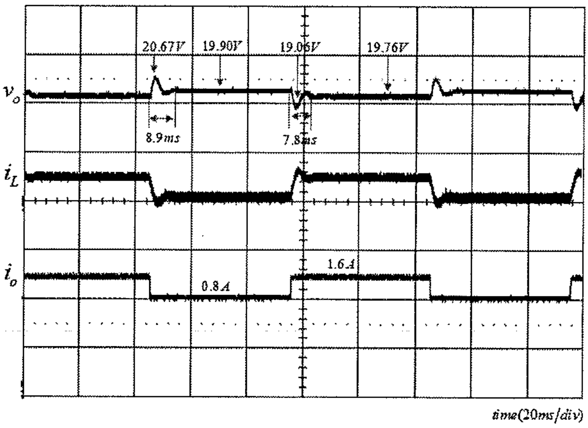

(b) Dynamic response when load current is disturbed

Fig. 3.9 Practical dynamic responses of output voltage and inductor current.

The practical experimental environment is shown in Fig. 3.10. A digital 16 bit DSC NJU20010 produced by the NJRC is used to execute the above digital controllers. The clock frequency of DSC is 62.5 MHz. An ADC and a PWM are integrated into the DSC. The limit of duty ratio is set to 0.05~0.88. The slew rates of the load and input voltage are 250mA/μs and 2.0V/μs, respectively. A resistor 25 Ω is used as the normal load. An electronic load PLZ164W is used to generate the load current disturbance 0.8 A. The input voltage is alternated by a switch.

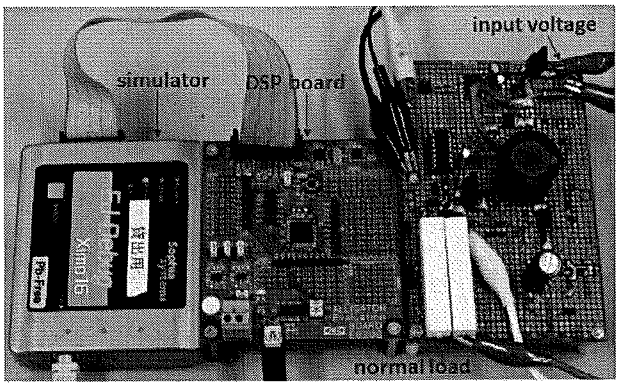

Fig. 3.10 Experimental environment.

3.5 Conclusions

The design of a LO based sensorless multi-loop control for a boost converter is proposed. The examinations of the closed-loop stability, the closed-loop dynamic characteristics of the output voltage, the inductor current as well as the estimated inductor current are provided. Simulations show the design procedure of determining the controllers and the LO. Practical experiments give the practical dynamic responses. The LO is effective in estimating the inductor current for the sensorless multi-loop control, and the proposed closed-loop stability and characteristics evaluation method is feasible to design the LO-based sensorless multi-loop control for boost converters.

4

Robust H∞ Control of Boost Converters: Current Sensorless Control

It is difficult to design the LO-based sensorless control of boost converters, because there are too many parameters to be determined in the control loops, moreover, the relationships between the loop gains and the closed-loop characteristics are generally indirect for the multi-loop control. In this chapter, two novel robust H∞ synthesis approaches are proposed to design compact sensorless controllers for boost converters, which need not solve any algebraic Riccati equation or linear matrix inequalities, and most importantly, parameterizes the controllers by an adjustable parameter behaving like a 'knob' on the dynamic performance, so that the closed-loop characteristics evaluation is very straightforward.

Part I

A Full-Order Sensorless Controller

4.1 Introduction

The design of an LO-based sensorless multi-loop control for boost converters in chapter 3 is based on the classical control theory: the control part is separated into two loops including an outer loop and an inner, and the closed-loop characteristics is examined in the frequency domain. A trial-and-error design procedure is needed since the controllers and the state observer have to be designed separately, and the closed-loop characteristics evaluation is severely aggravated. The trial-and-error design process is as follows: select the parameters of LO; design the compensators; evaluate the closed-loop stability through; evaluate the closed-loop dynamic characteristics; repeat the above process until the desired dynamic performance is maintained. It can be seen that it is complicated to design a sensorless multi-loop control in the frequency domain using the classical control theory.

Modern control no longer separates the control into two loops, and directly handles the system states including inductor current and the capacitor voltage of a converter in a state feedback controller. However, a state feedback controller with a state observer as presented in [43] brings no more benefits to the closed-loop characteristics evaluation than the conventional sensorless multi-loop control. Robust H∞ control, as a modern control, provides a synthesis approach to directly taking the disturbance attenuation as the design target. The robust H∞ control of switching converters has been introduced in several papers [46] [47] [48], however, there are some common drawbacks: one drawback is that an iterative procedure is needed to solve the algebraic Riccati equations (ARE) [46] [47] or linear matrix inequalities (LMI) [48]; as the main drawback, the advantages of the robust H∞ control over the conventional multi-loop control cannot be verified through closed-loop characteristics evaluation. In addition, there has no paper introducing the design of sensorless control for boost converters by the robust H∞ control. Therefore, in this chapter, a novel H∞ synthesis approach is firstly proposed to design a sensorless controller for boost converters.

The block diagram of robust H∞ control of a switching converter is shown in Fig. 4.1. The disturbance from the input voltage or the load is $w \in R^l$, the controlled output is $z \in R^q$, the control input is $u \in R^m$, and the measured output is $y \in R^p$. For boost converters, since the stability of the inductor current which is an internal state should also be guaranteed, it is necessary to include both the output voltage and the inductor current in the controlled output *z*. However, the disturbance attenuation on the output voltage is more desired. For this purpose, a weighting matrix *W* can be used as shown in Fig. 4.1.

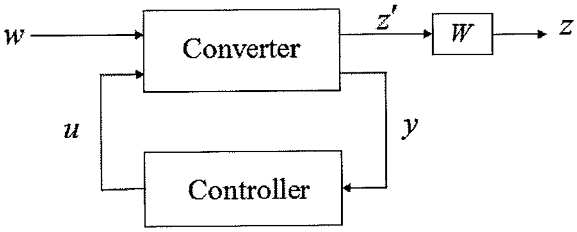

Fig. 4.1 Block diagram of robust H∞ control.

Define the state space equation of the converter as:

$$Converter:\begin{cases}\overset{\bullet}{x}=Ax+Bu+Ew\\ y=C_1x+D_1w\\ z=C_2x+D_2u\end{cases}\tag{4.1}$$

where $x\in R^n$ is the system states such as the inductor current and capacitor voltage, *u*, *w*, *y* and *z* are the same as shown in Fig. 4.1. Matrices *A*, *B* and *E* come from the equations of the converter, while matrices C_1, D_1, C_2 and D_2 are determined by the controller to be designed.

For the system in Eq. (4.1), a sensorless controller, also called measurement feedback controller, is written as follows:

$$Controller:\begin{cases}\overset{\bullet}{p}=Kp+Ly\\ u=Mp+Ny\end{cases}\tag{4.2}$$

where *y* is the input and *u* is the output of the controller as shown in Fig. 4.1, while *p* is the estimated state. Matrices *K*, *L*, *M* and *N* are the parameters of the controller.

Mainly, there are two H∞ synthesis approaches to derive a solution to Eq. (4.2). One approach need solve the AREs as introduced in [46] [47]. The other approach need solve the LMIs as introduced in [48]. There are some common drawbacks of the above H∞ synthesis approaches. One drawback is that, a suitable disturbance attenuation level should be first found, and an iterative procedure is needed to solve the AREs or LMIs. The second drawback is that it is difficult to check the solvability conditions. Moreover, as the main drawback, it is difficult to show how the closed-loop characteristics vary in a certain controller set, so that the advantages of the robust H∞ control over the conventional multi-loop control cannot be easily verified. In this chapter, a novel robust H∞ synthesis approach, which need not solve any ARE or LMI, and most importantly, parameterize the controller by an adjustable parameter behaving like a 'knob' on the dynamic performance, is proposed to design a compact sensorless controller for boost converters [49].

4.2 Introduction of the Proposed Robust H∞ Synthesis Approach

The closed-loop transfer function $G_{cl}(s)$ of the system in Eq. (4.1) with the controller in Eq. (4.2), that is from the disturbance w to the controlled output z is written as

$$G_{cl}(s) = C_{cl}(sI - A_{cl})^{-1} B_{cl} + D_{cl} \tag{4.3}$$

where

$$A_{cl} = \begin{bmatrix} A + BNC_1 & BM \\ LC_1 & K \end{bmatrix}, \quad B_{cl} = \begin{bmatrix} E + BND_1 \\ LD_1 \end{bmatrix}$$

$$C_{cl} = \begin{bmatrix} C_2 + D_2NC_1 & D_2M \end{bmatrix}, \quad D_{cl} = D_2ND_1$$

The H∞ norm of $G_{cl}(s)$ is defined in Eq. (4.4). The essential of robust H∞ control is to minimize $G_{cl}(s)$ according to the H∞ standard as defined in Eq. (4.5).

$$\left\| G_{cl}(s)_{s=j\omega} \right\|_{\infty} := \sup_{\omega \in [0,\infty]} \sigma_{\max}[G_{cl}(j\omega)] \tag{4.4}$$

$$\begin{cases} \left\| G_{cl}(s) \right\|_{\infty} < \gamma \\ \textit{Condition: the control object is stabilized} \end{cases} \tag{4.5}$$

The basis of the proposed H∞ synthesis approach is to decompose the system in Eq. (4.1) into a special coordinate basis (SCB) [50] [51]. Through SCB, the solvability conditions of the system in Eq. (4.1) with the controller in Eq. (4.2) can be easily checked, meanwhile, a step-by-step design procedure can be obtained, as presented from the following.

4.2.1 Solvability conditions of the proposed H∞ approach

Let (A, B, C_2, D_2) and (A^T, C_1^T, E^T, D_1^T) denote the subsystems Σ_P and Σ_Q, respectively. The solvability conditions of the system in Eq. (4.1) with the controller in Eq. (4.2) are as follows:

I) (A, B) is stabilizable;

II) (A, C_1) is detectable;

III) Σ_P and Σ_Q has no invariant zero on imaginary axis;

IV) $\mathrm{Im}(E) \subset \mathcal{V}^{-}(\Sigma_P) + \mathcal{S}^{-}(\Sigma_P)$;

V) $\mathrm{Im}(C_2^T) \supset V^-(\Sigma_Q) + S^-(\Sigma_Q)$.

I and II are the necessary conditions, while III, IV, and V are the sufficient conditions.

4.2.2 Controller design procedure

Referring to [51] [52] [53], the design procedure of the controller in Eq. (4.2) for the system in Eq. (4.1) is as follows:

Step 1: Decompose the system in Eq. (4.1) into SCB and check the solvability conditions.

Step 2: Compute the H∞ infimum γ^* of the system in Eq. (4.1).

Step 3: Set any $\gamma > \gamma^*$, and design a full state feedback controller $u = F(\gamma, \varepsilon)x$ for the following system through SCB decomposition:

$$\begin{cases} \dot{x} = Ax + Bu + Ew \\ y = x \\ z = C_2 x + D_2 u \end{cases} \tag{4.6}$$

Step 4: Similarly, design a full state feedback controller $u = K(\gamma, \varepsilon)$x for the following system:

$$\begin{cases} \dot{x} = A^T x + C_1^T u + C_2^T w \\ y = x \\ z = E^T x + D_1^T u \end{cases} \tag{4.7}$$

Step 5: From the above obtained state feedback controllers, the controller in Eq. (4.2) is expressed as follows:

$$\begin{cases} \dot{p} = Kp + Ly \\ u = Mp + Ny \end{cases} \tag{4.8}$$

where

$$
\begin{aligned}
K = A+\gamma^{-2}EE^{T}P(\gamma)+BF(\gamma,\varepsilon)+\left[I-\gamma^{-2}Q(\gamma)P(\gamma)\right]^{-1}\Big\{K(\gamma,\varepsilon)\left[C_1+\gamma^{-2}D_1E^{T}P(\gamma)\right] \\
+\gamma^{-2}Q(\gamma)\left[A^{T}P(\gamma)+P(\gamma)A+C_2^{T}C_2+\gamma^{-2}P(\gamma)EE^{T}P(\gamma)\right] \\
+\gamma^{-2}Q(\gamma)\left[P(\gamma)B+C_2^{T}D_2\right]F(\gamma,\varepsilon)\Big\}
\end{aligned}
$$

$$
\begin{aligned}
L &= -\left[I-\gamma^{-2}Q(\gamma)P(\gamma)\right]^{-1}K(\gamma,\varepsilon) \\
M &= F(\gamma,\varepsilon) \\
N &= 0
\end{aligned}
$$

where γ represents the desired disturbance attenuation level and can be set to any value satisfying $\gamma > \gamma^*$; γ^* is the H∞ infimum of the system in Eq. (4.1) and can be computed as introduced in [54] [55]. The adjustable parameter is $\varepsilon > 0$. There exists an $\varepsilon^* > 0$ such that for all $0 < \varepsilon < \varepsilon^*$, the closed-loop system becomes internally stable and the γ-suboptimal $\|G_{cl}(s)\|_\infty < \gamma$ is satisfied.

4.3 Derivation of a Sensorless Controller for Boost Converters

4.3.1 Construction of the small signal average value model

The boost converter used in this research is shown in Fig. 4.2, in which several parasitic components are considered. Referring to [45], the small signal average value model of the boost converter in CCM is constructed in Eq. (4.9).

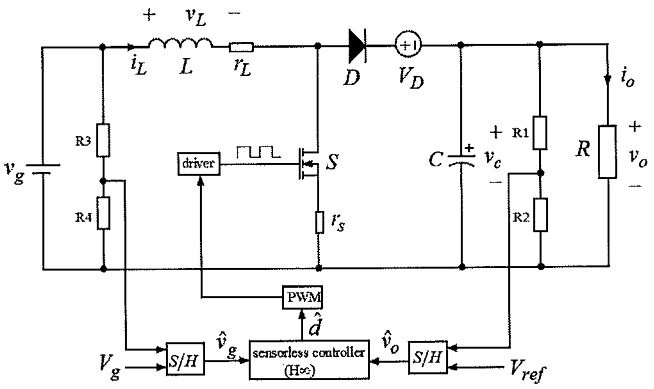

Fig. 4.2 Sensorless control of a boost converter.

$$\dot{x} = Ax + B\hat{d} + Ew \tag{4.9}$$

where $x = [\hat{i}_L \quad \hat{v}_c]$, $w = [\hat{v}_g \quad \hat{i}_o]$, and

$$A = \begin{bmatrix} -\frac{r_L + Dr_s}{L} & -\frac{D'}{L} \\ \frac{D'}{C} & -\frac{1}{RC} \end{bmatrix}, \quad B = \begin{bmatrix} \frac{(D'R - r_s)V_g + (r_s + r_L)V_D}{L(r_L + Dr_s + D'^2 R)} \\ -\frac{V_g - D'V_D}{C(r_L + Dr_s + D'^2 R)} \end{bmatrix}, \quad E = \begin{bmatrix} \frac{1}{L} & 0 \\ 0 & -\frac{1}{C} \end{bmatrix}$$

and

$$D' = \frac{r_s V_{ref} + RV_g}{2R(V_{ref} + V_D)}\left(1 + \sqrt{1 - \frac{4R(r_L + r_s)(V_{ref} + V_D)V_{ref}}{(r_s V_{ref} + RV_g)^2}}\right) \tag{4.10}$$

The symbol D denotes the duty ratio at a given operating point and $D' = 1 - D$, and $\hat{d}$ represents the duty ratio adjustment from the given operation point when a disturbance appears, that is the small signal of the duty ratio D. The symbols $\hat{x} = [\hat{i}_L \quad \hat{v}_c]^T$ and $\hat{w} = [\hat{v}_g \quad \hat{i}_o]^T$ are the corresponding AC small signals. Ignoring the equivalent series resistance of the output capacitor, $\hat{v}_c$ is equivalent to $\hat{v}_o$. Here, $\hat{v}_o$ and $\hat{v}_g$ are not scaled by the corresponding dividing resistors shown in Fig. 4.2 to evaluate the practical closed-loop characteristics. The coefficients of a controller will be scaled at the execution stage on a digital processor. For convenience, define

$$A = \begin{bmatrix} a_{11} & a_{12} \\ a_{21} & a_{22} \end{bmatrix}, \quad B = \begin{bmatrix} b_1 \\ b_2 \end{bmatrix}, \quad E = \begin{bmatrix} e_1 & 0 \\ 0 & e_2 \end{bmatrix}$$

4.3.2 Construction of the state space equation for the proposed robust H∞ approach

From the AC small signal model in Eq. (4.9), the state space equation for the proposed robust H∞ control is written as follows:

$$\begin{cases} \dot{\hat{x}} = A\hat{x} + B\hat{d} + E\hat{w} \\ y = C_1\hat{x} + D_1\hat{w} \\ z = C_2\hat{x} + D_2\hat{d} \end{cases} \tag{4.11}$$

The matrices A, B and E are the same as in Eq. (4.9), and

$$C_1 = \begin{bmatrix} 0 & 0 \\ 0 & 1 \end{bmatrix},\ D_1 = \begin{bmatrix} 1 & 0 \\ 0 & 0 \end{bmatrix},\ C_2 = \begin{bmatrix} 1 & 0 \\ 0 & w_o \end{bmatrix},\ D_2 = \begin{bmatrix} 0 \\ 0 \end{bmatrix}$$

The measurable output y is $[\hat{v}_g \quad \hat{v}_o]^T$, and the controlled output z is $[\hat{i}_L \quad \hat{v}_o]^T$. The weight on the output voltage is w_o.

4.3.3 SCB decomposition of the system in Eq. (4.11)

The SCB decomposition of the subsystem $\Sigma_P := (A, B, C_2, D_2)$ is obtained as:

$$\begin{gathered} \begin{bmatrix} \dot{x}_b \\ \dot{x}_d \end{bmatrix} = \begin{bmatrix} a_{22} - \dfrac{b_2}{b_1} a_{12} & w_o\left(a_{21} - \dfrac{b_2}{b_1}(a_{11} - a_{22}) - \dfrac{b_2^2}{b_1^2} a_{12}\right) \\ a_{11} + \dfrac{b_2}{b_1} a_{12} & \dfrac{a_{12}}{w_o} \end{bmatrix} \begin{bmatrix} x_b \\ x_d \end{bmatrix} + \begin{bmatrix} 0 \\ b_1 \end{bmatrix} \hat{d} \\ \begin{bmatrix} y_d \\ y_b \end{bmatrix} = \begin{bmatrix} x_d \\ x_b \end{bmatrix} \end{gathered} \tag{4.12}$$

and

$$\Gamma_{sP} = \begin{bmatrix} 0 & 1 \\ \dfrac{1}{w_o} & \dfrac{b_2}{b_1} \end{bmatrix},\ \Gamma_{oP} = \begin{bmatrix} 1 & 0 \\ w_o \dfrac{b_2}{b_1} & 1 \end{bmatrix},\ \Gamma_{iP} = \frac{1}{b_1}$$

where Γ_{sP}, Γ_{oP}, and Γ_{iP} are the state, output and input transformation matrices, respectively. The states and outputs after SCB decomposition of the subsystem Σ_P are x_b, x_d and y_b, y_d, respectively. The state x_b will not be directly influenced by the input $\hat{d}$, however, will be indirectly controlled by the output y_d. The state x_d is associated with the input $\hat{d}$ and the output y_d. This SCB implies a controllable and observable subsystem.

The SCB decomposition of the subsystem $\Sigma_Q := (A^T, C_1^T, E^T, D_1^T)$ is obtained as

$$\begin{aligned} \begin{bmatrix} \dot{x}_a^- \\ \dot{x}_d \end{bmatrix} &= \begin{bmatrix} a_{11} & a_{21} \\ a_{12} & a_{22} \end{bmatrix} \begin{bmatrix} x_a^- \\ x_d \end{bmatrix} + \begin{bmatrix} 0 & 0 \\ 0 & 1 \end{bmatrix} \begin{bmatrix} u_0 \\ u_d \end{bmatrix} \\ \begin{bmatrix} y_0 \\ y_d \end{bmatrix} &= \begin{bmatrix} e_1 & 0 \\ 0 & 1 \end{bmatrix} \begin{bmatrix} x_a^- \\ x_d \end{bmatrix} + \begin{bmatrix} 1 & 0 \\ 0 & 0 \end{bmatrix} \begin{bmatrix} u_0 \\ u_d \end{bmatrix} \end{aligned} \tag{4.12}$$

and

$$\Gamma_{sQ} = \begin{bmatrix} 1 & 0 \\ 0 & 1 \end{bmatrix}, \quad \Gamma_{oQ} = \begin{bmatrix} 1 & 0 \\ 0 & e_2 \end{bmatrix}, \quad \Gamma_{iQ} = \begin{bmatrix} 1 & 0 \\ 0 & 1 \end{bmatrix}$$

where Γ_{sQ}, Γ_{oQ}, and Γ_{iQ} are the state, output and input transformation matrices, respectively. The states and outputs after SCB decomposition of the subsystem Σ_Q are x_a^-, x_d and y_o, y_d, respectively. The state x_a^- is stable and will not be directly controlled by the virtual inputs u_o, u_d and the outputs y_o, y_d. The state x_d is associated with the virtual inputs u_o, u_d and the output y_d. This SCB implies a controllable and observable subsystem.

4.3.4 Solvability Verification

It is easy to prove that the solvability conditions I, II and III in subsection 4.2.1 are satisfied. The following can be obtained after SCB decomposition:

$$\mathcal{V}^-(\Sigma_Q) = \mathrm{Im}\{\begin{bmatrix} 1 \\ 0 \end{bmatrix}\}, \quad \mathcal{S}^-(\Sigma_Q) = \mathrm{Im}\{\begin{bmatrix} 0 \\ 1 \end{bmatrix}\}$$

Obviously, $\mathrm{Im}(C_2^T) \subset R^2$, so the solvability condition V is also satisfied. Although the SCB decomposition of the subsystem Σ_P shows that there is a state x_b, so that the condition IV is not satisfied, it does not mean that the controller in Eq. (4.2) for the system in Eq. (4.11) is not solvable. It is still solvable, however, a complicated computation of the H∞ infimum γ^* is required as presented from the following.

4.3.5 Computation of the H∞ infimum of the system in Eq. (4.11)

Through SCB decomposition, it is found that the H∞ infimum of the subsystem Σ_Q is $\gamma_Q^* = 0$. Thus, the H∞ infimum of the system in Eq. (4.11) is determined only by the subsystem Σ_P.

Referring to [55], for a given γ > 0, there exists a full information feedback controller for the subsystem Σ_P and the closed-loop satisfies $\|G_{cl}(s)\|_\infty < \gamma$, if only if there exists a positive real symmetric solution S_x to the following algebraic Riccati equation:

$$s_x A_x + A_x^T s_x + s_x E_x E_x^T s_x \gamma^{-2} - s_x B_x B_x^T s_x + C_x^T C_x = 0 \tag{4.14}$$

where

$$A_x = a_{22} - \frac{b_2}{b_1} a_{12} - \frac{w_o^2 b_1 b_2}{b_1^2 + w_o^2 b_2^2}\left(a_{21} - \frac{b_2}{b_1}(a_{11} - a_{22}) - \frac{b_2^2}{b_1^2} a_{12}\right)$$

$$B_x B_x^T = \frac{w_o^2 b_1^2}{b_1^2 + w_o^2 b_2^2}\left(a_{21} - \frac{b_2}{b_1}(a_{11} - a_{22}) - \frac{b_2^2}{b_1^2} a_{12}\right)^2$$

$$C_x^T C_x = \frac{b_1^2}{b_1^2 + w_o^2 b_2^2}$$

$$E_x E_x^T = w_o^2\left(\frac{b_2^2}{b_1^2} e_1^2 + e_2^2\right)$$

According to the above state feedback controller existing condition, the H∞ infimum of Eq. (4.11) is obtained as:

$$\gamma^* = \frac{\sqrt{(b_1^2 e_2^2 + b_2^2 e_1^2)(b_1^2 + w_o^2 b_2^2)}}{b_1^2 a_{21} - b_1 b_2 (a_{11} - a_{22}) - b_2^2 a_{12}} \tag{4.15}$$

4.3.6 Derivation of the controller in Eq. (4.2)

Following the design procedure described in the subsection 4.2.2, the controller in Eq. (4.2) is obtained as follows:

$$\begin{cases} \dot{p} = K_F p + L_F y \\ \hat{d} = M_F p + N_F y \end{cases} \tag{4.16}$$

where

$$
\begin{aligned}
K_F &= BF(\gamma,\varepsilon) + \begin{bmatrix} a_{11} & 0 \\ a_{21} - w_o^2 e_2^2 b_1^{-1} b_2 s_x \gamma^{-2} & w_o^2 e_2^2 s_x \gamma^{-2} \end{bmatrix} \\
L_F &= -K(\gamma,\varepsilon) \\
M_F &= F(\gamma,\varepsilon) \\
N_F &= 0
\end{aligned}
$$

and

$$
F(\gamma,\varepsilon) = \begin{bmatrix} -\dfrac{a_{11}}{b_1} - \dfrac{(\dfrac{a_{21}}{b_2} - \dfrac{a_{11}-a_{22}}{b_1} - \dfrac{a_{12}b_2}{b_1^2})s_x - \dfrac{b_1}{w_o^2 b_2^2}}{1+\dfrac{b_1^2}{w_o^2 b_2^2}} \dfrac{\lambda_1}{\varepsilon} \\[3ex] -\dfrac{a_{12}}{b_1} + \dfrac{(\dfrac{a_{21}b_1}{b_2^2} - \dfrac{a_{11}-a_{22}}{b_2} - \dfrac{a_{12}}{b_1})s_x + \dfrac{1}{b_2}}{1+\dfrac{b_1^2}{w_o^2 b_2^2}} \dfrac{\lambda_1}{\varepsilon} \end{bmatrix}^T
$$

$$
K(\gamma,\varepsilon) = \begin{bmatrix} -e_1 & 0 \\ -a_{12} & -a_{22} + \dfrac{\lambda_2}{\varepsilon} \end{bmatrix}^T
$$

The λ_1 and λ_2 in Eq. (4.16) can be set to any negative values, for example –1. The adjustable parameter is $\varepsilon > 0$. There exists an $\varepsilon^* > 0$ such that for all $0 < \varepsilon < \varepsilon^*$, the closed-loop system becomes internally stable and the γ-suboptimal $\|G_{cl}(s)\|_\infty < \gamma$ will be satisfied, where $\gamma > \gamma^*$.

4.4 Simulations and Experiments

To show the straightforward closed-loop characteristics evaluation of boost converters by the controller in Eq. (4.16), a boost converter listed in Table 2.1 is used.

4.4.1 Closed-loop characteristics evaluation

Substituting the parameters in Table 2.1 into Eq. (4.11), the matrices *A*, *B*, and *E* are obtained as follows:

$$A=\begin{bmatrix}-918.8 & -9938.5\\ 467.1 & -40\end{bmatrix},\ B=\begin{bmatrix}450820\\ -1712.7\end{bmatrix},\ E=\begin{bmatrix}21277 & 0\\ 0 & -1000\end{bmatrix}$$

Substituting the above matrices *A*, *B*, and *C* into Eqs. (4.6) and (4.7), and setting $\lambda_1 = \lambda_2 = -1$, the state feedback controllers F(γ, ε) and K(γ, ε) are obtained as follows:

$$F(\gamma,\varepsilon)=\begin{bmatrix}0.0020-\dfrac{w_o^2 s_x+0.5674}{w_o^2+69287.12}\times\dfrac{0.2709}{\varepsilon}\\[2ex] 0.0220-\dfrac{w_o^2 s_x-0.0000082w_o^2}{w_o^2+69287.12}\times\dfrac{71.30}{\varepsilon}\end{bmatrix}^T \tag{4.17}$$

$$K(\gamma,\varepsilon)=\begin{bmatrix}-2.1277\times10^4 & 0\\ 9.94\times10^3 & 40-\dfrac{1}{\varepsilon}\end{bmatrix}^T \tag{4.18}$$

As mentioned before, γ is the desired disturbance attenuation level of the closed-loop system with the condition $\gamma > \gamma^*$, and γ^* can be obtained through Eq. (4.15). The adjustable parameter is ε, and there exists an $\varepsilon^* > 0$ such that for all $0 < \varepsilon < \varepsilon^*$, the H∞ of the closed-loop system satisfies $\|G_{cl}(s)\|_\infty < \gamma$. The real symmetric matrix s_x is obtained from Eq. (4.12). The weight w_o is used to augment the disturbance attenuation on the output voltage because both the inductor current and the output voltage are included in the control output *z*.

First, set $w_o = 1$ to show the closed-loop characteristics. From Eq. (4.13), the H∞ infimum of the system in Eq. (4.11) is $\gamma^* = 2.1341$. Set $\gamma = 2.2$, then $s_x = 0.0053$ is obtained from Eq. (4.12). Substituting γ and s_x into the above F(γ, ε) and K(γ, ε), the controller in Eq. (4.16) as well as the closed-loop transfer function in Eq. (4.3) is parameterized by the adjustable parameter ε. The closed-loop audio susceptibility and output impedance are shown in Fig. 4.3 (a) and (b), respectively. Lower than about ε = 1/2100, the closed-loop system becomes stable. The disturbance attenuation increases as long as ε decreases. Lower than ε= 1/100000, and it will no longer obviously change, especially for the output impedance.

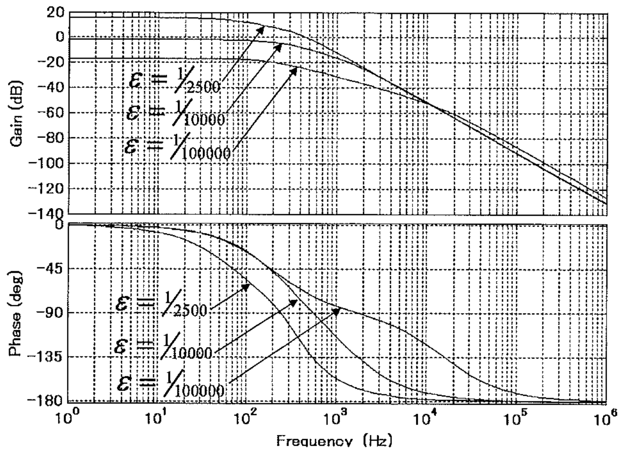

(a) audio susceptibility

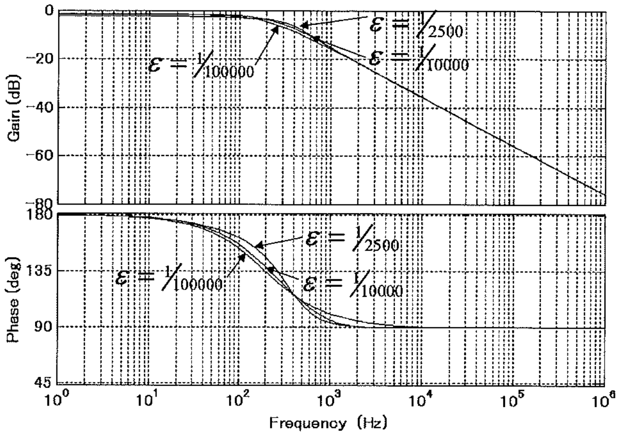

(b) output impedance

Fig. 4.3 Closed-loop dynamic characteristics ($w_o = 1$).

Then, set $w_o = 3$ to augment the disturbance attenuation effect on the output voltage. Similarly, the H∞ infimum of the system in Eq. (4.11) is $\gamma^* = 2.1603$. Set $\gamma = 2.2$, then $s_x = 0.0031$ is obtained. The closed-loop audio susceptibility and output impedance are shown in Fig. 4.4. Lower than about ε = 1/4000, the closed-loop system becomes stable. Lower than ε = 1/15000, the disturbance attenuation will no longer obviously change.

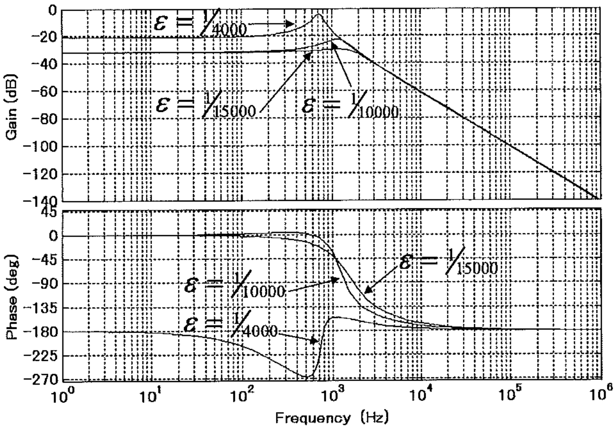

(a) audio susceptibility

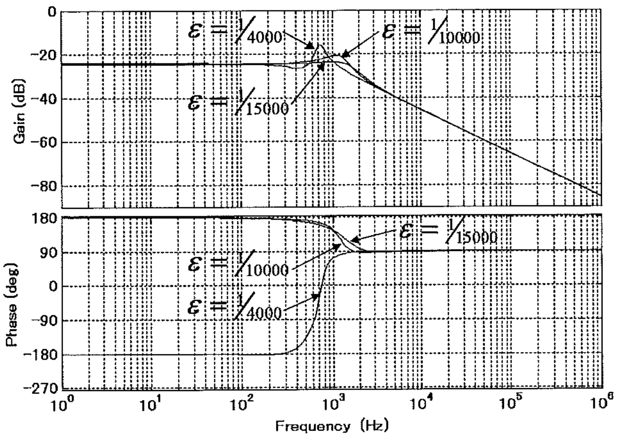

(b) output impedance

Fig. 4.4 Closed-loop dynamic characteristics ($w_o = 3$).

Next, set $w_o = 5$ to further augment the disturbance attenuation effect on the output voltage. Similarly, the H∞ infimum of the system in Eq. (4.11) is $\gamma^* = 2.1628$. Set $\gamma = 2.2$, then $s_x = 0.0022$ is obtained. The closed-loop audio susceptibility and output impedance are shown in Fig. 4.5. Lower than about $\varepsilon = 1/6000$, the closed-loop system becomes stable. Lower than $\varepsilon = 1/18000$, the disturbance attenuation will no longer obviously change.

For $w_o = 5$, the closed-loop dynamic responses of the output voltage to a step change in the disturbances are shown in Fig. 4.6. The response for $\varepsilon = 1/6000$ is not drawn because the peak value is too large. As shown in Fig. 4.6, the fluctuations in the output voltage from the DC operating point will go positive and remain a very small steady state error when a disturbance appears in the input voltage, while it will go negative before reach the steady state when a disturbance appears in the load.

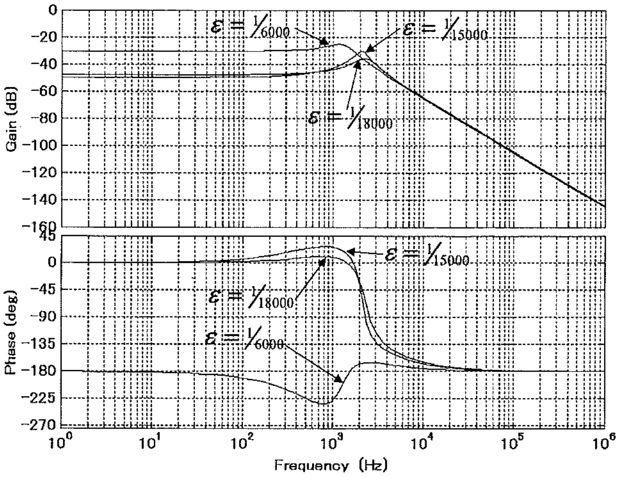

(a) audio susceptibility

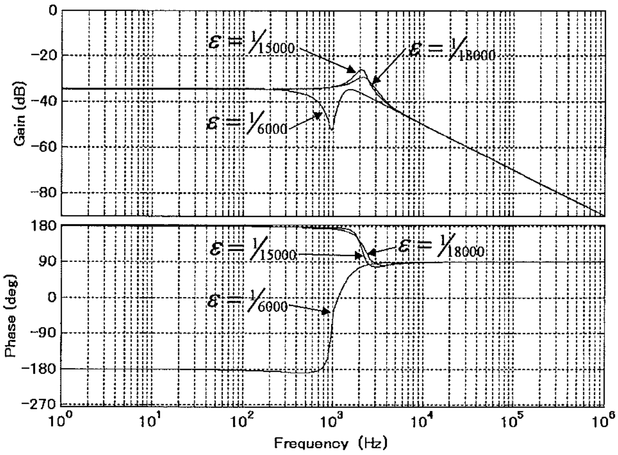

(b) output impedance

Fig. 4.5 Closed-loop dynamic characteristics ($w_o = 5$).

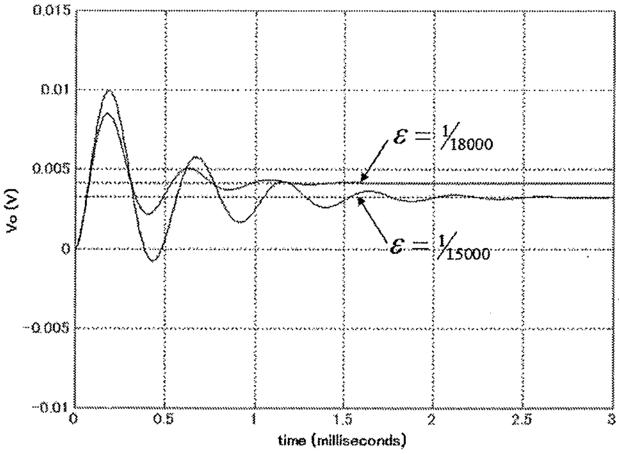

(a) response to a step change in the input voltage v_g

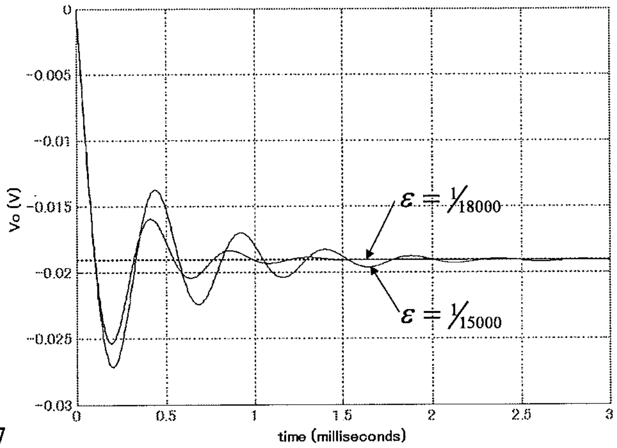

u7

(b) response to a step change in the load current i_o

Fig. 4.6 Closed-loop dynamic response of v_o to a step change ($w_o = 5$).

Although larger can further enhance the disturbance attenuation on the output voltage, Figs. 4.6 and 4.7 show that good disturbance attenuation has been obtained.

4.4.2 Practical experiments

For $w_o = 5$ and $\gamma = 2.2$, the controller in Eq. (4.16) is written in Eq. (4.19). To execute the obtained controller on a digital processor, the bilinear transformation $s = 2(z-1)/T_s(z+1)$, where T_s is the switching period, is utilized to discrete the continuous controller. The discrete controller for $\varepsilon = 1/18000$ is obtained in Eq. (4.20).

$$\begin{cases} \dot{p}(t) = \begin{bmatrix} -\dfrac{1.0967}{\varepsilon} & 9938.5-\dfrac{25.4108}{\varepsilon} \\ 506.7877+\dfrac{0.0042}{\varepsilon} & 11326-\dfrac{0.9034}{\varepsilon} \end{bmatrix} p(t) + \begin{bmatrix} 21277 & -9938.5 \\ 0 & -40+\dfrac{1}{\varepsilon} \end{bmatrix} \begin{bmatrix} \hat{v}_g(t) \\ \hat{v}_o(t) \end{bmatrix} \\ \hat{d}(t) = \begin{bmatrix} 0.0020-\dfrac{2.4326}{10^6\varepsilon} & 0.0220-\dfrac{5.6364}{10^5\varepsilon} \end{bmatrix} p(t) \end{cases} \tag{4.19}$$

$$\begin{cases} p(k+1) = \begin{bmatrix} 0.8717 & -2.7209 \\ 0.0036 & 0.9623 \end{bmatrix} p(k) + \begin{bmatrix} 51.3654 & -99.9147 \\ 0.0828 & 45.4991 \end{bmatrix} \begin{bmatrix} \hat{v}_g(k) \\ \hat{v}_o(k) \end{bmatrix} \\ \hat{d}(k) \quad = \begin{bmatrix} -0.0001 & -0.0023 \end{bmatrix} p(k) + \begin{bmatrix} -0.0029 & -0.0524 \end{bmatrix} \begin{bmatrix} \hat{v}_g(k) \\ \hat{v}_o(k) \end{bmatrix} \end{cases} \tag{4.20}$$

A digital 16 bit processor NJU20010 produced by the New Japan Radio Corporation is used to execute the above digital controller. The limit of duty ratio is set to 0.05~0.88. The slew rates of the load and the input voltage are 250mA/μs and 2.0V/μs, respectively. Fig. 4.7 shows the practical experimental results. The experimental environment is the same to Fig. 3.10 in chapter 3.

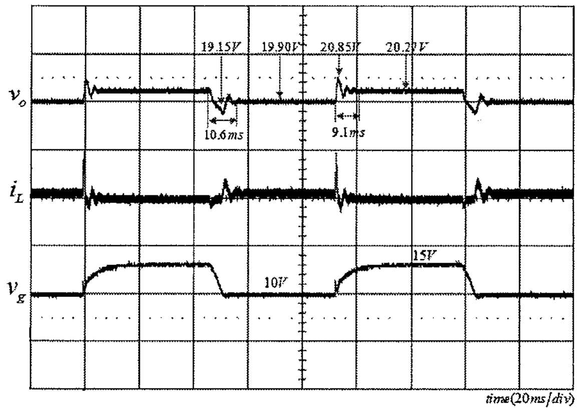

(a) sudden change in the input voltage experiment

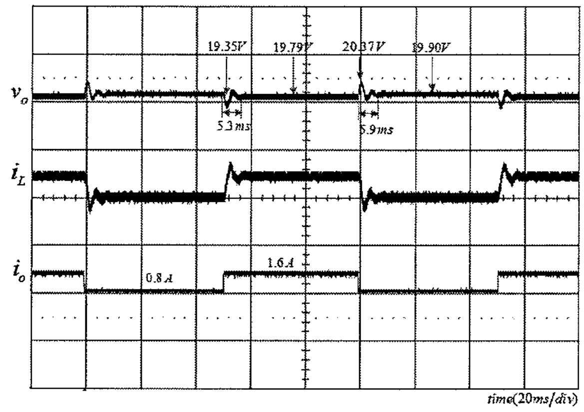

(b) sudden change in the load current experiment

Fig. 4.7 Dynamic responses of output voltage by the digital controller.

4.5 Conclusions

For the conventional LO-based sensorless multi-loop control of a boost converter, there are at least six parameters relating with the closed-loop characteristics. For the proposed robust H∞ synthesis approach, a compact sensorless controller is parameterized by an adjustable parameter behaving like a 'knob' on the closed-loop characteristics, so that the closed-loop characteristics evaluation becomes very straightforward. Simulations show the closed-loop characteristics evaluation process. Practical experiments show that the practical dynamic responses are very good. The derived sensorless controller is general to the boost converters having a same topology. The proposed H∞ synthesis approach can also be easily extent to other converters such as buck-boost and quadratic converters.

Part II

A Low-Order Sensorless Controller

4.6 Problem Formulation

The block diagram of the robust H∞ control of a switching converter is redrawn in Fig. 4.8. The disturbance is $w \in R^l$, the controlled output is $z \in R^q$, the controller output is $u \in R^m$, and the measured output is $y \in R^p$. A weight matrix W is used to adjust the disturbance attenuation on the controlled output z. Define the state space equation of the converter in Eq. (4.21). A compact sensorless controller is written in Eq. (4.22).

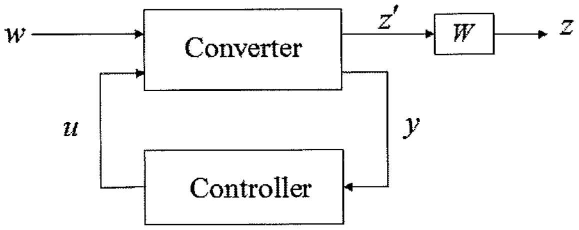

Fig. 4.8 Block diagram of robust H∞ control.

$$Converter: \begin{cases} \dot{x} = Ax + Bu + Ew \\ y = C_1x + D_1w \\ z = C_2x + D_2u \end{cases} \tag{4.21}$$

$$Controller: \begin{cases} \dot{p} = Kp + Ly \\ u = Mp + Ny \end{cases} \tag{4.22}$$

where $x \in R^n$ is the system state including the inductor current and the capacitor voltage.

Generally, the order of the controller in Eq. (4.22) is the same to the system in Eq. (4.21) with an order *n*. However, the order of the controller can be reduced to *n–rank*[C_1 D_1]+*rank*(D_1)≤*n*. A low order controller has the merit of less computation volume or simpler circuit, and is more suitable for real-time control.

Mainly, there are two H∞ synthesis approaches to designing a lower order controller. One approach is to solve the following AREs in Eqs. (4.23) and (4.24) with the conditions in Eq. (4.25) to construct a low-order controller as introduced in [56] [57]:

$$Y\alpha^T(A-G)^T\tau^T+\tau(A-G)\alpha Y+Y\alpha^T(\gamma^{-2}C_1^TC_1+G^TG-2A^TC_2^TC_2A)\alpha Y+\tau B_1B_1^T\tau^T=0 \quad (4.23)$$

$$Y\alpha^T(A-G)^T\tau^T+\tau(A-G)\alpha Y+Y\alpha^T(\gamma^{-2}C_1^TC_1+G^TG-2A^TC_2^TC_2A)\alpha Y+\tau B_1B_1^T\tau^T=0 \quad (4.24)$$

$$\begin{aligned} Z^{-1}\tau-\tau+\gamma^{-2}Y\alpha^TX=0 \\ ZY>0 \end{aligned} \quad (4.25)$$

where $G = BB^TC_2{}^TC^2$, α is a constant matrix, *X* and *Y* are the solutions to be found, and γ is the desired disturbance attenuation level.

The other approach is to solve the following LMIs as introduced in [58] [59]:

$$\begin{gathered}
\begin{bmatrix} \hat{A}_{22}X+X\hat{A}_{22}^T-\hat{B}_{22}\hat{B}_{22}^T & X\hat{C}_{12}^T & \gamma^{-1}\hat{B}_{12} \\ \hat{C}_{12}X & -I & \gamma^{-1}\hat{D}_{11} \\ \gamma^{-1}\hat{B}_{12}^T & \gamma^{-1}\hat{D}_{11}^T & -I \end{bmatrix}<0 \\
\begin{bmatrix} \hat{A}_{22}^TY+Y\hat{A}_{22}-\hat{C}_{22}^T\hat{C}_{22} & Y\hat{B}_{12} & \gamma^{-1}\hat{C}_{12}^T \\ \hat{B}_{12}^TY & -I & \gamma^{-1}\hat{D}_{11} \\ \gamma^{-1}\hat{C}_{12} & \gamma^{-1}\hat{D}_{11} & -I \end{bmatrix}<0 \\
-\begin{bmatrix} X & \gamma^{-1}T_{22} \\ \gamma^{-1}T_{22}^T & Y \end{bmatrix}<0
\end{gathered} \quad (4.26)$$

It can be seen that, especially for a low-order controller, an exhaustive solution search procedure is required to solve the AREs or LMIs. In this chapter, a novel H∞ synthesis approach is proposed to design a low order sensorless controller for boost converters. The proposed H∞ approach need not solve any ARE or LMI, and most importantly, makes the closed-loop characteristics evaluation straightforward by parameterizing the controller with an adjustable parameter which behaves like a 'knob' on the dynamic performance [60].

4.7 Introduction of the Proposed Robust H∞ Synthesis Approach

The closed-loop transfer function $G_{cl}(s)$ of the system in Eq. (4.21) with the controller in Eq. (4.22), that is from the disturbance *w* to the controlled output *z* is written as:

$$G_{cl}(s) = C_{cl}(sI - A_{cl})^{-1} B_{cl} + D_{cl} \tag{4.27}$$

where

$$A_{cl} = \begin{bmatrix} A + BNC_1 & BM \\ LC_1 & K \end{bmatrix}, \quad B_{cl} = \begin{bmatrix} E + BND_1 \\ LD_1 \end{bmatrix}$$

$$C_{cl} = \begin{bmatrix} C_2 + D_2NC_1 & D_2M \end{bmatrix}, \quad D_{cl} = D_2ND_1$$

The basis of the proposed robust H∞ synthesis approach is to decompose the system in Eq. (4.21) into a special coordinate basis (SCB) [50] [51]. Through SCB decomposition, it is easy to check the solvability conditions, and design the low-order controller by a step-by-step procedure, as presented from the following.

4.7.1 Solvability conditions

The solvability conditions are the same as given in subsection 4.3.1.

4.7.2 Design Procedure of a Low Order Controller

Referring to [51] [61] [62], the design procedure of a low-order controller in Eq. (4.22) is as follows:

Step 1: Decompose the system in Eq. (4.21) into SCB and check the solvability conditions;

Step 2: Compute the H∞ infimum γ^* of the system in Eq. (4.21);

Step 3: Set any $\gamma > \gamma^*$ and define an auxiliary system in Eq. (4.28);

$$\begin{cases} \dot{x}_{pq} = A_{pq}x_{pq} + B_{pq}u + E_{pq}w_{pq} \\ y \;= C_{1p}x_{pq} \qquad\quad + D_{1pq}w_{pq} \\ z_{pq} = C_{2p}x_{pq} + D_{2pq}u \end{cases} \tag{4.28}$$

where

$$A_{pq} := A + EE^T P\gamma^{-2} + (\gamma^2 I - QP)^{-1} QC_{2p}^T C_{2p}$$

$$B_{pq} := B + (\gamma^2 I - QP)^{-1} QC_{2p}^T D_{2p}$$

$$E_{pq} := (I - QP\gamma^{-2})^{-1} E_q$$

$$C_{1p} := C_1 + D_1 E^T P\gamma^{-2}$$

Through the SCB decomposition of Eq. (4.21), P, Q, as well as C_{1p}, D_{1pq}, C_{2p}, and D_{2pq} can be obtained.

Step 4: Transform the system in Eq. (4.28) into the form in Eq. (4.29);

$$\begin{cases} \dot{x} = \begin{bmatrix} A_{11} & A_{12} \\ A_{21} & A_{22} \end{bmatrix} x + \begin{bmatrix} B_1 \\ B_2 \end{bmatrix} u + \begin{bmatrix} E_1 \\ E_2 \end{bmatrix} w_{pq} \\ y = \begin{bmatrix} 0 & C_{1,02} \\ I_k & 0 \end{bmatrix} x + \begin{bmatrix} D_{1,0} \\ 0 \end{bmatrix} w_{pq} \\ z = \begin{bmatrix} C_{2,1} & C_{2,2} \end{bmatrix} x + D_2 u \end{cases} \tag{4.29}$$

Step 5: Design a full state feedback controller $u = F_p(\gamma, \varepsilon)x$ for the following subsystem of the system in Eq. (4.29);

$$\begin{cases} \dot{x} = Ax + Bu + Ew_{pq} \\ y = x \\ z = C_{2p}x + D_{2pq}u \end{cases} \tag{4.30}$$

Step 6: Design a full state feedback controller $u = K_Q(\gamma, \varepsilon)$x for the following subsystem of the system in Eq. (4.29);

$$\begin{cases} \dot{x} = A_{22}^T x + \begin{bmatrix} C_{1,02}^T & A_{12}^T \end{bmatrix} u + C_{2,2}^T w \\ y = x \\ z = E_2^T x + \begin{bmatrix} D_{1,0}^T & E_1^T \end{bmatrix} u \end{cases} \tag{4.31}$$

Step 7: Denote $F_P(\gamma, \varepsilon) = [F_{P1} \quad F_{P2}]$, $K_Q(\gamma, \varepsilon) = [K_{Q1} \quad K_{Q2}]$. A low order controller in Eq. (4.22) is expressed as follows:

$$\begin{cases} \dot{p} = Kp + Ly \\ u = Mp + Ny \end{cases} \tag{4.32}$$

where

$$K = A_{22} + K_{Q1}C_{1,02} + K_{Q2}A_{12} + (B_2 - K_{Q2}B_1)F_{P2}$$

$$L = \begin{bmatrix} -K_{Q1} & A_{21} + K_{Q2}A_{11} - (A_{22} + K_{Q1}C_{1,02} + K_{Q2}A_{12})K_{Q2} \end{bmatrix} \\ + (B_2 + K_{Q2}B_1)\begin{bmatrix} 0 & F_{P1} - F_{P2}K_{Q2} \end{bmatrix}$$

$$M = F_{P2}$$

$$N = \begin{bmatrix} 0 & F_{P1} - F_{P2}K_{Q2} \end{bmatrix} N = \begin{bmatrix} 0 & F_{P1} - F_{P2}K_{Q2} \end{bmatrix}$$

The symbol γ represents the desired disturbance attenuation level satisfying $\gamma > \gamma^*$. γ^* is the H∞ infimum of the system in Eq. (4.21) and can be computed as introduced in [54] [55]. The parameter $\varepsilon > 0$ is tunable. There exists an $\varepsilon^* > 0$ such that for all $0 < \varepsilon < \varepsilon^*$, the closed-loop system becomes internally stable and the γ-suboptimal $\|G_{cl}(s)\|_\infty < \gamma$ is satisfied.

4.8 Derivation of a Low Order Sensorless Controller for Boost Converters

4.8.1 Construction of the small signal average value model

The same boost converter is redrawn in Fig. 4.9, and the small signal average value model of the boost converter in CCM is rewritten in Eq. (4.33).

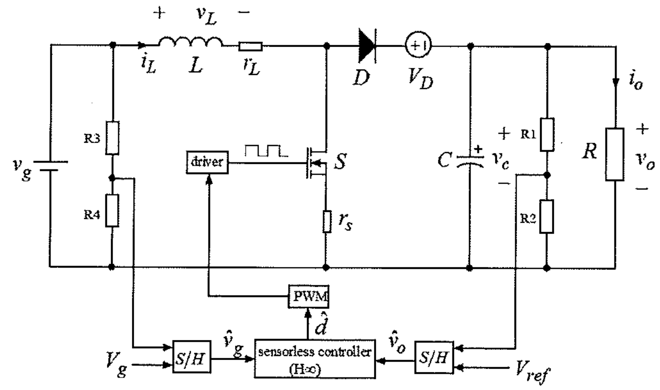

Fig. 4.9 Sensorless controlled boost converter.

$$\dot{x} = Ax + B\hat{d} + Ew \tag{4.33}$$

where $x = [\hat{\imath}_L \quad \hat{v}_c]$, $w = [\hat{v}_g \quad \hat{\imath}_o]$, and

$$A = \begin{bmatrix} -\dfrac{r_L + Dr_s}{L} & -\dfrac{D'}{L} \\ \dfrac{D'}{C} & -\dfrac{1}{RC} \end{bmatrix}, \quad B = \begin{bmatrix} \dfrac{(D'R - r_s)V_g + (r_s + r_L)V_D}{L(r_L + Dr_s + D'^2 R)} \\ -\dfrac{V_g - D'V_D}{C(r_L + Dr_s + D'^2 R)} \end{bmatrix}, \quad E = \begin{bmatrix} \dfrac{1}{L} & 0 \\ 0 & -\dfrac{1}{C} \end{bmatrix}$$

and

$$D' = \frac{r_s V_{ref} + RV_g}{2R(V_{ref} + V_D)}\left(1 + \sqrt{1 - \frac{4R(r_L + r_s)(V_{ref} + V_D)V_{ref}}{(r_s V_{ref} + RV_g)^2}}\right) \tag{4.34}$$

The symbol D denotes the duty ratio at a given operating point and $D' = 1 - D$, and $\hat{d}$ represents the duty ratio adjustment from the given operation point when a disturbance occurs. Ignoring the equivalent series resistance of the output capacitor, $\hat{v}_c$ is equivalent to $\hat{v}_o$. For convenience, define

$$A = \begin{bmatrix} a_{11} & a_{12} \\ a_{21} & a_{22} \end{bmatrix}, \quad B = \begin{bmatrix} b_1 \\ b_2 \end{bmatrix}, \quad E = \begin{bmatrix} e_1 & 0 \\ 0 & e_2 \end{bmatrix}$$

4.8.2 Construction of the state space equation for the robust H∞ approach

From the small signal model in Eq. (4.33), the state space equation for the proposed robust H∞ control is written as:

$$\begin{cases} \dot{\hat{x}} = A\hat{x} + B\hat{d} + E\hat{w} \\ y = C_1\hat{x} + D_1\hat{w} \\ z = C_2\hat{x} + D_2\hat{d} \end{cases} \tag{4.35}$$

The matrices A, B and E are the same to Eq. (4.32), and

$$C_1 = \begin{bmatrix} 0 & 0 \\ 0 & 1 \end{bmatrix},\quad D_1 = \begin{bmatrix} 1 & 0 \\ 0 & 0 \end{bmatrix},\quad C_2 = \begin{bmatrix} 1 & 0 \\ 0 & w_o \end{bmatrix},\quad D_2 = \begin{bmatrix} 0 \\ 0 \end{bmatrix}$$

The measurable output is $y = [\hat{v}_g \quad \hat{v}_o]^T$, the controlled output is $z = [\hat{i}_L \quad \hat{v}_o]^T$, and w_o is a weight on the output voltage as shown in Fig. 4.10. Denote

$$A = \begin{bmatrix} a_{11} & a_{12} \\ a_{21} & a_{22} \end{bmatrix},\quad B = \begin{bmatrix} b_1 \\ b_2 \end{bmatrix},\quad E = \begin{bmatrix} e_1 & 0 \\ 0 & e_2 \end{bmatrix}$$

4.8.3 SCB decomposition of the system in Eq. (4.35)

The SCB decomposition of the subsystem Σ_P: = (A, B, C_2, D_2) is obtained as:

$$\begin{gathered} \begin{bmatrix} \dot{x}_b \\ \dot{x}_d \end{bmatrix} = \begin{bmatrix} a_{22} - \frac{b_2}{b_1}a_{12} & w_o(a_{21} - \frac{b_2}{b_1}(a_{11} - a_{22}) - \frac{b_2^2}{b_1^2}a_{12}) \\ a_{11} + \frac{b_2}{b_1}a_{12} & \frac{a_{12}}{w_o} \end{bmatrix} \begin{bmatrix} x_b \\ x_d \end{bmatrix} + \begin{bmatrix} 0 \\ b_1 \end{bmatrix}\hat{d} \\ \begin{bmatrix} y_d \\ y_b \end{bmatrix} = \begin{bmatrix} x_d \\ x_b \end{bmatrix} \end{gathered} \tag{4.36}$$

and

$$\Gamma_{sP} = \begin{bmatrix} 0 & 1 \\ \frac{1}{w_o} & \frac{b_2}{b_1} \end{bmatrix}, \; \Gamma_{oP} = \begin{bmatrix} 1 & 0 \\ w_o \frac{b_2}{b_1} & 1 \end{bmatrix}, \; \Gamma_{iP} = \frac{1}{b_1}$$

The SCB decomposition of the subsystem $\Sigma_Q := (A^T, C_1^T, E^T, D_1^T)$ is obtained as:

$$\begin{gathered} \begin{bmatrix} \dot{\bar{x}}_a \\ \dot{x}_d \end{bmatrix} = \begin{bmatrix} a_{11} & a_{21} \\ a_{12} & a_{22} \end{bmatrix} \begin{bmatrix} \bar{x}_a \\ x_d \end{bmatrix} + \begin{bmatrix} 0 & 0 \\ 0 & 1 \end{bmatrix} \begin{bmatrix} u_0 \\ u_d \end{bmatrix} \\ \begin{bmatrix} y_0 \\ y_d \end{bmatrix} = \begin{bmatrix} e_1 & 0 \\ 0 & 1 \end{bmatrix} \begin{bmatrix} \bar{x}_a \\ x_d \end{bmatrix} + \begin{bmatrix} 1 & 0 \\ 0 & 0 \end{bmatrix} \begin{bmatrix} u_0 \\ u_d \end{bmatrix} \end{gathered} \tag{4.37}$$

and

$$\Gamma_{sQ} = \begin{bmatrix} 1 & 0 \\ 0 & 1 \end{bmatrix}, \; \Gamma_{oQ} = \begin{bmatrix} 1 & 0 \\ 0 & e_2 \end{bmatrix}, \; \Gamma_{iQ} = \begin{bmatrix} 1 & 0 \\ 0 & 1 \end{bmatrix}$$

4.8.4 Solvability Verification

As proved in subsection 4.3.4, the controller in Eq. (4.22) for the system in Eq. (4.21) is solvable, however, a complicated computation of the H∞ infimum γ^* is required.

4.8.5 Computation of the H∞ infimum of the system in Eq. (4.35)

Through SCB decomposition, it is found that the H∞ infimum of the subsystem Σ_Q is $\gamma_Q^* = 0$. Thus, the H∞ infimum of the system in Eq. (4.35) is determined only by the subsystem Σ_P. Referring to [55], for a given $\gamma > 0$, a positive real symmetric solution s_x to the algebraic Riccati equation in Eq. (4.38) should exist.

$$s_x A_x + A_x^T s_x + s_x E_x E_x^T s_x \gamma^{-2} - s_x B_x B_x^T s_x + C_x^T C_x = 0 \tag{4.38}$$

where

$$A_x = a_{22} - \frac{b_2}{b_1} a_{12} - \frac{w_o^2 b_1 b_2}{b_1^2 + w_o^2 b_2^2} \left(a_{21} - \frac{b_2}{b_1}(a_{11} - a_{22}) - \frac{b_2^2}{b_1^2} a_{12}\right)$$

$$B_x B_x^T = \frac{w_o^2 b_1^2}{b_1^2 + w_o^2 b_2^2}(a_{21} - \frac{b_2}{b_1}(a_{11} - a_{22}) - \frac{b_2^2}{b_1^2} a_{12})^2$$

$$C_x^T C_x = \frac{b_1^2}{b_1^2 + w_o^2 b_2^2}$$

$$E_x E_x^T = w_o^2 (\frac{b_2^2}{b_1^2} e_1^2 + e_2^2)$$

According to the above solution existing condition, the H∞ infimum of Eq. (4.35) is obtained as:

$$\gamma^* = \frac{\sqrt{(b_1^2 e_2^2 + b_2^2 e_1^2)(b_1^2 + w_o^2 b_2^2)}}{b_1^2 a_{21} - b_1 b_2 (a_{11} - a_{22}) - b_2^2 a_{12}} \tag{4.39}$$

4.8.6 Derivation of a low-order controller

Although the system in Eq. (4.29) can be constructed through the SCB decomposition of the system in Eq. (4.35), it can be seen that the system in Eq. (4.35) is already very similar to the system in Eq. (4.29). Therefore, a transformation $T_x = [0 \quad 1;\ 1 \quad 0]$ on the system state x is performed to transform Eq. (4.35) into the form in Eq. (4.29).

Following the design procedure described in the subsection 4.7.2, a low-order controller in Eq. (4.22) is obtained as follows:

$$\begin{cases} \overset{\bullet}{p} = Kp + Ly \\ \hat{d} = Mp + Ny \end{cases} \tag{4.40}$$

where

$$K = -\frac{w_o^2 b_2 (b_1^2 a_{21} - b_1 b_2 (a_{11} - a_{22}) - b_2^2 a_{12}) s_x - b_1^3}{b_1 (b_1^2 + w_o^2 b_2^2)} \frac{\lambda}{\varepsilon}$$

$$L = \begin{bmatrix} e_1 & \dfrac{w_o^2 (b_1^2 a_{21} - b_1 b_2 (a_{11} - a_{22}) - b_2^2 a_{12}) s_x + w_o^2 b_1 b_2}{b_1^2 + w_o^2 b_2^2} \dfrac{\lambda}{\varepsilon} \end{bmatrix}$$

$$M=-\frac{a_{11}}{b_1}-\frac{w_o^2 b_2(b_1^2 a_{21}-b_1 b_2(a_{11}-a_{22})-b_2^2 a_{12})s_x-b_1^3}{b_1^2(b_1^2+w_o^2 b_2^2)}\frac{\lambda}{\varepsilon}$$

$$N=\begin{bmatrix}0 & \frac{w_o^2}{b_1}\frac{(b_1^2 a_{21}-b_1 b_2(a_{11}-a_{22})-b_2^2 a_{12})s_x+b_1 b_2}{b_1^2+w_o^2 b_2^2}\frac{\lambda}{\varepsilon}-\frac{a_{12}}{b_1}\end{bmatrix}$$

The λ in Eq. (4.40) can be set to any negative value, for example –1. The parameter ε > 0 is tunable.

4.9 Simulations and Experiments

The same boost converter with parameters listed in Table 2.1 is used to show the straightforward closed-loop characteristics evaluation.

4.9.1 Simulations of the low-order sensorless controller

Setting λ = –1, the low order sensorless controller is obtained in Eq. (4.41).

$$\begin{cases}\dot{p}=-\frac{1.6148\times10^5 w_o^2 s_x+9.1622\times10^4}{9.1622\times10^4+1.3223w_o^2}\frac{1}{\varepsilon}p+\begin{bmatrix}21277 & -\frac{9.4283\times10^7 w_o^2 s_x-772.10w_o^2}{2.0323\times10^5+2.9332w_o^2}\frac{1}{\varepsilon}\end{bmatrix}\begin{bmatrix}\hat{v}_g\\ \hat{v}_o\end{bmatrix}\\ \hat{d}=(0.002-\frac{1.6148w_o^2 s_x+0.9162}{4.1304\times10^5+5.9613w_o^2}\frac{1}{\varepsilon})p+\begin{bmatrix}0 & 0.022-\frac{9.4283\times10^5 w_o^2 s_x-7.7210w_o^2}{9.1622\times10^8+1.3223\times10^4 w_o^2}\frac{1}{\varepsilon}\end{bmatrix}\begin{bmatrix}\hat{v}_g\\ \hat{v}_o\end{bmatrix}\end{cases}$$

(4.41)

First, set $w_o = 1$ to examine the closed-loop characteristics. From Eq. (4.39), the H∞ infimum of the system in Eq. (4.35) is $\gamma^* = 2.1341$. Set $\gamma = 2.2$, then $s_x = 0.0053$ can be obtained from Eq. (4.38). Substituting γ and s_x into Eq. (4.41), the closed-loop audio susceptibility and output impedance are shown in Fig. 4.10 (a) and (b), respectively. Lower than about ε=1/6000, the disturbance on the output voltage begins to be attenuated. The disturbance attenuation increases as long as decreases. Lower than ε = 1/100000, the disturbance attenuation will no longer change obviously, especially for output impedance.

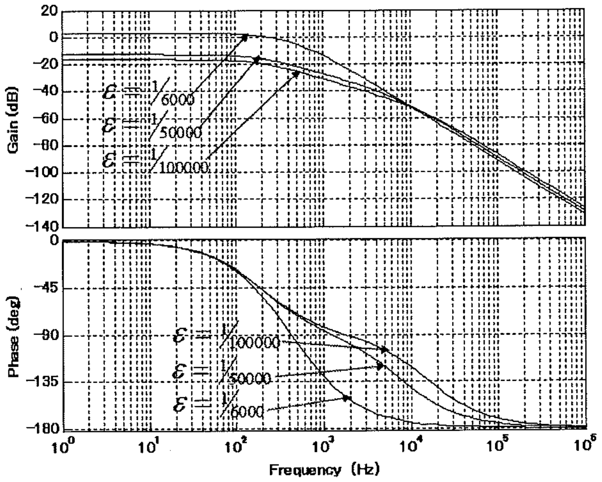

(a) audio susceptibility

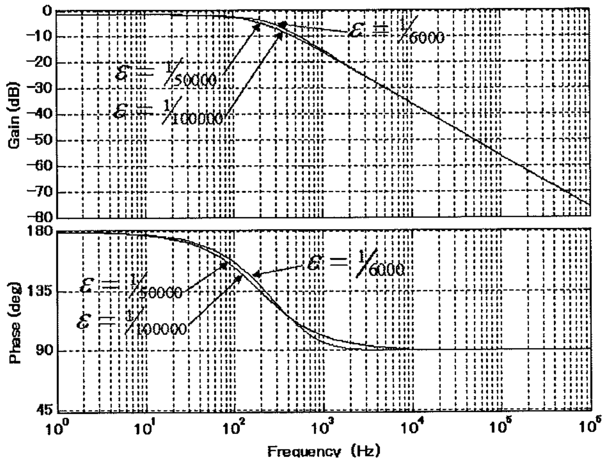

(b) output impedance

Fig. 4.10 Bode plots of closed-loop characteristics ($w_o = 1$).

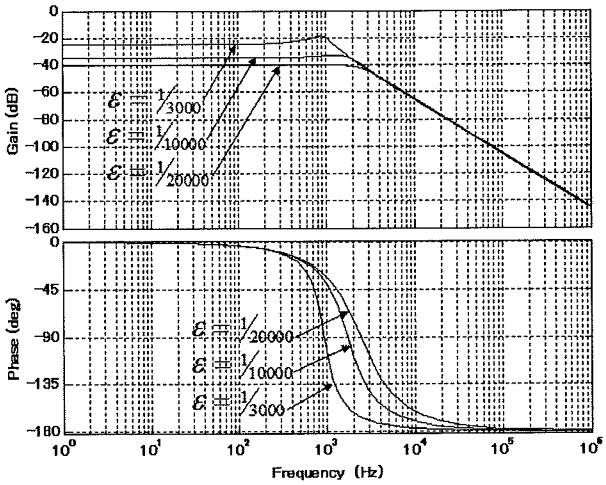

(a) audio susceptibility

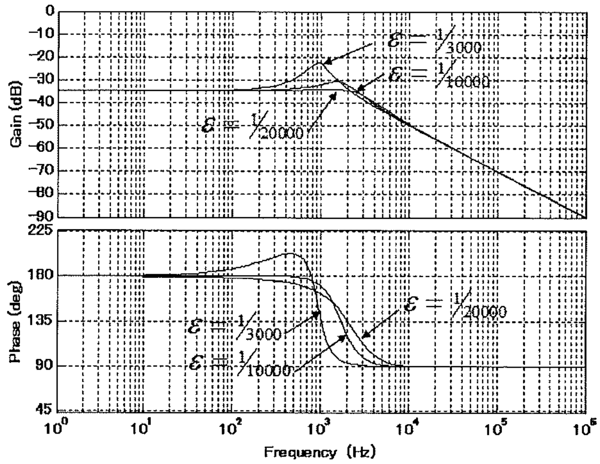

(b) output impedance

Fig. 4.11 Bode plots of closed-loop characteristics ($w_o = 5$).

Next, set $w_o = 5$ to augment the disturbance attenuation effect on the output voltage. Similarly, the H∞ infimum of the system in Eq. (4.35) is $\gamma^* = 2.1628$. Set $\gamma = 2.2$, then $s_x = 0.0022$ is obtained. The closed-loop characteristics are shown in Fig. 4.11. Lower than about $\varepsilon = 1/3000$, the disturbance on the output voltage begins to be attenuated much. Lower than $\varepsilon = 1/20000$, the disturbance attenuation will no longer change obviously.

Next, set $w_o = 10$ to further augment the disturbance attenuation effect on the output voltage. The H∞ infimum of the system in Eq. (4.35) is $\gamma^* = 2.1640$. Set $\gamma = 2.2$, then $s_x = 0.0013$ is obtained. The closed-loop characteristics are shown in Fig. 4.12. Lower than about $\varepsilon = 1/2000$, the disturbance on the output voltage begins to be attenuated much. Lower than $\varepsilon = 1/8000$, the disturbance attenuation will no longer change obviously. It means that the closed-loop characteristics have approached its limit when $w_o = 10$ and this value can be chosen as the suitable value of ε.

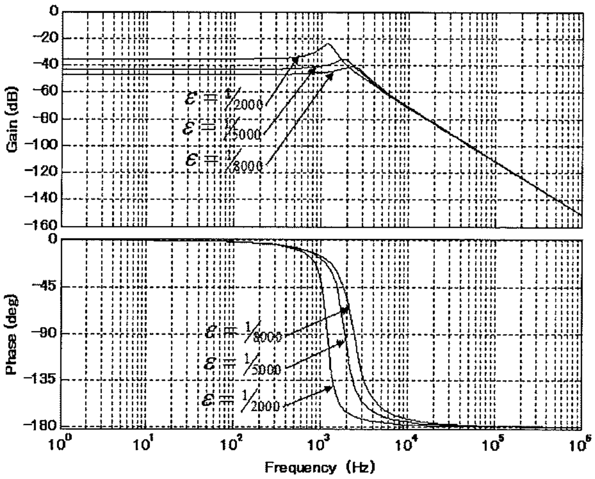

(a) audio susceptibility

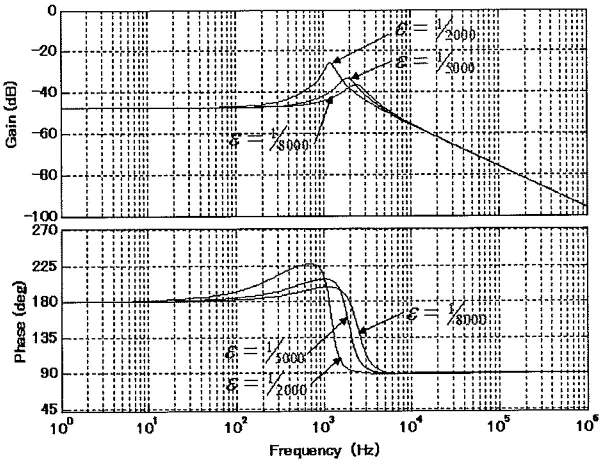

(b) output impedance

Fig. 4.12 Bode plots of closed-loop characteristics ($w_o = 10$).

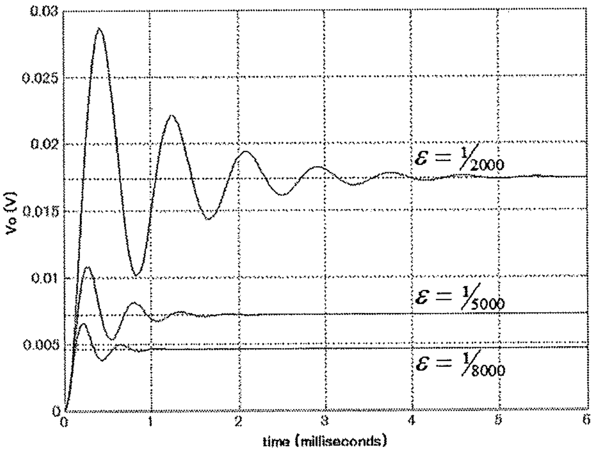

(a) step response of $\hat{v}_o$ to a step change in $\hat{v}_g$

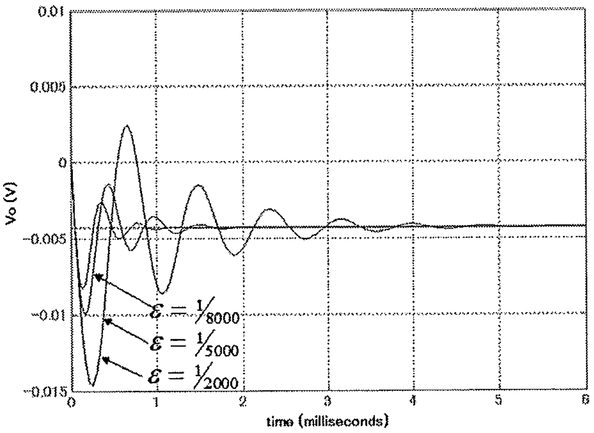

(b) step response of $\hat{v}_o$ to a step change in $\hat{i}_o$

Fig. 4.13 Step responses of output voltage $\hat{v}_o$.

Although larger w_o can further enhance the disturbance attenuation on the output voltage, Fig. 4.13 shows that good disturbance attenuation has been obtained. The closed-loop dynamic responses of the output voltage are shown in Fig. 4.13 for $w_o = 10$.

4.9.2 Practical experiments

Through bilinear transformation $s = 2(z-1)/T_s(z+1)$, where T_s is the switching period, the digital counterpart of the controller in Eq. (4.41) obtained by the proposed H∞ synthesis approach is written in Eq. (4.42) for $w_o = 10$ and $\varepsilon = 1/8000$. The practical dynamic response of output voltage is shown in Fig. 4.14.

$$\begin{cases} p(k+1) = -9572.3p(k) + 53.1831\hat{v}_g(k) - 1242.1\hat{v}_0(k) \\ \hat{d}(k) \ = -0.00005p(k) - 0.0014\hat{v}_g(k) - 1.0483\hat{v}_0(k) \end{cases} \tag{4.42}$$

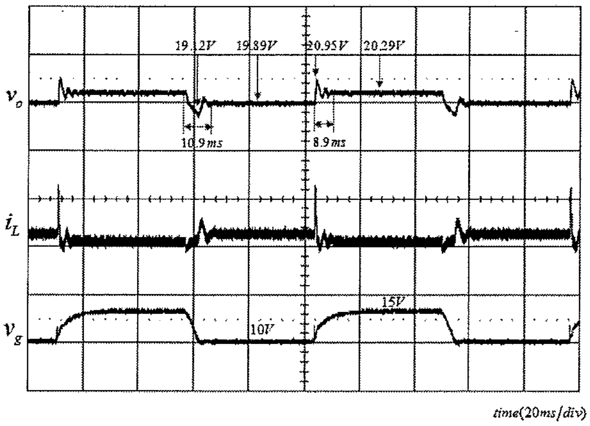

(a) dynamic response when input voltage is disturbed

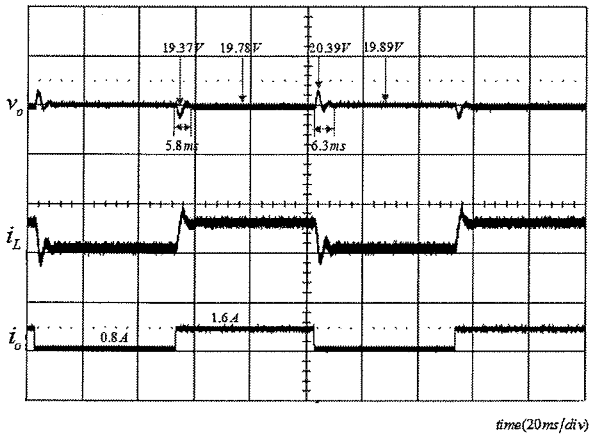

(b) step response of $\hat{v}_o$ to a step change in $\hat{\imath}_o$

Fig. 4.14 Step responses of output voltage $\hat{v}_o$.

The practical experimental environment is the same to Fig. 3.10 in chapter 3.

4.10 Conclusions

Through the proposed robust H∞ synthesis approach, a low-order sensorless controller is derived for a boost converter. The controller is parameterized by an adjustable parameter behaving like a 'knob' on the closed-loop characteristics, which makes the closed-loop characteristics evaluation very straightforward. Compared with the full-order controller, the computation is reduced by one third. Simulations show the straightforward closed-loop characteristics evaluation. Practical experimental results confirmed the simulations. The derived sensorless controller is general for boost converters. The proposed H∞ synthesis approach is also applicable to the sensorless controller design of other converters such as buck-boost and quadratic converters.

5

Sliding Mode Observer for Current Sensorless Control of Boost Converters

A Luenberger observer (LO) only feeds a linear output estimation error back to the observer. In this chapter, a sliding mode observer (SMO), which feeds a nonlinear output estimation error back to the observer, is proposed for the sensorless control of a boost converter to improve its dynamic performance.

5.1 Introduction

For a boost converter in the continuous conduction mode (CCM), analysis in the frequency domain shows that there is a right-half-plane-zero (RHPZ) in the transfer function from the duty ratio to the output voltage [2]. The crossover frequency of the open loop gain is severely restricted by this RHPZ, resulting in poor dynamic performance if single-loop output voltage control is adopted. The time domain analysis of a sliding mode controlled boost converter shows that an unstable inductor current will result if only the output voltage is used [63]. Therefore, either an inductor or a switch current is required for the control of a boost converter in the CCM. This situation is similar to the control of buck-boost and fly-back converters. However, as presented before, a current sampling circuit will unavoidably increase the cost, size, and weight and cause a slight power loss. The sensorless control of boost converters provides a solution to this problem. Some sensorless controls have been introduced in previous papers as follows. The use of the integral of the voltage drop on the inductor to estimate the inductor current was introduced in [16] [64], the use of the predicted inductor current for peak current control was introduced in [65] [66], and the use of a state observer based on the state-space equation was introduced in [17] [18]. Investigation results show that, a Luenberger observer (LO) [18] and Kalman filter (KF) [67] are most effective in observing the inductor current of switching converters. However, some drawbacks have also been pointed out as follows. It was shown in [67] that the robustness to parameter uncertainty and external noise cannot be guaranteed for the LO and KF and that the real-time implementation of the KF involves significant numerical complexity. The theoretical analysis in [75] shows that for the LO, the convergence of the estimation error is only ensured in a bounded region. In the formulas of the LO and KF, a linear output voltage estimation error is fed back to the observer. This means that the estimation error cannot be forced to zero quickly and the convergence accuracy of the observer is not good, as shown in [17] [67].

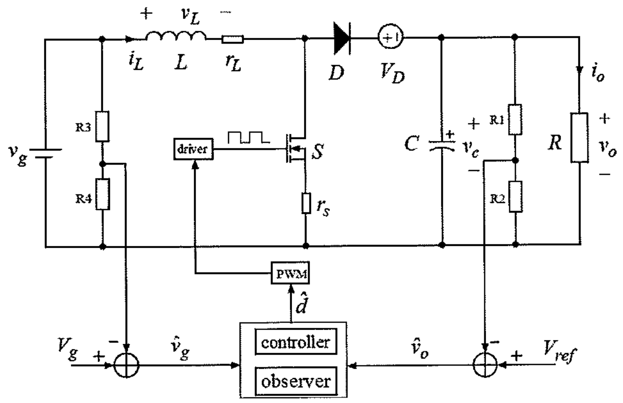

Fig. 5.1 Sensorless controlled boost converter.

The sensorless control of boost converters can be summarized in Fig. 5.1. The inductor current is first estimated using the duty ratio, the input voltage, and the output voltage, and then the estimated inductor current is applied to the controller. From the inductor current estimation methods introduced in [16] [17] [18] [64] [65] [66], the following LO is the most effective method of observing the inductor current of switching mode power suppliers:

$$\begin{aligned} &\overset{\bullet}{\hat{x}} = \Phi(\hat{x}) + \Gamma(\hat{x}, u) + K(y - \hat{y}) \\ &\hat{y} = C\hat{x}(t) \end{aligned} \tag{5.1}$$

here $\hat{x}$ is the estimate of the system state x, and y is the measurable output. The LO can be a nonlinear [18] or linear observer [17] depending on the constructed model of the control object. However, it can be seen that the error between the control system output y and the observer output $\hat{y}$ is fed linearly back to the observer. As a result, the estimation error cannot be forced to zero quickly, and the convergence accuracy of the observer deteriorates in the presence of unknown disturbances [18] [67].

As presented in [68] [69] [70] [71] [72], for a sliding mode observer (SMO) written in Eq. (5.2), a nonlinear output estimation error is fed back to the observer. Provided a bound on the magnitude of the disturbances is known, the SMO can force the estimation error to converge to zero in a finite time, while the observer states converge asymptotically to the actual system states.

$$\begin{aligned} \dot{\hat{x}} &= \Phi(\hat{x}) + \Gamma(\hat{x}, u) + L\,\mathrm{sgn}(y - \hat{y}) \\ \hat{y} &= C\hat{x}(t) \end{aligned} \tag{5.2}$$

Although there have been several studies on the application of the SMO to switching power suppliers [73] [74] [75] [76]; however, there have been no papers introducing the application of the SMO to the sensorless current control of boost, buck-boost, and fly-back converters with a clear description of the SMO. Therefore, in this chapter, an improved discrete SMO is proposed for the sensorless control of boost converters to improve their dynamic performance [77]. Simulations and practical experiments on an NJU20010 digital processor are performed. It is shown that the dynamic performance of the boost converter is greatly improved by the proposed SMO-based control compared with LO-based control.

5.2 Introduction of the Proposed Sliding Mode Observer

Suppose that a discrete linear time-invariant system has the form:

$$\begin{aligned} x(k+1) &= \Phi x(k) + \Gamma u(k) + F\xi(k) \\ y(k) &= Cx(k) \end{aligned} \tag{5.3}$$

where $x(k) \in R^n$ is the state, $y(k) \in R^p$ is the measurable output, $u(k) \in R^m$ is the known input, $\xi(k) \in R^q$ is the bounded disturbance, $q \le p$, and Φ, Γ, F, and C are constant matrices of appropriate dimensions. $\zeta(k)$ is unknown but assumed to be bounded and satisfy:

$$\|\xi(k)\| \le \rho \tag{5.4}$$

where ρ is known. To construct state $x(k)$ in the system given by Eq. (5.3), an improved

SMO is proposed.

5.2.1 Proposed sliding mode observer

The proposed SMO for the system in Eq. (5.3) is written as:

$$\begin{aligned} \hat{x}(k+1) &= \Phi\hat{x}(k) + \Gamma u(k) + G_l e_y(k) + G_n v \\ \hat{y}(k) &= C\hat{x}(k) \end{aligned} \tag{5.5}$$

where

$$e_y(k) = y(k) - \hat{y}(k), \quad v = \mathrm{sgn}(e_y)$$

$\hat{x}(k)$ is the estimate of state $x(k)$, v is a discontinuous feedback compensation, which can eliminate the effect of the nonlinear term $\zeta(k)$ in Eq. (5.3), and, when combined with $u(k)$, it guarantees the asymptotic stability of error estimation. The constant matrix G_n is the observer gain matrix, which guarantees that a sliding mode is attained on the sliding surface in the error space of the state estimation. Compared with Eq. (5.2), a linear output error term $G_l e_y$ is added to the observer in order to enlarge the sliding mode region.

5.2.2 Solvability conditions of the proposed SMO

The necessary and sufficient conditions of the SMO given by Eq. (5.5) for the system in Eq. (5.3) are as follows:

I. $rank(CF) = rank(F)$.

II. The invariant zeros of the triple (Φ, F, C) lie inside the unit circle.

5.2.3 Observation error dynamics

Define $e(k) = x(k) - \hat{x}(k)$ as the state estimation error. From Eqs. (5.3) and (5.5), the reconstruction error is given as follows:

$$e(k+1) = (\Phi - G_l C)e(k) + F\xi(k) - G_n v \tag{5.6}$$

$$e_y(k) = Ce(k) \tag{5.7}$$

Define the sliding surface as

$$s = \{e(k) \mid e_y(k) = 0\} \tag{5.8}$$

As proved in [68] [72], the error system given by Eqs. (5.6) and (5.7) is asymptotically stable, and a convergent sliding-mode motion occurs on the sliding surface defined in Eq. (5.8) under some conditions. Assuming that the ideal sliding mode of the system in Eq. (5.6) is obtained after a finite time k, at which $e_y(k) = 0$, the equivalent control at the sliding stage is obtained as

$$v_{eq}(k) = (CG_n)^{-1}(C\Phi e(k) + CF\xi(k)) \tag{5.9}$$

Substituting Eq. (5.9) into the state error equation Eq. (5.6) gives the reduced order system:

$$e(k+1) = (I - G_n(CG_n)^{-1}C)(\Phi e(k) + F\xi(k)) \tag{5.10}$$

Ideally, the error system in Eq. (5.6) will converge to the origin along the sliding surface in Eq. (5.8) under the control expressed as Eq. (5.9).

5.2.4 Parameter determination of the SMO

To determine the parameters G_l and G_n in Eq. (5.5), the application of a linear transformation to change the coordinates of the system in Eq. (5.3) was introduced in [69] [75], and the use of a linear matrix inequality was introduced in [78]. In this chapter, a simple method introduced in [68] is proposed as follows.

As one of the eigenvalues of $(I - G_n(CG_n)^{-1}C)\Phi$ is zero, G_n can be determined through assigning the other $n - 1$ eigenvalues. Moreover, if there exists a real number such that

$$F = \eta G_n \tag{5.11}$$

and all the eigenvalues of $(I - G_n(CG_n)^{-1}C)\Phi$ lie inside the unit circle on the discrete complex plane, it can be found that $e(k)$ is independent of $\zeta(k)$ through substituting Eq. (5.11) into Eq. (5.10). That is, the sliding motion given by Eq. (5.10) is stable and will not be affected by any disturbance.

Define a discrete Riccati equation as follows:

$$\Phi P \Phi^T - \frac{1}{\alpha + CPC^T} \Phi PC^T CP\Phi^T - P = -Q \tag{5.12}$$

where Q is a positive semi-definite symmetric matrix and α is a positive real number. Solving Eq. (5.12) to find the unique positive definite symmetric matrix P, the matrix G_l is given by

$$G_l = \frac{1}{\alpha + CPC^T} \Phi PC^T \tag{5.13}$$

5.3 Design of SMO-Based Sensorless Control for Boost Converters

5.3.1 Construction of discrete small signal average value model

A boost converter by sliding mode sensorless control is shown in Fig. 5.2, in which several parasitic components are considered. Referring to [2], the small signal average value model of the boost converter in the CCM is constructed as follows:

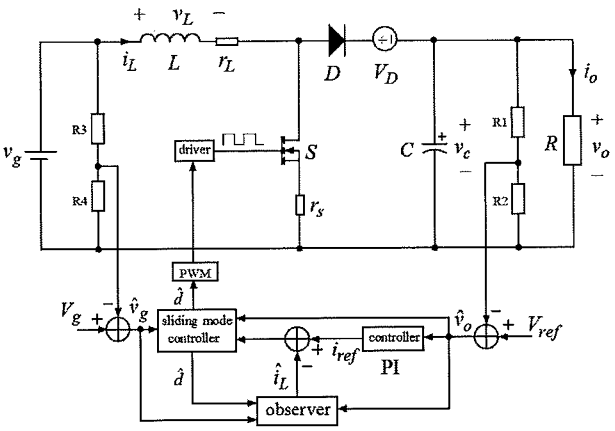

Fig. 5.2 Sliding mode sensorless control of a boost converter.

$$\dot{x} = Ax + Bd + Ew \tag{5.14}$$

where $x = [i_L \quad v_c]$, $w = [v_g \quad i_o]$, and

$$A=\begin{bmatrix} -\frac{r_L+Dr_s}{L} & -\frac{D'}{L} \\ \frac{D'}{C} & -\frac{1}{RC} \end{bmatrix},\quad B=\begin{bmatrix} \frac{(D'R-r_s)V_g+(r_s+r_L)V_D}{L(r_L+Dr_s+D'^2R)} \\ -\frac{V_g-D'V_D}{C(r_L+Dr_s+D'^2R)} \end{bmatrix},\quad E=\begin{bmatrix} \frac{1}{L} & 0 \\ 0 & -\frac{1}{C} \end{bmatrix}$$

and

$$D'=\frac{r_sV_{ref}+RV_g}{2R(V_{ref}+V_D)}(1+\sqrt{1-\frac{4R(r_L+r_s)(V_{ref}+V_D)V_{ref}}{(r_sV_{ref}+RV_g)^2}}) \tag{5.15}$$

where D is the duty ratio in one switching period and $D' = 1 - D$. $x = [i_L \quad v_o]$T and $w = [v_g \quad i_o]^T$ are the corresponding AC small signals. Here, although v_o and v_g are not scaled by the corresponding dividing resistors shown in Fig. 5.2, the parameters of the controllers will be scaled at the execution stage on a digital processor.

To design a discrete SMO and controller, the above state space in Eq. (5.14) should be discretized, and the discrete counterpart is written as

$$x(k+1)=A_dx(k)+B_dd(k)+E_dw(k) \tag{5.16}$$

where $x(k+1) = [i_L(k+1) \quad v_o(k+1)]$, $w(k) = [v_g(k) \quad i_o(k)]$

$$A_d=e^{AT},\quad B_d=\int_0^T e^{A\tau}d\tau B,\quad E_d=\int_0^T e^{A\tau}d\tau E$$

On the basis of Eq. (5.16), the SMO is designed as described in the following section.

5.3.2 Construction of the sliding mode observer

To design the SMO, define

$$x(k)=\begin{bmatrix} i_L(k) \\ v_o(k) \end{bmatrix},\quad u(k)=\begin{bmatrix} d(k) \\ v_g(k) \end{bmatrix},\quad \xi(k)=\begin{bmatrix} i_o(k) \end{bmatrix}$$

First, change Eq. (5.16) into the following form:

$$\begin{cases} x(k+1) = \Phi x(k) + \Gamma u(k) + F\xi(k) \\ y(k) = \begin{bmatrix} 0 & 1 \end{bmatrix} x(k) \end{cases} \tag{5.17}$$

where

$$\Phi = A_d, \quad \Gamma = \begin{bmatrix} B_d & E_d(*,1) \end{bmatrix}, \quad F = \begin{bmatrix} E_d(*,2) \end{bmatrix}$$

Then, the SMO is constructed as follows:

$$\begin{bmatrix} \hat{i}_L(k+1) \\ \hat{v}_o(k+1) \end{bmatrix} = \Phi \begin{bmatrix} \hat{i}_L(k) \\ \hat{v}_o(k) \end{bmatrix} + \Gamma u(k) + G_l e_y(k) + G_n v \tag{5.18}$$

where

$$e_y(k) = y(k) - \hat{y}(k), \quad v = \mathrm{sgn}(e_y)$$

5.3.3 Design of SMO-based sliding mode controller

The SMO in Eq. (5.18) can be used for the average value model based sensorless control of a boost converter, such as multi-loop PI control and state feedback control. As multi-loop PI control is well known to almost all power electronics engineers and researchers, in this chapter, the design of a sliding mode controller, which can maintain better dynamic performance than a linear controller, is introduced in the following.

First, change Eq. (5.16) into the following form:

$$x(k+1) = A_d x(k) + B_d d(k) + E_1 v_g(k) + E_2 i_o(k) \tag{5.19}$$

where

$$E_1 = E_d(*, 1), \quad E_2 = E_d(*, 2)$$

Then, the system state variables are selected as follows to design a discrete sliding mode controller. Both the inductor current error and the output voltage error are used to improve the accuracy of the output voltage.

$$x(k)=\begin{bmatrix} x_1(k) \\ x_2(k) \\ x_3(k) \end{bmatrix}=\begin{bmatrix} i_L(k)-i_{ref}(k) \\ v_o(k) \\ \sum_1^k x_1+\sum_1^k x_2 \end{bmatrix}$$

here i_{Ref} represents the instantaneous reference inductor current and is generated from the following PI controller:

$$i_{ref}(k)=k_P v_o(k)+k_I \sum_{j=1}^{k} v_o(j) \tag{5.20}$$

Define the sliding surface as

$$s(k)=c_1x_1(k)+c_2x_2(k)+c_3x_3(k) \tag{5.21}$$

Suppose that $i_o \leq \rho$ at all times, where ρ represents the maximum disturbance from the load. Using the equivalent control $s(k+1) = s(k)$ at the sliding stage, the equivalent control can be obtained from Eqs. (5.19), (5.20), and (5.21), and is written as follows through replacing $x(k)$ by $\hat{x}(k)$ in Eq. (5.18):

$$d_{eq}=-(MB_d)^{-1}\left[(MA_d-N)\hat{x}(k)+ME_1v_g+ME_2\rho-c_3i_{Ref}(k)\right] \tag{5.22}$$

where

$$M=\begin{bmatrix} c_1+c_3 & -(k_P+k_I)(c_1+c_3)+c_2+c_3 \end{bmatrix}$$

$$N=\begin{bmatrix} c_1 & -k_P(c_1+c_3)+c_2 \end{bmatrix}$$

The actual trajectory of a sliding mode controlled system is shown in Fig. 5.3. The equivalent control term in Eq. (5.22) forces the system states to move toward the origin at the sliding stage. A switching control term should also be used to bring the system states onto the sliding surface s and trap them into a small range of s at the sliding stage. Although a sign function can ideally realize sliding mode control, the chattering problem will also appear [80]. In fact, only quasi-sliding mode control is feasible in practical applications. Therefore, the switching control term in Eq. (5.23), which is a saturation function, is adopted to eliminate the chattering at the steady stage.

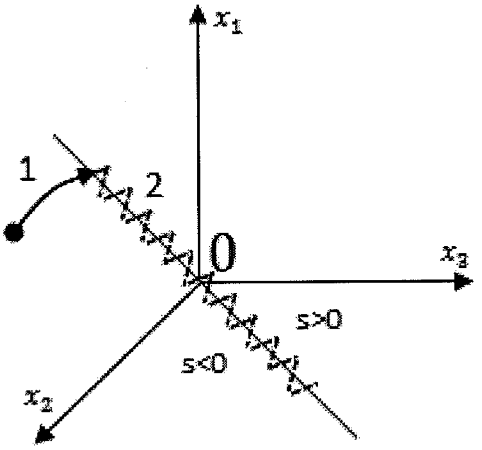

Fig. 5.3 Trajectory of a sliding mode controlled system.

$$d_{sw}(k) = -\beta sat(\frac{s}{\Delta}) = \begin{cases} -\beta & s > \Delta \\ -\frac{\beta}{\Delta}s & |s| \le \Delta \\ \beta & s < \Delta \end{cases} \tag{5.23}$$

where Δ represents the boundary layer around the sliding surface s. The overall discrete sliding mode controller is written as follows:

$$d(k) = d_{eq} + d_{sw} \tag{5.24}$$

The derivation of the stability conditions of the discrete sliding mode controller in Eq. (5.24) is given in [23] [79]. The parameter determination of the sliding mode controller is also presented in [79], and an empirical approach to selecting the sliding coefficients is presented in [23].

5.4 Simulations and Experiments

To verify the improved dynamic performance by the proposed SMO-based sensorless control, a boost converter whose parameters are listed in Table 2.1 is used.

5.4.1 Simulations of SMO-based and LO-based sensorless sliding mode control

Substituting the parameters in Table 2.1 into Eq. (5.14), the discrete counterpart in Eq. (5.16) is obtained as follows:

$$A_d = \begin{bmatrix} 0.9938 & -0.0660 \\ 0.0031 & 0.9996 \end{bmatrix},\ B_d = \begin{bmatrix} 2.9965 \\ -0.0067 \end{bmatrix},\ E_d = \begin{bmatrix} 0.1414 & 0.0002 \\ 0.0002 & -0.0067 \end{bmatrix}$$

Referring to [23] [79], the sliding mode controller in Eq. (5.24) is obtained as

$$d(k) = \frac{-7.59\hat{i}_L(k) - 3.45\hat{v}_o(k) - 5.07v_g + 5.8i_{ref}(k) + 3.43 - 5sat(\frac{s(k)}{0.1})}{100} \tag{5.25}$$

where

$$s(k) = 0.5x_1(k) + 5x_2(k) + 0.1x_3(k)$$

$$i_{ref}(k) = -10.016v_o(k) - 0.0053\sum_{j=1}^{k} v_o(j)$$

and $\hat{i}_L$ and $\hat{v}_o$ are the estimated states obtained by the SMO in Eq. (5.18).

Firstly, determine the parameter G_l in Eq. (5.18). Setting $Q = I_2$ and $\alpha = 1$, where I_2 is a unit matrix, the matrix P in Eq. (5.12) is obtained as

$$P = \begin{bmatrix} 76.6166 & 0.3167 \\ 0.3167 & 1.6196 \end{bmatrix}$$

Substituting the above P into Eq. (5.13), the matrix G_l in Eq. (5.18) is obtained as $G_l = [0.0793 \quad 0.6184]^T$, and the eigenvalues of $\Phi - G_lC$ are 0.9931 and 0.3820.

Secondly, determine the parameter G_n in Eq. (5.18). Substituting Eq. (5.11) into Eq. (5.10), it is found that the eigenvalues of $(I-G_n(CG_n)^{-1}C)\Phi$ are 0.9939 and 0. Therefore, there exists a real number η such that the sliding motion given by Eq. (5.10) is stable and will not be affected by any disturbance. Selecting η = 0.8, the matrix G_n is obtained as $G_n = [0.0003 \;\; -0.0083]^T$. Then, the SMO in Eq. (5.18) is given by

$$x(k+1)=\begin{bmatrix}0.9938 & -0.0660\\ 0.0031 & 0.9996\end{bmatrix}x(k)+\begin{bmatrix}2.9965 & 0.1414\\ -0.0067 & 0.0002\end{bmatrix}u(k)+\begin{bmatrix}0.0793\\ 0.6184\end{bmatrix}e_y(k)$$
$$+\begin{bmatrix}0.0003\\ -0.0083\end{bmatrix}v(k) \tag{5.26}$$

where $x(k+1) = [\hat{\imath}_L(k+1) \qquad \hat{v}_o(k+1)]^T$.

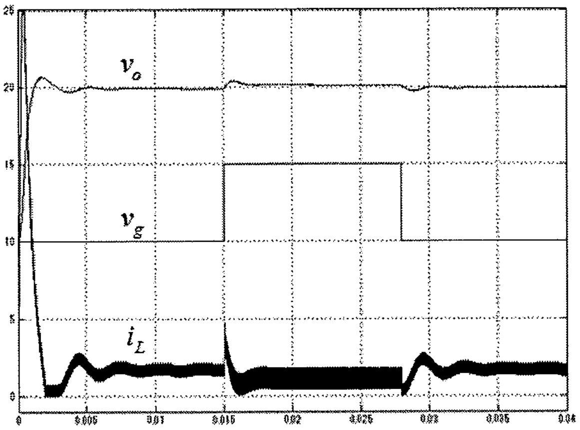

(a) Dynamic response to an input voltage disturbance

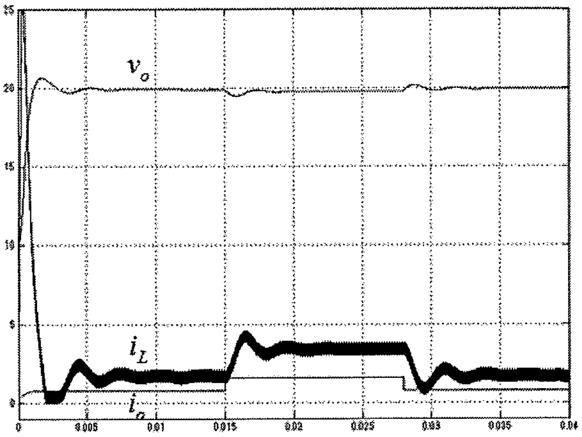

(b) Dynamic response to a load disturbance

Fig. 5.4 Dynamic response of SMO-based sliding mode control.

Similarly, α in Eq. (5.12) and η in Eq. (5.11) can be set to other values, e.g., $\alpha = 0.1$, $\alpha = 5$ and $\eta = 0.2$, to investigate the convergence performance of the SMO. Simulations show that good convergence performance is maintained by $\alpha = 1$ and $\eta = 0.8$. The dynamic response of the boost converter whose parameters are listed in Table 2.1 controlled by the sliding mode controller in Eq. (5.25) and the SMO in Eq. (5.26) is shown in Fig. 5.4.

For the LO in Eq. (5.1), the estimation error dynamics are governed by the eigenvalues of the matrix Φ–KC. The eigenvalue assignment of Φ–KC is usually used to determine the parameter K, and eigenvalues with a large real part and small imaginary part will result in better performance, while those with a small real part and large imaginary part will result in poorer performance. Simulations show that good convergence performance is maintained by the eigenvalues of Φ–KC of $\{0.8 \pm j0.2\}$ and the LO is given in Eq. (5.27). The dynamic response of the boost converter with the parameters listed in Table 2.1 controlled by the sliding mode controller in Eq. (5.25) and the LO in Eq. (5.27) is shown in Fig. 5.5.

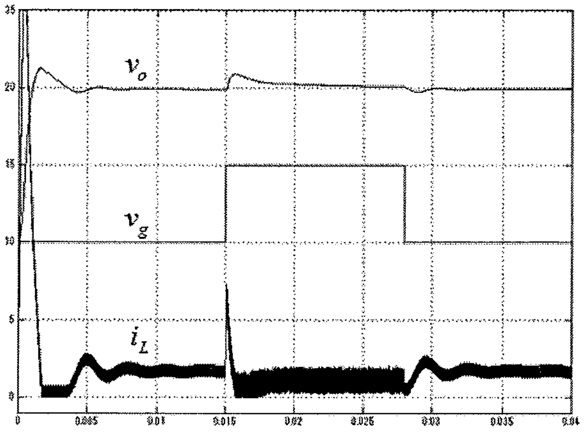

(a) Dynamic response to an input voltage disturbance

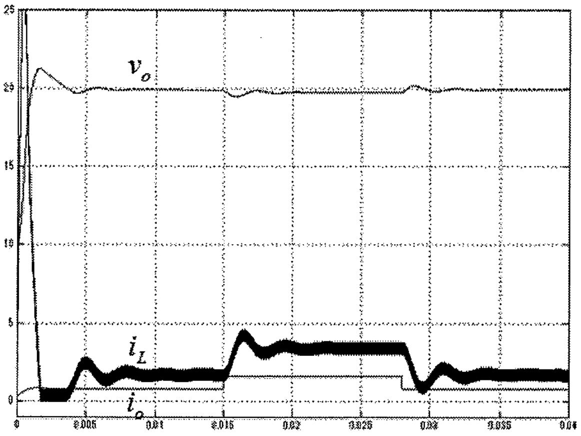

(b) Dynamic response to a load disturbance

Fig. 5.5 Dynamic response of LO-based sliding mode control.

$$x(k+1)=\begin{bmatrix}0.9938 & -0.0660\\ 0.0031 & 0.9996\end{bmatrix}x(k)+\begin{bmatrix}2.9965 & 0.1414\\ -0.0067 & 0.0002\end{bmatrix}u(k)+\begin{bmatrix}24.9529\\ 0.3934\end{bmatrix}e_y(k) \quad (5.27)$$

where $x(k+1) = [\hat{i}_L(k+1) \quad \hat{v}_o(k+1)]^T$.

From the above simulations, it can be observed that the dynamic response of the boost converter whose parameters are listed in Table 2.1 is clearly improved by SMO-based sensorless sliding mode control compared with LO-based control when the input voltage is disturbed. Figures. 5.4(b) and 5.5(b) show that the dynamic response is very short when the load is disturbed, so that the improvement in the dynamic response is relatively slight when the load is disturbed.

5.4.2 Practical experiments of LO- and SMO-based sliding mode control

The practical environment is the same as shown in Fig. 3.10 in chapter 3: a 16 bit digital signal processor NJU20010 produced by NJRC is used to execute the controllers; the limit of the duty ratio is set to 0.05 ~ 0.88; The slew rates of the load current and the input voltage are 250 mA/μs and 2.0 V/μs, respectively. The dynamic responses of the boost converter controlled by the sliding mode controller in Eq. (5.25) with the SMO in Eq. (5.26) and the LO in Eq. (5.27) are shown in Figs. 5.6 and 5.7, respectively. It can be seen that the overshoot/undershoot and the recovery time are clearly improved when the input voltage is disturbed by the SMO-based control. Also, since the dynamic response to the load disturbance is very short, the dynamic response improvement is relatively slight.

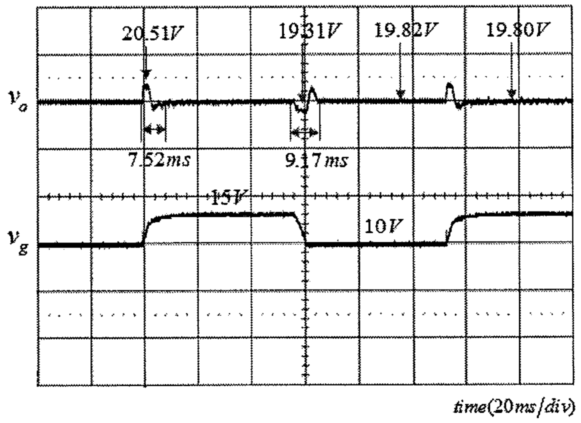

(a) Dynamic response to an input voltage disturbance

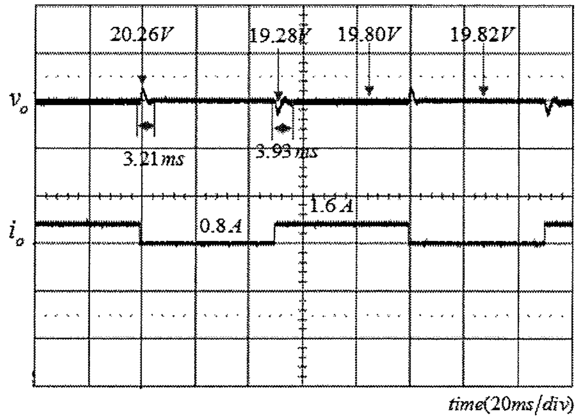

(b) Dynamic response to a load disturbance

Fig. 5.6 Experimental results of SMO-based sliding mode control.

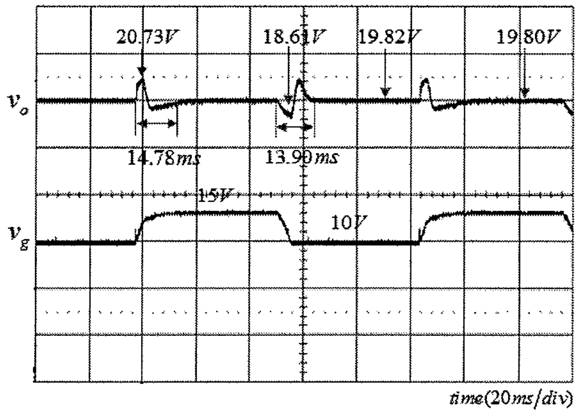

(a) Dynamic response to an input voltage disturbance

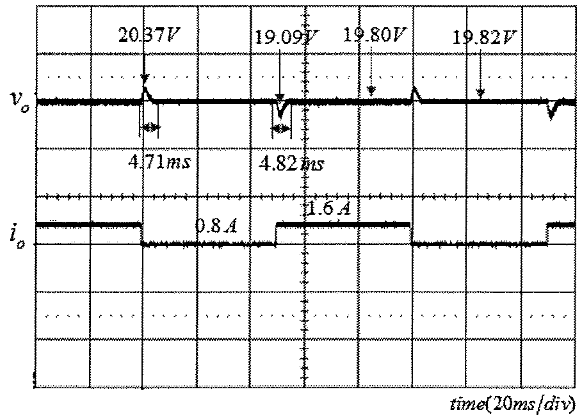

(b) Dynamic response to a load disturbance

Fig. 5.7 Experimental results of LO-based sliding mode control.

5.4.3 Comparison with multi-loop PI control

To compare the dynamic performance of the boost converter whose parameters are listed in Table 2.1 by SMO-based sliding mode control and conventional sensor-based multi-loop PI control, a multi-loop control given in Eqs. (5.28) and (5.29), is adopted, in which the inductor current is sensed by a shunt resistor. The counterpart of the Eqs. (5.28) and (5.29) in continuous time shows that the inner open loop has a gain crossover frequency of 40.8 kHz with a phase margin of 86.2^0, and the outer open loop has a gain crossover frequency of 2.47 kHz with a phase margin of 79.8^0 and a gain margin of 18.0 dB. It can be said that the multi-loop controller is very good. Figure. 5.8 shows its dynamic response.

$$d(k) = -2.156e_I(k) - 0.00067\Sigma e_I(j) \tag{5.28}$$

$$i_{ref}(k) = -10.016v_0(k) - 0.0053\Sigma v_0(j) \tag{5.29}$$

where $e_I(k) = i_L(k) - i_{ref}(k)$, i_L is the inductor current, and i_{ref} is the reference current.

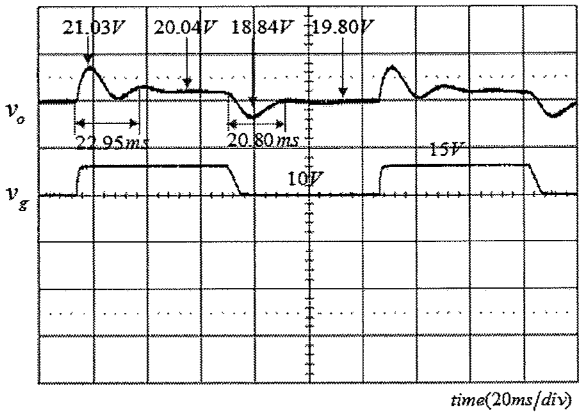

(a) Dynamic response to an input voltage disturbance

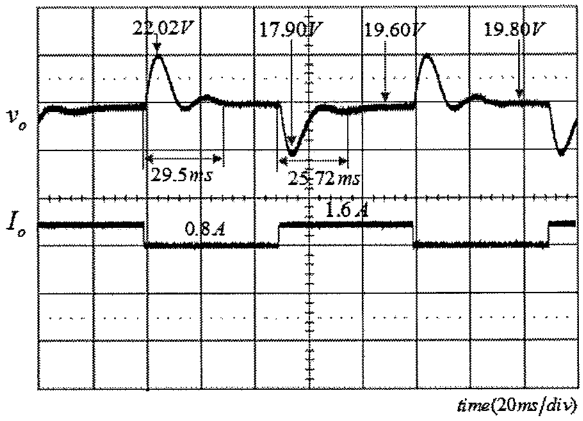

(b) Dynamic response to a load disturbance

Fig. 5.8 Experimental results of sensor-based multi-loop PI control.

5.5 Conclusions

A state observer can be used to estimate the inductor current instead of a current sampling network. For an LO, the output estimation error is linearly fed back to the observer, while for an SMO, the output estimation error is fed back to the observer via a nonlinear term so that better convergence performance can be maintained. Applying the proposed discrete SMO based sensorless control to a boost converter, simulations and experiments show that the dynamic response are greatly improved by the SMO-based sensorless control, compared with the LO-based sensorless control.

6

Conclusions and Future Works

6.1 Conclusions

In this research, the current sensorless control of boost converters is studied, and the achievements are as follows:

- **Single-loop control and multi-loop control are compared in chapter 2**
  Based on the small signal model, the single-loop PID control and multi-loop PI control of the boost converter is compared. It clearly shows that multi-loop control can improve the closed-loop dynamic performance.
- **An LO-based sensorless multi-loop control is analyzed in chapter 3**
  The design of a LO based sensorless multi-loop control of boost converters is proposed: the closed-loop stability evaluation and the closed-loop dynamic characteristics evaluations of output voltage, inductor current as well as the estimated inductor current are provided. Simulations show the design procedure. Practical experiments show the practical dynamic performance.
- **Robust H∞ synthesis approaches are proposed to design compact sensorless controllers in chapter 4**
  The LO-based sensorless multi-loop control needs a complicated trail-and-error design procedure. There are at least 6 parameters to be determined. A compact sensorless controller for a boost converter is deduced by a novel robust H∞ synthesis approach. Simulations show the straightforward closed-loop characteristics evaluation: there is only one parameter to be tuned. The practical experiments show that good dynamic

responses are maintained.

A low order controller has the merit of small computation volume or simple circuit. A novel robust H∞ approach is also proposed to design a low-order sensorless controller for boost converters. Simulations show the closed-loop evaluation. Practical dynamic responses show that good dynamic performance is maintained.

- **A sliding mode observer (SMO) is proposed in chapter 5**

  An SMO feeds the output estimation error back to the observer via a nonlinear term with a better convergence performance. A discrete SMO is proposed to the sensorless control of a boost converter. Simulations and practical experiments show that the dynamic responses are greatly improved compared with LO-based sensorless control.

6.2 Future works

1. Verify the accuracy improvement of output voltage for the robust H∞ control of boost converters

One of the controllers derived from the proposed robust H∞ approaches for the boost converter with parameters listed in Table 2.1 is rewritten in Eq. (6.1).

$$\begin{cases} \dot{p}(t) = \begin{bmatrix} -\dfrac{1.0967}{\varepsilon} & 9938.5-\dfrac{25.4108}{\varepsilon} \\ 506.7877+\dfrac{0.0042}{\varepsilon} & 11326-\dfrac{0.9034}{\varepsilon} \end{bmatrix} p(t) + \begin{bmatrix} 21277 & -9938.5 \\ 0 & -40+\dfrac{1}{\varepsilon} \end{bmatrix} \begin{bmatrix} \hat{v}_g(t) \\ \hat{v}_o(t) \end{bmatrix} \\ \hat{d}(t) = \begin{bmatrix} 0.0020-\dfrac{2.4326}{10^6\varepsilon} & 0.0220-\dfrac{5.6364}{10^5\varepsilon} \end{bmatrix} p(t) \end{cases} \tag{6.1}$$

It can be seen that the input voltage and output voltage are used in the controller, while the integral of output voltage is not used. In future works, the following signals which includes the integral of output voltage will be used to design the controllers and verify the accuracy improvement of output voltage.

$$\hat{v}_g,\ \hat{v}_o,\ \int \hat{v}_o dt$$

2. Study and compare H_2 control with H∞ control.

As defined in Eq. (6.2), the H∞ norm examines the maximum value over all frequencies.

$$\left\|G_{cl}(s)\right\|_{\infty} = \sup_{\omega\in[0,\infty]} \sigma_{\max}[G_{cl}(j\omega)] = \sup_{\left\|w\right\|_2=1} \frac{\left\|z\right\|_2}{\left\|w\right\|_2} \tag{6.2}$$

The H_2 norm of a scalar function is defined in Eq. (6.3), which examines the summary of the absolute value.

$$\left\|G_{cl}(s)\right\|_2 = \left[\frac{1}{2\pi}\int_{-\infty}^{+\infty} |G(j\omega)|^2\, d\omega\right]^{\frac{1}{2}} \tag{6.3}$$

Whether there are some merits using the $H_2/H\infty$ control to design a controller for switching converters will be studied in future.

References

[1] C. Simpson, "Linear and switching voltage regulator fundamentals". National semiconductor, 2011.

[2] R. W. Erickson, D. Maksimovic, Fundamentals of Power Electronics. Kluwer Academic Publishers, 2001.

[3] J. D. van Wyk, F. C. Lee, "On a future for power electronics". IEEE Jour. of Emer. and Sele. Topi. in Power Elec., Vol. 1, No. 2, pp. 59-72, 2013.

[4] J.W. Kolar, J. Biela, S. Waffler, T. Friedli, U. Badstuebner, "Performance trends and limitations of power electronic systems". 6th Inter. Conf. on Integ. Power Elec. Systems, pp. 1-20, Mar. 2010.

[5] M. M. Jovanovic, "Power supply technology - past, present and future". Proc. of the Power Conv. and Inte. Motion Conf., pp. 3-15, Mar. 2007.

[6] P. Shamsi, B. Fahimi, "Design and development of very high frequency resonant DC–DC boost converters". IEEE Trans. on Power Elec., Vol. 27, No. 8, pp. 3725-3733, 2012.

[7] C. N. P.P. Robert, D. S. Anthony, M. R. Juan, I. A. David, J. P. David, "Very high frequency resonant boost converters". IEEE Power Elec. Spec. Conf., pp. 2718-2724, June, 2007.

[8] J. Liu, K. L. Wong, S. Allen, J. Mookken, "Performance evaluations of hard-switching interleaved DC/DC boost converter with new generation silicon carbide MOSFETs". Cree Inc., SiC Appl. Engineering, Durham, NC, USA.

[9] P. Kumar, "DC-DC converters applications and design trends". Electronics Maker, 2013.

[10] K.R. Skup, P. Grudzinski, P. Orleanski, W. Nowosielski, "A digital controller for satellite medium power DC/DC converters". 18th Inter. Conf. on Meth. and Mode. in Auto. and Robo. (MMAR), pp. 566-571, Aug. 2013.

[11] A. Trejos, M. Goez, C. A. Ramos-Paja, E. Arango, "Digital controllers design analysis for DC/DC converters in PV applications". 2013 4th IEEE Inter. Symp. on Power Elec. for Distr. Gene. Syst. (PEDG), pp. 1-6, July 2013.

[12] S. Khare, "Features, value and benefits of digital control for power supplies". Microchip Technology Inc., 2010.

[13] Taufik, M. Starman, M. Anwari, “Digitally controlled synchronous buck converter”. Proc. of the Inter. Conf. on Elec. Engi. and Info. Inst. Tech., pp. 911-914, June, 2007.

[14] H.P. Forghani-zadeh, G.A. Rincon-Mora, “Current-sensing techniques for DC-DC converters”. Midwest Symp. on Circ. and Syst., Vol. 2, pp. 577-580, Aug. 2002.

[15] A. Saysanasongkham, M. Arai, S. Fukumoto, S. Takeuchi, K. Wada, “A highly reliable digital current control using an adaptive sampling method”. IEEJ Jour. of Indus. Appl., Vol. 3, No. 4, pp. 296-303, 2014.

[16] P. Midya, P. T. Krein, M. F. Greuel, “Sensorless current mode control–an observer-based technique for DC–DC converters”. IEEE Trans. on Power Elec., Vol. 16, No.4, pp 522-526, 2001.

[17] G. Cimini G, G. Ippoliti, G. Orlando, M. Pirro, “Current sensorless solution for PFC boost converter operating both in DCM and CCM”. 21st Medi. Conf. on Cont. and Auto., pp.137-142, June 2013.

[18] A.G. Beccuti, S. Mariethoz, S. Cliquennois, S. Wang, M. Morari, “Explicit model predictive control of DC–DC switched-mode power supplies with extended Kalman filtering”. IEEE Trans. on Indus. Elec., Vol. 56, No. 6, pp 1864-18740, 2009.

[19] I. Lee, G.W. Moon, “Soft-switching DC/DC converter with a full ZVS range and reduced output filter for high-voltage applications”. IEEE Trans. on Power Elec., Vol. 28, No. 1, pp. 112-122, 2013.

[20] J. Biela, M. Schweizer, S. Waffler, J. W. Kolar, “SiC versus Si–evaluation of potentials for performance improvement of inverter and DC–DC converter systems by SiC power semiconductors”. IEEE Trans. on Indus. Elec., Vol. 58, No. 7, pp. 2872-2882, 2011.

[21] S. Ujita, Y. Kinoshita, H. Umeda, T. Morita, “A compact GaN-based DC-DC converter IC with high-speed gate drivers enabling high efficiencies”. IEEE 26th Intern. Symp. on Power Semi. Devices & IC’s (ISPSD), pp. 51-54, June 2014.

[22] Xutao Li, Minjie Chen, S. Hirofumi, T. Yoshihara, “Design of an auto-tunable PID controller for buck converters through a robust H∞ synthesis approach”. IEICE Comm. Expr., pp. 7-12, Jan. 2016.

[23] S.-C. Tan, Y.M. Lai, C. K. Tse, L. Martinez-Salamero, C.-K. Wu, “A fast-response sliding-mode controller for boost-type converters with a wide range of operating conditions”. IEEE trans. Indus. Elect., Vol. 54, No. 6, pp. 3276-3286, 2007.

[24] A. A. Johnson, J. Vaidhyanathan, C. Arkhom, “Synthesis of nonlinear control of switching topologies of buck-boost converter using fuzzy logic on field programmable gate array (FPGA)”. Jour. of Intel. Lear. Syst. and Appl., pp.36-42, 2010.

[25] C.-Y. Chan, “A nonlinear control for DC–DC power converters”. IEEE Trans. on Power Elec., Vol. 22, No. 1, pp. 216-222, 2007.

[26] K. K. Tse, H. S.H. Chung, S. Y. R. Hui, H. C. So, “A comparative investigation on the use of random modulation schemes for DC/DC converters”. IEEE Trans. on Indus. Elec., Vol. 47, No. 2, 2000.

[27] H. Chung, S.Y.R. Hui, K.K. Tse, “A chaotic soft switching PWM boost converter for EMI reduction”. IEEE Intern. Symp. on Indus. Elec., pp. 341-346, July 2008.

[28] B. Ankit, P. David, W. K. Keong, C. Federico, L. W. Cheng, "DC-DC buck converter EMI reduction using PCB layout modification". IEEE Trans. on Elec. Comp., Vol. 53, No. 3, 2011.

[29] K. A. Mohammed, F. H. Khan, "Reliability analysis and performance degradation of a boost converter". IEEE Trans. on Indus. Appl., Vol. 50, No. 6, pp. 3986-3994, Nov. 2014.

[30] G. Chen, R. Burgos, Z. Liang, F. Lacaux, F. Wang, J.D. van Wyk, W.G. Odendaal, D. Boroyevich, "Reliability-oriented design considerations for high-power converter modules". 35fh Ann. IEEE Power Elec. Spec. Conf., Vol.1, pp.419-425, June 2004.

[31] Y. Hayashi, A. Matsumoto, "Fundamental study of an intelligent power routing switch based on SiC DC-DC converter for next generation DC distribution network". 15th Euro. Conf. on Power Elec. and Appl. (EPE), pp. 1-8, Sep. 2013.

[32] B. Brad, K. K. Marian, "Modeling the closed-current loop of PWM boost DC–DC converters operating in CCM with peak current-mode control". IEEE Trans. on circ. and syst.–I: Regular papers, Vol. 52, No. 11, pp. 2404-2412, 2005.

[33] R.D. Middlebrook, S. Cuk, "A general unified approach to modelling switching converter power stages". IEEE Power Elec. Spec. Conf., pp. 18-34, 1976.

[34] R. B. Ridley, B. H. Cho, F. C. Y. LEE, "An analysis and interpretation of loop gains of multi-loop controlled switching regulators". IEEE Trans. on Power Elec., pp. 489-498, 1988.

[35] A. F. Rozman, J. J. Boylan, "Band pass current control". Appl. Power Elec. Conf. and Expo., Vol. 2, pp. 631-637, 1994.

[36] A.A. Stoorvogel, "The H∞ control problem: a state space approach". Prentice Hall, Englewood Cliffs, 1992.

[37] K. D. Young, V. I. Utkin, U. Ozguner, "A control engineer's guide to sliding mode control". Trans. on Contr. Syst. Tech., Vol. 7, No. 3, pp. 328-342, 1999.

[38] R. Ahmadi, D. Paschedag, M. Ferdowsi, "Closed-loop input and output impedances of DC-DC switching converters operating in voltage and current mode control". IEEE Indus. Elec. Soci., pp. 2311-2316, Nov. 2010.

[39] H. Choi, "Practical feedback loop design considerations for switched mode power supplies". Fairchild Semiconductor Power Seminar, pp. 489-498, 2010-2011.

[40] N. Kondrath, M. K. Kazimierczuk, "Audio-susceptibility of the inner-loop of peak current-mode controlled PWM DC-DC buck converter in CCM". Ann. Conf. on IEEE Indus. Elec. Soci., pp. 250-255, Oct. 2012.

[41] Z. Chen, "Double loop control of buck-boost converters for wide range of load resistance and reference voltage". IET Contr. Theo. and Appl., Vol. 6, No. 7, pp. 900-910, 2012.

[42] D. G. Luenberger, "An introduction to observers". IEEE Trans. on Auto. Cont., Vol. 16, No. 6, pp 596–602, 1971.

[43] H. Cho, S. J. Yoo, S. Kwak, "State observer based sensorless control using Lyapunov's method for boost converters". IET Power Elec., Vol. 8, No. 1, pp 11-19, 2014.

[44] Xutao Li, Minjie Chen, Shinohara Hirofumi, and Yoshihara Tsutomu, "Design of a Luenberger observer based sensorless multi-loop control for boost converters". Inter. Conf. on Elec., Infor. and Comm., Jan., 2016

[45] M. K. Kazimierczuk, Pulse-width modulated DC–DC power converters. John Wiley & Sons, Ltd, 2008.

[46] E. Vidal-Idiarte, L. Martinez-Salamero, H. Valderrama-Blavi, F. Guinjoan, J. Maixe, "Analysis and design of H∞ control of nonminimum phase-switching converters". IEEE Trans. on Circ. and Syst., Vol. 50, No. 10, pp. 1316-1323, 2003.

[47] R. Naim, G. Weiss, S. Ben-Yaakov, "H∞ control applied to boost power converters". IEEE Trans. on Power Elec., Vol. 2, No. 4, pp. 677-683, 2003.

[48] C. Olalla, R. Leyva, A. El Aroudi, P. Garces, I. Queinnec, "LMI robust control design for boost PWM converters". IET Power Elec., Vol. 3, No.1, pp 75-85, 2010.

[49] Xutao Li, Minjie Chen, Shinohara Hirofumi, and Yoshihara Tsutomu, "Design of a sensorless controller synthesized by robust H∞ control for boost converters". IEICE Trans. on Comm., Vol. E99-B, No. 02, 8 pages, Feb., 2016. (to appear)

[50] C. B. Martin, "Introduction to a special coordinate basis for multivariable linear systems". Proc. of the Amer. Cont. Conf., Vol. 145, No. 2, pp 204-210, Mar. 1998.

[51] B.M. Chen, Robust and H∞ control. Springer, 2010.

[52] A. Saberi, B.M. Chen, Z.L. Lin, "Closed-form solutions to a class of H-optimization problems – output feedback case". Proc. of the 31st Conf. on Deci. and Cont., Vol. 2, pp 2261-2262, Dec., 1992.

[53] A. Saberi, B.M. Chen, "Closed-form solutions to a class of H-∞ optimization problems – output feedback case". Inter. Jour. of Cont., Vol. 60, No. 1, pp 41-70, 1994.

[54] B.M. Chen, A. Saberi, U.-L. Ly, "A non-iterative method for computing the infimum in H∞-optimization". Inter. Jour. of Cont., Vol. 56, No. 6, pp 1399-1418, 1992.

[55] C. Scherer, "H∞-control by state-feedback and fast algorithms for the computation of optimal H∞-norms". IEEE Trans. on Auto. Cont., Vol. 35, No. 10, pp 1090-1099, 1990.

[56] A. Moran, M. Hayase, "Design of reduced order H∞ controllers". The 36th SICE Ann. Conf., pp 1013-1018, July 1997.

[57] C. F. Yung, "Reduced-order H∞ controller design: An algebraic Riccati equation approach". Automatica, Vol.36, pp. 923-926, 2000.

[58] Y. Jie, A. Sideris, "H∞ control synthesis via reduced order LMIs". The 36th Conf. on Deci. & Cont., Vol. 1, pp 183-188, Dec. 1997.

[59] P. Gahinet, "Explicit controller formulas for LMI-based H∞ synthesis". American Contr. Conf., Vol. 3, pp 2396-2400, July 1994.

[60] Xutao Li, Minjie Chen, Shinohara Hirofumi, and Yoshihara Tsutomu, "Design of a low order sensorless controller by robust H∞ control for boost converters". Journal of Power Electronics, Vol. 16, No. 2, 12 pages, March, 2016. (to appear)

[61] A. Saberi, B.M. Chen, Z.L. Lin, "Closed-form solutions to a class of H∞-optimization problems". Inter. Jour. of Cont., Vol. 60, No. 1, pp 41-70, 1994.

[62] A.A. Stoorvogel, A. Saberi, B.M. Chen, "A reduced order observer based controller design for H∞-optimization". IEEE Trans. on Auto. Contr., Vol. 39, No. 2, pp 355-360, 1994.

[63] H. Sira-Ramirez, "Sliding motions in bilinear switched networks". IEEE Trans. Circ. Syst., Vol. CAS-34, No. 8, pp. 919-933, 1987.

[64] J. T. Mossoba, P. T. Krein, "Design and control of sensorless current mode dc-dc converters". Applied Power Electronics Conference and Exposition, Vol. 1, pp. 315-321, Feb. 2003.

[65] A. Kelly, K. Rinne, "Sensorless current-mode control of a digital dead-beat DC-DC converter". Applied Power Electronics Conference and Exposition, Vol. 3, pp. 1790-1795, 2004.

[66] Q. Tong, Q. Zhang, R. Min, X. Zou, Z. Liu, Z. Chen, "Sensorless predictive peak current control for boost converter using comprehensive compensation strategy". IEEE Trans. Indus. Elect., pp. 1-11, 2013.

[67] Y. C. Zhang, Z. M. Zhao, T. Lu, L. Q. Yuan, W. Xu, J. G. Zhu, "A comparative study of Luenberger observer, sliding mode observer and extended Kalman filter for sensorless vector control of induction motor drives". Energy Conv. Cong. and Expo., pp. 2466-2473, 2009.

[68] A. J. Koshkouei, A. S. I. Zinober, "Sliding mode state observers for discrete-time linear systems". Inter. Jour. of Syst. Scie., Vol. 33, No. 9, pp. 751-758, 2002.

[69] S. K. Spurgeona, "Sliding mode observers: a survey". Inter. Jour. of Syst. Scie., Vol. 39, No. 8, pp. 751-764, 2008.

[70] H. J. Yang, Y.Q. Xia, P. Shi, "Observer-based sliding mode control for a class of discrete systems via delta operator approach". Journal of the Franklin Institute, Vol. 347, No. 7, pp. 1199-1213, 2010.

[71] I. Haskara, "On sliding mode observers via equivalent control approach". Inter. Journal of Control, Vol. 71, No. 6, pp. 1051-1067, 2010.

[72] Y. Shtessel, C. Edwards, L. Fridman, Sliding mode control and observation. Birkhauser, 2013.

[73] A. Sainana, "A novel sliding mode observer applied to the three-phase voltage source inverter". European Conf. on Power Elec. and Appl., pp. 1-12, Sept. 2005.

[74] F.M. Oettmeier, J. Neely, S. Pekarek, R. DeCarlo, K. Uthaichana, "MPC of switching in a boost converter using a hybrid state model with a sliding mode observer". IEEE trans. Indus. Elect., Vol. 56, No. 9, pp. 3453-3466, 2009.

[75] A. Jaafar, E. Godoy, P. Lefranc, X.F. Lin-Shi, A. Fayaz, N. Li, "Nonlinear sliding mode observer and control of high order DC-DC converters". Annual Conf. on IEEE Indus. Elec. Soci., pp. 180-186, Nov. 2010.

[76] G. Cimini, G. Ippoliti, G. Orlando, M. Pirro, "Current sensorless solutions for PFC of boost converters with passivity-based and sliding mode control". Power Engi., Ener. and Elec. Drives, pp 1175-1180, May, 2013.

[77] Xutao Li, Minjie Chen, and Tsutomu Yoshihara, "Design of sliding-mode-observer-based sensorless control of boost converters for high dynamic performance". Journal of Signal Processing, Vol. 19, No. 6, pp. 253-261, Nov. 2015.

[78] H. H. Choi, K.-S. Ro, "LMI-based sliding-mode observer design method". Proc. Inst. Elect. Eng. Contr. Theory Appl., Vol. 152, pp. 113-115, 2005.

[79] A. J. Koshkouei, A. S. I. Zinober, "Sliding mode control of discrete-time systems". Jour. of Dyna. Syst., Meas., and Contr., Vol. 122, pp. 793-802, 2000.

[80] V. Utkin, H. Lee, "Chattering problem in sliding mode control systems". International Workshop on Variable Structure Systems, pp. 346-350, June 2006.

Publications

Journal Papers

1. Xutao Li, Minjie Chen, Hirofumi Shinohara, and Tsutomu Yoshihara, “Design of a Low Order Sensorless Controller by Robust H∞ Control for Boost Converters”. Journal of Power Electronics, Vol. 16, 12 pages, 2016. (to appear)
2. Xutao Li, Minjie Chen, Hirofumi Shinohara, and Tsutomu Yoshihara, “Design of a Sensorless Controller Synthesized by Robust H∞ Control for Boost Converters”. IEICE Transactions on Communications, Vol. E99-B, No. 02, pp. 356-363, Feb., 2016.
3. Xutao Li, Minjie Chen, Hirofumi Shinohara, and Tsutomu Yoshihara, “Design of an Auto-Tunable PID Controller for Buck Converters through a Robust H∞ Synthesis Approach”. IEICE Communication Express, Vol. 5, No. 1, pp. 7-12, Jan., 2016.
4. Xutao Li, Minjie Chen, and Tsutomu Yoshihara, “Design of Sliding-Mode-Observer-Based Sensorless Control of Boost Converters for High Dynamic Performance”. Journal of Signal Processing, Vol. 19, No. 6, pp. 253-261, Nov. 2015.
5. Minjie Chen, Xutao Li, Hao Zhang, Tsutomu Yoshihara, “A Novel Soft-Switching Modular Inverter for Photovoltaic PCU with High Efficiency and Reduced Size”. IEEJ Transactions on Electronics, Information and Systems, Vol. 134, No. 11, pp. 1647-1655, 2014.

Conference Papers

1. Xutao Li, Minjie Chen, Hirofumi Shinohara, and Tsutomu Yoshihara, “Design of a Luenberger Observer Based Sensorless Multi-loop Control for Boost Converters”. International Conference on Electronics, Information and Communication, pp. 258-261,

Jan., 2016.

2. Xutao Li, Minjie Chen, Hirofumi Shinohara, and Tsutomu Yoshihara, "Dynamic Response Improvement of Feedforward Combined Multi-loop Control for Boost Converters". International Technical Conference on Circuits Systems, Computers and Communications, pp. 529-532, June, 2015.
3. Xutao Li, Minjie Chen, Hao Zhang, and Tsutomu Yoshihara, "Dynamic Response Improvement of Discrete Sliding Mode Controlled Switching Power Converter via Double Integral". International conference on Instrumentation, Control, Information Technology and System Integration (SICE), pp. 1981-1986, Sept. 2013.
4. Xutao Li, Minjie Chen, and Tsutomu Yoshihara, "A Method of Searching PID Controller's Optimized Coefficients for Buck Converter Using Particle Swarm Optimization". IEEE 10th International Conference on Power Electronics and Drive Systems (PEDS), pp. 238-243, April, 2013.
5. Minjie Chen, Xutao Lee, and Tsutomu Yoshihara, "A Novel Soft-Switching Grid-Connected PV Inverter and its Implementation". IEEE 9th International Conference on Power Electronics and Drive Systems (PEDS), pp. 373-378, Dec., 2011.

Appendix

■ Special coordinate basis (SCB) decomposition

The system in Eq. (4.1) is rewritten as follows.

$$Converter:\begin{cases}\dot{x}=Ax+Bu+Ew\\ y=C_1x+D_1w\\ z=C_2x+D_2u\end{cases}\tag{A.1}$$

From the description in chapter 4, the state $x = [x_1 \quad x_2]$ can be written as follows:

$$\begin{aligned}\dot{x}_1&=a_{11}x_1+a_{12}x_2+b_1u\\ \dot{x}_2&=a_{21}x_1+a_{22}x_2+b_2u\end{aligned}\tag{A.2}$$

1. SCB decomposition of subsystem Σ_P

The subsystem Σ_P is written as follows:

$$\Sigma_P:\begin{cases}\dot{x}=Ax+Bu\\ z=C_2x+D_2u\end{cases}\tag{A.3}$$

As presented in chapter 4, matrix $D_2 = 0$. The SCB decomposition procedure is as follows:
Step 1: differentiate z;

$$\dot{z}=C_2Ax+C_2Bu\tag{A.4}$$

As $C_2B \neq 0$, select the following matrix to transform the subsystem in Eq. (A.3):

$$T = \begin{bmatrix} 1 & 0 \\ 0 & w_o \end{bmatrix} \tag{A.5}$$

Step 2: eliminate the u of x_2 in Eq. (A.2);

Define a temporary state $\hat{x} = [\hat{x}_1 \quad \hat{x}_2]$, and perform $\hat{x} = Tx$, then

$$\begin{aligned} \dot{\hat{x}}_1 &= a_{11}\hat{x}_1 + \frac{a_{12}}{w_o}\hat{x}_2 + b_1 u \\ \dot{\hat{x}}_2 &= w_o a_{21}\hat{x}_1 + a_{22}\hat{x}_2 + w_o b_2 u \end{aligned} \tag{A.6}$$

From the $\hat{x}_1$ in Eq. (A.6), u can be expressed as:

$$u = -\frac{a_{11}}{b_1}\hat{x}_1 - \frac{a_{12}}{w_o b_1}\hat{x}_2 + \frac{1}{b_1}\dot{\hat{x}}_1 \tag{A.7}$$

Substituting Eq. (A.7) into $\hat{x}_2$ in Eq. (A.6), $\hat{x}_2$ is written as:

$$\dot{\hat{x}}_2 = w_o\left(a_{21} - \frac{a_{11}b_2}{b_1}\right)\hat{x}_1 + \left(a_{22} - \frac{a_{12}b_2}{b_1}\right)\hat{x}_2 + w_o\frac{b_2}{b_1}\dot{\hat{x}}_1 \tag{A.8}$$

Step 3: eliminate the $\dot{\hat{x}}_1$ in Eq. (A.8);

Define a temporary state $x_* = [x_{1*} \quad x_{2*}]$, and let

$$\begin{aligned} x_{1_*} &= \hat{x}_1 \\ x_{2_*} &= \hat{x}_2 - w_o\frac{b_2}{b_1}\hat{x}_1 \end{aligned} \tag{A.9}$$

Then, from Eqs. (A.6), (A.8) and (A.9), x_* is expressed as follows:

$$\begin{aligned}\dot{x}_{1*} &= (a_{11}+\frac{a_{12}b_2}{b_1})x_{1*}+\frac{a_{12}}{w_o}x_{2*}+b_1u\\ \dot{x}_{2*} &= w_o[a_{21}+\frac{b_2}{b_1}(a_{22}-a_{11})-(\frac{b_2}{b_1})^2a_{12}]x_{1*}+(a_{22}-\frac{a_{12}b_2}{b_1})x_{2*}\end{aligned} \tag{A.10}$$

Step 4: construct the SCB of Eq. (A.3).

The SCB of Eq. (A.3) is written as follows:

$$\begin{cases}\dot{x}_* = A_*x_* + B_*u_*\\ z_* = C_{1*}x_*\end{cases} \tag{A.11}$$

where

$$A_* = \begin{bmatrix} a_{22}-\frac{a_{12}b_2}{b_1} & w_o[a_{21}+\frac{b_2}{b_1}(a_{22}-a_{11})-(\frac{b_2}{b_1})^2a_{12}] \\ \frac{a_{12}}{w_o} & a_{11}+\frac{a_{12}b_2}{b_1}\end{bmatrix},\quad B_* = \begin{bmatrix}0\\1\end{bmatrix}$$

$$C_{1*} = \begin{bmatrix} 1 & 0 \\ -\frac{w_ob_2}{b_1} & 1\end{bmatrix}$$

and

$$\Gamma_{sP} = \begin{bmatrix} 0 & 1 \\ \frac{1}{w_o} & \frac{b_2}{b_1}\end{bmatrix},\quad \Gamma_{oP} = \begin{bmatrix} 1 & 0 \\ \frac{w_ob_2}{b_1} & 1\end{bmatrix},\quad \Gamma_{iP} = \frac{1}{b_1}$$

2. SCB decomposition of subsystem Σ_Q

The subsystem Σ_Q is written as follows:

$$\Sigma_Q : \begin{cases}\dot{x} = A^Tx + C_1^Tu\\ y = E^Tx + D_1^Tu\end{cases} \tag{A.12}$$

The SCB decomposition procedure is as follows:

Step 1: define the transform matrix *T*;

As $D_1^T \neq 0$, select a unit transform matrix T as follows:

$$T = \begin{bmatrix} 1 & 0 \\ 0 & 1 \end{bmatrix} \tag{A.13}$$

Step 2: construct the SCB of Eq. (A.12).

Define a temporary state $x_* = [x_{1*} \quad x_{2*}]$. As T is a unit matrix, the SCB of Eq. (A.12) is constructed as follows:

$$\begin{cases} \dot{x}_* = A_*^T x_* + C_{1*}^T u_* \\ y_* = E_*^T x_* + D_{1*}^T u_* \end{cases} \tag{A.14}$$

where $A_* = A$, $C_{1*} = C_1$, $D_{1*} = D_1$, and

$$E_* = \begin{bmatrix} e_1 & 0 \\ 0 & 1 \end{bmatrix}$$

and

$$\Gamma_{sQ} = \begin{bmatrix} 1 & 0 \\ 0 & 1 \end{bmatrix}, \ \Gamma_{oP} = \begin{bmatrix} 1 & 0 \\ 0 & e_2 \end{bmatrix}, \ \Gamma_{iQ} = \begin{bmatrix} 1 & 0 \\ 0 & 1 \end{bmatrix}$$